Nanomaterial-Based Surface Modifications for Improved Ballistic and Structural Performance of Ballistic Materials

by

Kelsey Steinke

A dissertation submitted in partial fulfillment
of the requirements for the degree of
Doctor of Philosophy
(Materials Science and Engineering)
in the University of Michigan
2022

Doctoral Committee:

Professor Henry Sodano, Chair
Lecturer Kathleen Sevener
Professor Alan Taub
Professor Anthony Waas

Kelsey Steinke

steinkka@umich.edu

ORCID iD: 0000-0001-9090-0720

Dedication

This dissertation is dedicated to my parents; without all their love and support, this would not have been possible.

Acknowledgements

I would first and foremost like to thank Dr. Sodano for giving me the opportunity to be part of his research group and to work in the aerospace materials laboratory. I am appreciative of the chance to work together to discover new knowledge. His enthusiasm and drive for research has challenged me to strive for excellence, pushed me to think more critically, and helped me to answer meaningful research questions in the process. His mentorship, guidance, and high expectations have made me a better scientist/engineer, and for that I am grateful. I would also like to thank my committee members Dr. Kathleen Sevener, Dr. Alan Taub, and Dr. Anthony Waas for their valuable guidance, suggestions, and support in the completion of my dissertation work.

Second, I would like to sincerely thank my past and present lab mates Dr. Brendan Patterson, Dr. Hyun-Sik Hwang, Dr. Mohammad Malakooti, Dr. Alireza Nafari, Dr. Jiajun Lin, Jaehyun Jung, Ruowen Tu, and Steven Momallo for their support and encouragement in my research endeavors as well as their companionship. In particular, I would like to thank my co-author, Dr. LoriAnne Groo, whose expertise played an important role in my publication, along with her close friendship and unwavering support to help with the everyday struggles throughout these last few years. I would also like to acknowledge and thank my colleague and postdoc, Dr. Jalal Nasser, for his encouragement, valuable discussions, and friendship that played a significant role in my PhD journey.

I would like to thank my friends here in Michigan for your constant encouragement, friendship, and the fun times we have shared. I would also like to thank all of my other close friends back home who have always supported me through my high and lows of graduate school.

Thank you for keeping me grounded when I was struggling, always believing in me, and always being a light and a place for laughter.

I would like to send appreciation to my family for their love and guidance. In particular, I would like to thank my brother for his encouragement, positively and excitement of my research endeavors throughout the duration of my PhD pursuit. Lastly, I would like to thank my parents for their endless support and unconditionally love. They have always encouraged me and helped me believe in myself and my abilities, and my achievements during my time at Michigan would not have been possible without them. Words cannot express how grateful I am for their sacrifices and the life they have provided for me and I would not be the person I am today without them.

Table of Contents

List of Tables

List of Figures

List of Equations

Abstract

Improving the ballistic protection abilities of engineering materials has become increasingly important given the continuous rise in threat levels. Two polymeric fibers heavily used as ballistic materials for their high strength to weight ratio, impact resistance, energy absorption, and wear and abrasion resistance are ultra-high molecule weight polyethylene (UHMWPE) and aramid fibers. These fibers are used both as fiber reinforcement in polymer matrix composites for hard body armor applications, such as helmets and military vehicle armor panels, and as woven fabrics for soft body armor applications, such as bullet proof vests and gloves. Yet, in the case of fiber-reinforced polymer composites (FRPCs), these polymer fibers are known to suffer from poor adhesion to the matrix due to their smooth and chemically inert surfaces, resulting in discontinuous interfaces that limit their FRPCs from reaching their use in structural applications. In addition, when these polymer fibers are woven into a fabric, their resulting low inter-yarn friction causes for easy slipping between neighboring yarns, which reduces structural packing within the woven fabric and results in failure at lower velocity threats. Therefore, both the fiber-matrix interface and the inter-yarn friction of UHMWPE and aramid fibers require considerable improvements for furthering their use and their performance in ballistic and structural applications. Research efforts aiming to improve these properties have mainly relied on the development of fiber surface modification techniques. Particularly, nanoscale surface modifications have gained attraction in recent years due to their ability to simultaneously introduce bonding mechanisms that rely on chemical interactions and mechanical interlocking. However,

current approaches are known to compromise the structural integrity of the fibers, its weight, or its scalability to industrial level applications.

This dissertation explores the use of three nanomaterial-based surface modifications, primarily aramid nanofibers (ANFs) and zinc oxide nanowires (ZnO NWs) on UHMWPE fibers and laser induced graphene (LIG) on aramid fibers, in order to improve the interfacial and inter-yarn properties of UHMWPE and aramid fibers through simple, fast, and benign processes. The adhesion between ANFs or ZnO NWs and the UHMWPE fiber surface was initially improved using a surface functionalization treatment that formed a well-adhered nanostructured interphase. Single-fiber pullout was used to investigate and optimize the interfacial reinforcement effect the ANF and ZnO NW interphases have in UHMPWE FRPCs. The ZnO NW interphase on woven UHMWPE fabric was then studied through yarn pullout and impact testing where improvements in the fabric's inter-yarn friction, impact performance, and energy absorption were demonstrated. Finally, the use of a LIG interphase in aramid FRPCs was shown to suppress delamination and improve both interlaminar fracture toughness and impact resistance. Concurrently, the piezoresistive LIG interphase was shown to be capable of enabling in-situ structural health monitoring via electrical resistance measurements that correlate to impact damage and delamination in aramid FRPCs. The work in this dissertation demonstrates effective methods to modify the chemically inert and smooth surfaces of UHMWPE and aramid fibers through three nanomaterial-based surface modifications that enable improved interfacial and inter-yarn properties and further advances the integration of the FRPCs and woven fabric in high-performance structural and ballistic applications.

Chapter 1. Introduction

1.1. Motivation

Advancements in technology and weaponry have demonstrated an increased demand in the need for and application of ballistic materials, specifically polymer fibers. Two highly favorable polymer fibers used in military and defense applications, among others, are ultra-high molecular weight polyethylene (UHMWPE) and aramid fibers. As shown in Figure 1.1, the market for UHMWPE and aramid fibers has increased and is expected to grow with a global compound annual growth rate of 11.3% from 2018–2026 and 6.5% from 2018–2025, respectively. The market for UHMWPE is driven by demand from the healthcare industry due to an increase in orthopedic implants, such as joint replacements for knees and hips. The application of UHMWPE in the shipping, aerospace and defense industries is the second largest market expected to grow over the next five years (Figure 1.1A) due to an increase in demand for its use in personal protective equipment and anti-ballistic applications (e.g., bulletproof vests, impact plates, helmets). UHMWPE is used in other applications for its desired properties of superior impact strength, high energy absorption, wear-resistance, non-toxic, corrosion-resistance and low water absorption [1]. For aramid fibers, the United States market is dominated by security and protection applications, and its use in body armor fuels that market (Figure 1.1B). The use of aramid fibers has also been increasing in industrial protective equipment for worker safety such as its use in headgear and body gear. Due to its high strength-to-weight ratio, abrasion and impact resistance, and high energy absorption properties aramid fibers are used in a wide range of other applications (e.g., tire and rubber reinforcement, friction products, optical fibers) [2].

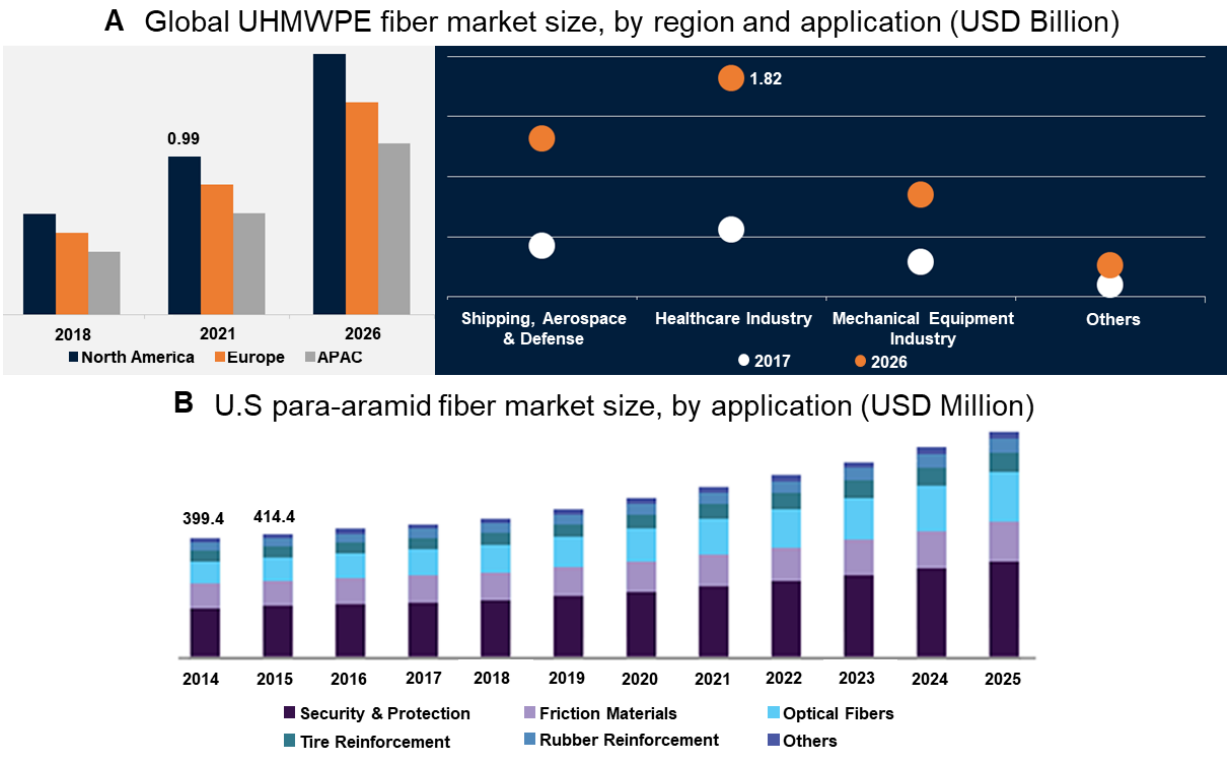

Figure 1.1. (A) Global UHMWPE fiber market size, by region and application (USD Billion) [1]. (B) U.S para-aramid fiber market size, by application (USD Million) [2].

Although UHMWPE and aramid fibers are widely used, they suffer from poor interfacial properties in both composites and fabrics. In fiber reinforced polymer composites (FRPCSs) and woven fabric, there are multiple failure modes that occur that do not allow them to reach their theoretical maximum properties. The failure modes in FRPCSs are shown in Figure 1.2A, and includes matrix cracking, fiber breakage, delamination, and debonding [3]. The properties of FRPCs are based on the properties of its two components and the interface between them. The discontinuous interface between the fiber and the matrix, which lacks chemical interactions, and the difference in stiffness between the fiber and matrix leads to poor load transfer and interfacial stress concentrations that can cause interfacial failure.

To overcome the poor interface in FRPCs, the discrete fiber-matrix interface needs to be replaced with a functional gradient that bridges the fiber and matrix components. A functional

gradient creates a gradual transition between the soft and stiff component instead of an abrupt change between the two. The blending of material properties alleviates stress concentrations at the fiber-matrix interface. Figure 1.2B illustrates that the interfacial shear strength (IFSS) of UHMWPE and aramid fibers are significantly lower compared to other reinforcing fibers due to a lack of functional groups in the polymers that prevent them from sufficiently bonding to the matrix (Figure 1.2B). While UHMWPE has a wide variety of properties and applications, the inert smooth surface of the fibers result in this substantially low IFSS which limits its use as a reinforcement in FRPCs for structural applications.

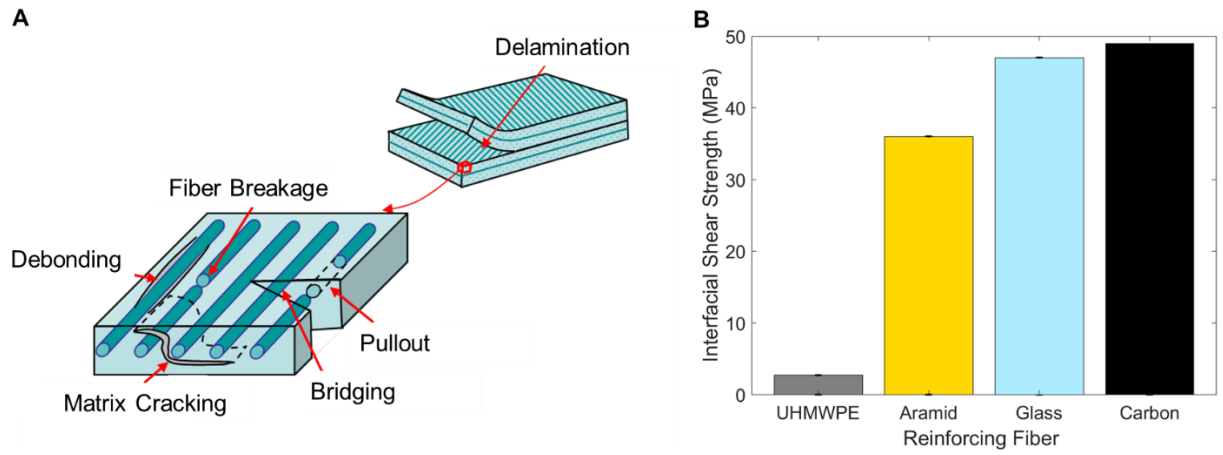

Figure 1.2. (A) Failure modes in FRPCS [3]. (B) IFSS comparison for UHMWPE, Aramid, glass, and carbon reinforcing fibers.

When the polymer fibers are woven into a fabric they exhibit different failure modes than FRPCs, which include windowing, fiber pullout, and fiber breakage as shown in Figure 1.3 [4]. The inter-yarn friction between yarns has been studied and proven to be the most vital property for the fabrics impact performance [5]. Low friction between yarns causes slippage between the primary yarns, which reduces the structural packing of the fabric. When slippage happens, the impact energy is solely on the primary yarns and not shared with the secondary yarns, which causes fabric failure/fiber breakage to happen at lower impact speeds. Woven UHMWPE fabric has low

inter-yarn friction attributed to its inherently inert surface and low surface energy, limiting its use in ballistic impact applications. When the friction between yarns of woven fabric is increased, there is improved load transfer between yarns that allows for the fabric to be impacted at higher velocities before failure. Therefore, to improve and advance the use of polymer fibers in high-performing composites and ballistic impact applications, the fiber-matrix and inter-yarn interactions need to be improved.

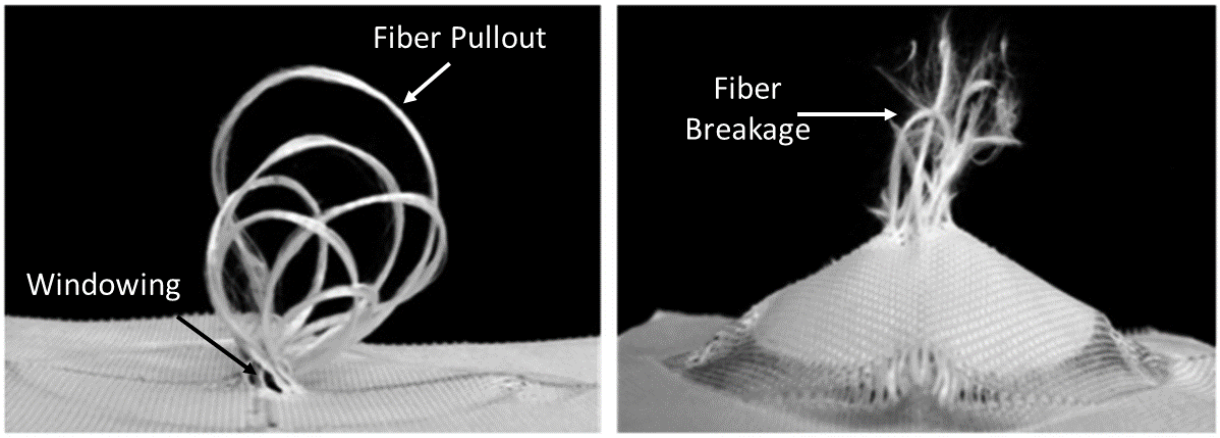

Figure 1.3. Failure modes in woven fabric during impact [4].

In this dissertation, the interfacial and inter-yarn properties of UHMWPE and aramid fibers are improved through the use of three nanomaterials-based surface modifications. Aramid nanofibers, zinc oxide nanowires, and laser induced graphene nanomaterials applied to the polymer fibers surface were used to improve the structural and ballistic performance measured through single-fiber pullout, yarn pullout, ballistic impact and mode I fracture toughness tests. Prior to the nanomaterial coatings, chemical functionalization was performed on the surface of the fibers to improve bonding with the nanomaterials. The nanomaterial-based surface modifications to the polymer fibers enabled enhanced chemical and mechanical interactions at the interface. The failure modes of the modified polymer fibers from the nano-structured interphases were analyzed to understand the reinforcement mechanism to improve the interfacial and inter-yarn properties.

This chapter summarizes a brief history and advancement of ballistic materials in vehicle armor, helmets, and vests. The two ballistic materials UHMWPE and aramid fibers will then be discussed in more detail in terms of their manufacturing, properties, and applications. This discussion is followed by a literature review of the various methods to enhance UHMWPE and aramid fibers interfacial property in FRPCs and the inter-yarn friction and impact performance of woven fabric. The following section aims to establish the advantages of a nanostructure reinforcement on the polymer fibers as a functional gradient in FRPCs and improve the inter-yarn friction in woven fabrics.

1.2. History of Ballistic Materials

Ballistic materials are used in protection applications to keep an individual safe from many levels of threats, including knives, hand-held weapons, and exploding munitions, by stopping penetration and absorbing the shock of the threat. Ballistic protection comes in forms of nonwoven and woven fabrics; compliant laminates; and composites for the use in vehicles, helmets, and vests [6]. Military vehicles, including ground vehicles, boats, and aircraft, require armor protection that varies depending on the type and level of threat the vehicle will encounter. Prior to the 21st century, military vehicles had little armor protection and were designed to be lightweight given that most protection would come from personal body armor. For example, Humvees were soft-skinned vehicles, boats had fiberglass hulls and deckhouses, and helicopters had sheet metal floors. With the increasing speed and lethality of modern threats, new vehicle armor and survivability requirements were adopted, and the demand for lightweight armor increased due to its limited restriction on maneuverability.

Military vehicles have a wide range of size and operational duties which require different armor solutions. For military boats, large ships utilize composites placed behind the metal structure

to reduce weight to balance cost and performance. These ships do not typically prioritize light-weight armor since they have sufficient capacity; however, faster and more agile boats may require more lighter-weight and high-performance armor solutions. Relatedly, fixed- or rotary-wing vehicles utilize light-weight armor for the weight reduction. High armor protection is needed for attack helicopters; however, there is increased protection needed for utility and lift vehicles as missions evolve with changes in the battlefield. During medical evacuation, helicopters may encounter small arms fire, demonstrating the importance of adding auxiliary armor. Ground vehicles add protection not in the form of the body structure, but by the supplemental armor that is attached on the outside and the inside of the hull. Composite armor attached to the inside of the hull, or spall liners, are used to catch break offs from the hard brittle hull after impact and reduce lethality of penetrating overmatching threat. Additionally, add-on kits, which consist of hybrid construction of metal or ceramics and composites, can be added when extra protection is needed; however, the vehicle is not burdened by the extra weight when it is not needed [7].

Helmets were designed to fully enclose the head to protect the brain and skull from a variety of impacts and were originally made from metallic materials. During World War I, helmets were made from steel and provided protection from fragmenting projectiles, although they could not stop a rifle bullet [8,9]. During World War II, a new grade of metal known as Hadfield steel was used along with an inner-molded nylon fiber liner to create the M1 or “steel pot” helmet. The M1 was still unable to stop close range bullets or shrapnel, but it offered improved protection and was used until the mid-1980s. After the invention of Kevlar in the 1960s, the helmet was then molded out of Kevlar with phenolic resin, which provided greater protection and reliably stopped most bullets, shrapnel, and pistil caliber bullets. The next major advancement in helmet design was the use of UHMWPE fibers, which offer enhanced ballistic protection. While these fibers might not

be as good as Kevlar when it comes to creep resistance, the major advantage of UHMWPE fibers is the weight savings over aramid for the same or advanced protection levels. There are also advances in the energy-absorbing abilities of the helmets to provide better protection from traumatic brain injuries, especially from explosives.

Various materials have been used as body armor since time immemorial as protection. For example, leather was used in Grecian shields, layered silk in ancient Japan, and chain mail for armored suits during the Middle Ages. Body armor made from metal significantly impeded the mobility of the wearer to be practical. During World War II, synthetic fiber-based ballistic protection was first reported as the flak jacket made of nylon fabric; however, it did not protect against bullets, only sharp objects and exploding fragments. When Kevlar was invented, it created huge advancements in body armor and was revolutionary for having high tensile strength while still being flexible and lightweight. Kevlar vests had the ability to protect against bullets, and by the 1980s, up to 50% of law enforcement wore Kevlar vests on the job which saved many lives [10]. Since Kevlar revolutionized body armor, research has been ongoing into several new fibers and construction methods for bulletproof fabric. These new fibers and fabrics being researched and produced, such as UHMWPE, offer enhanced penetration protection and impact resistance as well as remaining lightweight and have promise to become the standard for body armor of the future [10].

With the advancements in ballistic materials as well as the increasing need for improved protection, the ballistic protection markets compound annual growth rate is 6.5% from 2020–2025 (Figure 1.4A) [11]. Manufacturers are focusing on improving ballistic performance through making materials lighter, thinner, and more durable. The need for advanced protection also comes with the advancement in technology and ballistic weapons. FRPCs have been the largest market

compared to ceramic and metal matrix composites and is expected to continue to grow and be the largest market by value and volume, due to FRPCs light weight, temperature resistant, and high friction properties [12]. As shown in Figure 1.4B, the increase in the armor material market is driven by innovative products related to body armor such as vests, helmets, and gloves [13]. Advancement in textile materials allow for lightweight armor with improved ballistic protection. Figure 1.4 demonstrates that the ballistic material market is expected to continue to grow and along with that is the need for advanced and improved material systems.

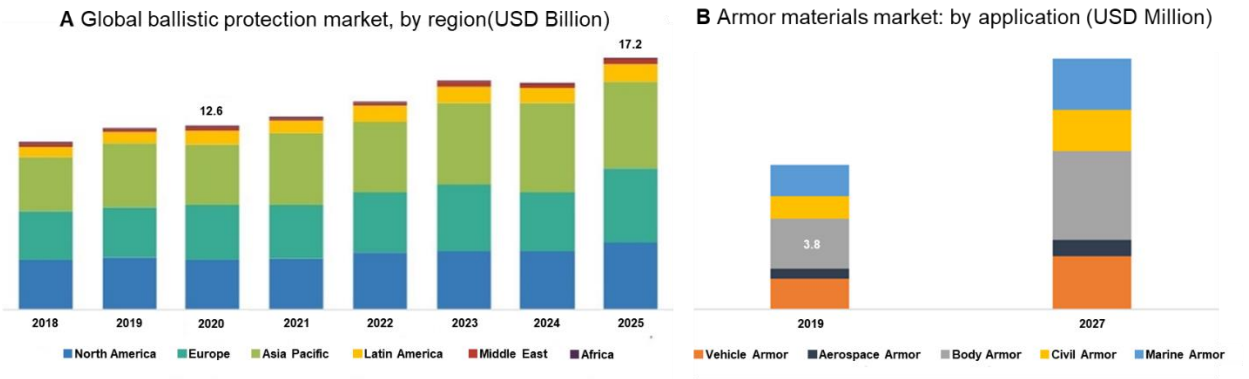

Figure 1.4. (A) Ballistic protection market, by region from 2018-2025 (USD Billion) [11]. (B) Armor materials market, by application from 2019 to 2027 (USD Millions) [13].

Currently, ballistic materials are diversified based on their intended application as previously discussed with the variations in materials used for vehicles, helmets, and body armor. However, most ballistic materials look to (a) *stop* the penetration, (b) *absorb* the focused shock of a projectile, (c) *spread* out the force, and (d) *prevent* the object from doing the damage for which it was designed. Common ballistic materials are metals and alloys, composites, ceramics, fiberglass, ballistic nylon, aramid fiber and UHMWPE fiber. Steel is the cheapest armor material and can weather multiple hits without degrading like other armor materials. However, steel is heavy and cannot conform to the wearer's body easily, making it uncomfortable to wear. Ceramics are used for their high armor protection, improved energy absorption and dispersion, as compared

to steel, and their excellent creep and stress rupture resistance. However, ceramics plates are often heavy, restrict wearers' mobility, and may be unable to withstand multiple hits, hindering its applications and growth. Fiberglass is not used in flexible body armor as it has low ballistic resistance against handgun bullets, however its used as molded armor with a combination of phenolic/polyvinyl butyral (PVB) resin in ballistic panels, which can be used as spall liners in military vehicles [7]. Ballistic nylon has high abrasion resistance and durability making it useful in end-uses in gear, which endures constant repetitious use; however, it is no longer used for body armor protection as it offers limited protection against bullets. Two of the most common ballistic materials for body armor are UHMWPE and aramid fiber. These two material properties are discussed in detail in the following sections.

1.2.1. Ultra-High Molecular Weight Polyethene Fabric (UHMWPE)

Low-density polyethylene fiber has been available since the 1930s and was commercialized in the 1950s. Since then, it has been used in many applications including bottles, caps, toys, housewares, agricultural mulch, pipes, trash bags, and grocery bags[14]. Regular polyethylene molecules are not orientated and are easily torn apart, so to strengthen the fibers, the molecular chains must be elongated, crystalized, and oriented in the direction of the fiber to allow for sufficient interaction and load transfer. The discovery of the gel-spinning process in 1979 allowed for the production of ultra-high molecular weight polyethylene, which was produced on the commercial scale beginning in 1990 [15]. The gel-spinning process has three main steps: continuous extrusion of a UHMWPE solution, spinning, gelation and crystallization of the UHMWPE, and removal of the remaining solvent and super-hot drawing. A schematic representation of the gel-spinning process is shown in Figure 1.5 [15]. UHMWPE is first suspended in a solvent and fed through a heated extruder to dissolve the UHMWPE powder. The

solution is spun and fed through a spinneret and extruded through spinning holes that allow for fibers to form and for crystallization to be enforced by cooling. The solvent is removed from the fiber and subjected to extensive hot drawing. Extremely high draw ratios can be achieved due to the reduction of entailments per polymer chain due to the dissolution process. Low interaction between polymer chains can also achieve high draw ratios, which then result in high molecular orientation and high strength fibers [16].

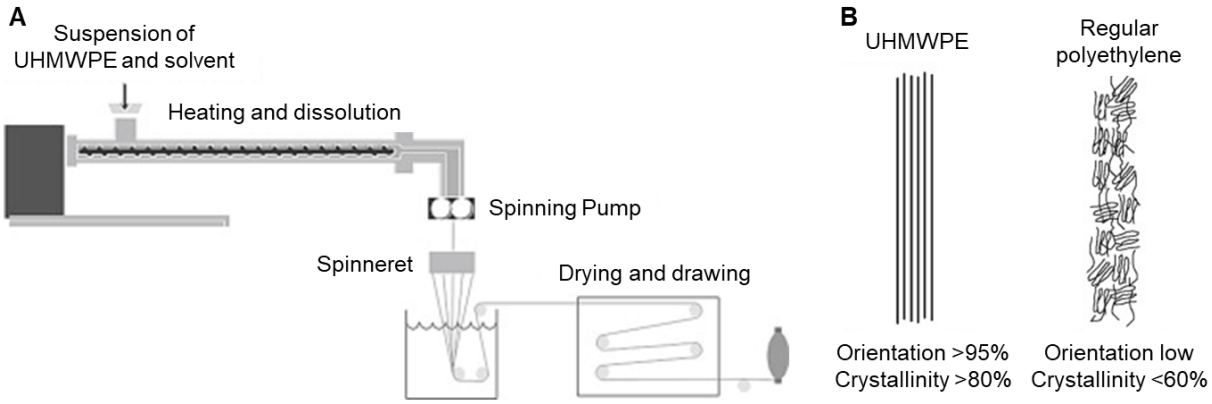

Figure 1.5. (A) Schematic of UHMWPE polymer fiber gel-spinning process and the (B) macromolecular orientation of regular polyethylene and UHMWPE [15].

The chemical structure of UHMWPE is a simple repeating CH_2 molecular unit. The fibers make up extremely long chains (200,000 repeat units with a molecular weight of 6 million g/mol) that are aligned in the same direction and bonded to each other with numerous van der Waals bonds. These van der Waals bonds provide the superior load transfer between these chains [7,15,17]. The UHMWPE polymer chains are highly orientated and crystalline (>80%) compared to regular polyethylene (Figure 1.5B). The primary property of UHMWPE is the high strength and high modulus in combination with a low density. In fact, the tenacity is 10-15 times that of good quality steel. The fibers have lower heat resistance due to the weak bonding between the olefin molecules, which allows for thermal excitation to disrupt the crystalline structure. The UHMWPE melting point is around 144–150 °C and they maintain performance below -50 °C. Due to the high

crystallinity and simple molecular structure, which does not contain any other chemical groups, UHMWPE (a) has low surface energy; (b) is resistant to chemicals, acids, and alkali environments, ultraviolet (UV) radiation; and (c) is not sensitive to attachment by microorganisms [15]. Polyethylene is hydrophobic and has low porosity, and therefore, water absorption in UHWMPE fibers is negligible. UHMWPE has a low coefficient of friction that results in good fiber-to-fiber wear and abrasion resistance as well as excellent resistance against external abrasion. UHMWPE fibers have the ability to absorb extremely high amounts of energy and have a high impact resistance. However, UHWMPE is sensitive to creep, has low adhesion to other materials and low compression yield strength, which limits its usage [17].

Due to the numerous desired properties of UHMWPE, it is used in a wide range of applications. It is a suitable material in a wide range of industries including automotive, aerospace, marine, forestry, medical and military applications. Some of the first products made with UHMWPE were in the marine industry. The fibers are used in many heavy-duty rope, net, and sail applications due to their high strength and low weight. The fibers also have excellent abrasion and fatigue resistance, do not lose tenacity in water or UV, can float on water, and are flexible, which make them easy to handle. UHMWPE is also used in nets in the aviation industry. In leisure and sports applications, it is used for sporting goods such as archery bow strings and water skis, due to its excellent impact resistance and vibration damping; and fabric for backpacks, tents and tarps as it is lighter and stronger than other materials. In the medical community, UHMWPE is used in many orthopedic implants in knee, shoulder, and hip surgeries due to its biocompatibility, abrasion resistance, and toughness. Due to its high energy absorption, UHMWPE is used in “soft” and “hard” ballistic protection where low weight and high protection is needed.

UHMWPE woven fabric is extensively used as soft body armor in the form of vests to protect against fragments and handguns. Woven UHMWPE is also used as net panels, which are light weight and a highly effective armor solution for protecting vehicles against Rocket Propelled Grenades. Helmets and lightweight panels are forms of hard armor UHMWPE is used to make. The light-weight helmets can offer protection against bomb and grenade fragments and handgun and rifle threats. UHMWPE armor panels are used in lightweight military vehicles and easily-molded inserts into vests to protect against highly penetrating rifle ammunition. UHMWPE panels are also used in military helicopter cockpit doors to provide ballistic protection and in naval ships as the main armor material due to their water resistant property along with being lightweight and strong [15].

1.2.2. Aramid Fabric

Aramid fibers are derived from aromatic acids and amines that have a long chain with amide linkages directly attached to two aromatic rings. A para-aramid orientated polyamide called Kevlar® was synthesized in 1965 by a DuPont research scientist, Stephanie Kwolek. Kevlar® aramid fibers are based on poly (P-phenylene terephthalamide) and are spun through a process called dry-jet wet spinning. An anisotropic solution of terephthalic acid and p-phenylene diamine are extruded through an air gap and coagulated in a bath to generate a yarn that is then washed and dried. The fibers are then drawn at a temperature higher than 300 °C to increase the modulus [7,18]. The para-aramid molecular structure is highly orientated and forms a crystalline structure that has hydrogen bonds between the adjacent polar amide groups in the molecular structure as shown in Figure 1.6.

The high strength and thermal resistance of para-aramids come from the stability of the aromatic ring and the added strength of the amide linkage due to conjugation with the aromatic

structures and the linear geometry of the para link, which offers greater chain orientation [7]. This high crystallinity results in insignificant shrinkage at high temperature, low creep, and a high glass transition temperature. Aramid yarns have a breaking tenacity more than 5 times than steel. The structure exhibits anisotropic properties, with higher strength and modulus in the fiber longitudinal direction than in the axial direction, meaning it has a poor compressive strength. Para-aramid fibers also have a large capacity to absorb kinetic energy causing them to have high impact strength. They also have high toughness and are cut and abrasion resistance. Aramid fibers are resistant to many organic solvents and salts, but they have loss of strength when exposed to strong acids and bases. The aromatic structure of the para-aramid is responsible for oxidative reactions when exposed to UV light, which leads to a color change and loss of strength. Aramids also contain amide links that are hydrophilic, which means the fibers absorb moisture, and this process can lower their strength making them more environmentally sensitive.

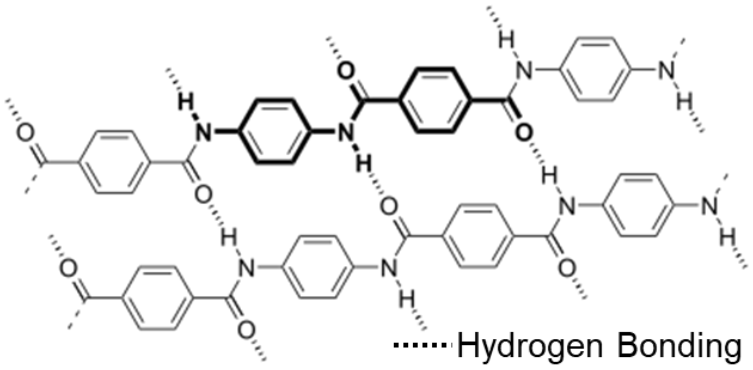

Figure 1.6. Chemical structure of para-aramid fiber.

Due to the wide range of desired properties of aramid fibers, they are used in a variety of applications from a range of industries. As friction materials in the automotive industry, aramid fibers reinforce tires, brake pads, belts, linings, and clutch facings due to their thermal stability and abrasion resistance. Due to the chemical, thermal, and high-pressure stability, aramid fibers help make gaskets strong and durable. Aramid FRPCs are utilized in the aerospace, automotive, marine,

and rail industries to build aircraft, cars, ships, and rail carriages. Aramid FRPCs can reduce the weight without compromising strength and help to increase fuel efficiency while also being able to manufacture complex shapes with minimal need for rivets and fasteners and decrease operating and maintenance costs. In the sporting goods industry athletes, outdoor aficionados and anyone looking for lighter, stronger, and safer sports products can use aramid fiber in sails, skies, tennis strings and in protective apparel such as gloves, motorcycle and hunting protective clothing. Aramid fibers can also strengthen ropes and cables in many applications due its cut, abrasion and fatigue resistance, durability and being able to withstand temperature and environment extremes. Aramid fibers are also used as a reinforcement for glass fiber optical cables for their high strength, lightweight capability, and flexibility to help against mechanical stress and guarantee optimum performance.

Due to aramid fibers having high strength to weight ratio, energy absorption capabilities and impact resistance, they are employed in a variety of ballistic applications. Aramid fibers woven into a fabric are used as soft body armor (ballistic vests), to help protect human lives against ballistic and fragment threats. Aramid fiber laminates can be molded into helmets which provide added protection from bullets and steel fragments from handheld weapons and exploding munitions [19]. Aramid composites are an effective and lightweight armor solution on trucks as spall liners, as well as other fragment protection applications on vehicles, planes, and ships that provide protection from ballistic attacks when increased security is needed and weight is a critical factor. Aramids thermal stability and high glass transition temperature also ensures the integrity of ballistic armor structure at elevated temperatures during a ballistic event [17,20–22].

1.3. Interfacial Modifications of UHMWPE Fabric and Fiber Reinforced Polymer Composites

Failure in a woven fabric or FRPCs form can severely limit the performance and applications of UHMWPE fibers. The impact performance of woven fabric is affected by multiple parameters such as yarn linear density, thread density, crimp, and number of crossovers [5]. However, one factor considered to be the most vital to the performance of woven fabrics is inter-yarn friction [5]. Theoretical and experimental studies have found that increased inter-yarn friction of woven fabrics can improve the ballistic performance [5,23–30]. As shown in a simulation in Figure 1.7, the woven fabric with the lower friction coefficient, the yarns can easily slip past each other and show significant yarn distortion and yarn pullout in the impact region and of the primary yarns, or those yarns directly in contact with the projectile [29]. When the coefficient of friction increases, the structural packing is maintained due to the friction of the yarns at the crossover points restricting motion between the yarns. The increased friction between warp and weft yarns reduces slippage between primary yarns and helps maintain the structural packing of the fabric during impact, thus improving impact resistance [23,26,27].

Inter-yarn friction has also been shown to control the amount of energy released during impact, which improves the energy absorption properties of woven fabrics [23,28–30]. As the friction between the warp and weft yarns increases, more impact energy is shared by secondary yarns, or yarns not in direct contact with the projectile [23]. This increased friction also reduces the maximum load on the primary yarns and prolongs fabric failure at higher velocities [23]. Therefore, increasing the inter-yarn friction improves the impact resistance of woven fabrics. In contrast, poor inter-yarn friction between weft and warp yarns is attributed to the inherently inert and low surface energy of the UHMWPE fiber [31,32]. To increase the impact performance of

woven fabrics, the friction between yarns should be increased, which will improve the load transfer between yarns and allow for the fabric to withstand higher velocity impacts.

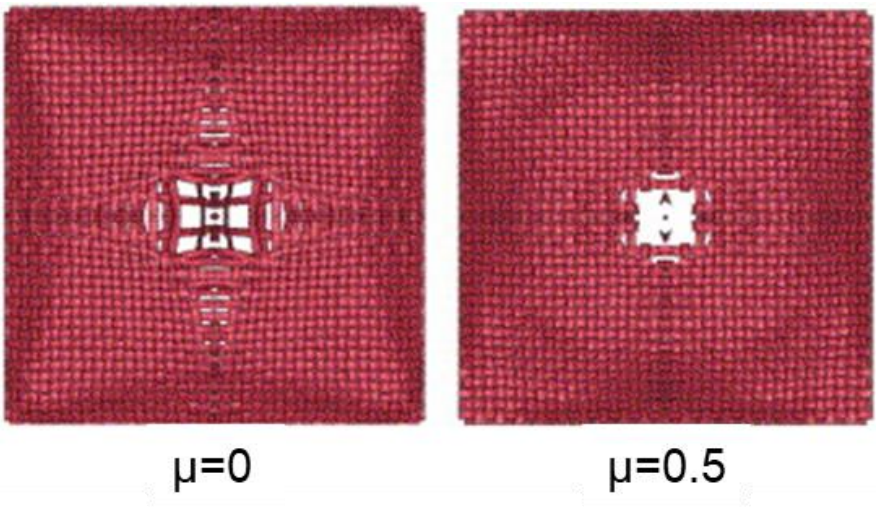

Figure 1.7. Comparison of simulated woven fabric failure for different friction conditions of μ=0 and μ=0.5 [29].

The performance of composite materials is primarily dependent on the choice of fiber and matrix, however its final properties are typically dictated by the interface between them [33]. Interfacial properties in composite materials are usually determined by chemical interactions, mechanical interlocking, and the size of the surface area between both interface constituents [34,35]. Due to the previously mentioned low surface energy, smooth, high crystallinity, and chemical inertness of the fiber surface, UHMPWE composites exhibit in poor adhesion at the fiber-matrix interface due to the absence of chemical bonding and a lack of mechanical interlocking. The chemically inert surface of the UHMWPE fibers can also result in poor resin wetting of the fibers during composite manufacturing, which can also lead to poor interfacial properties. As a result, in interfacial debonding is a common failure mode observed in UHMWPE composites when used in structural applications. In sum, it is important to enhance the UHMWPE fiber-matrix interface so that the structural performance of composites can be improved, and their potential applications expanded [33–36]. The literature review presented in this section is dedicated to the

chemical and morphological modification techniques to the fiber surface used to improve the inter-yarn friction and interfacial adhesion of UHMWPE woven fabric and FRPCs.

1.3.1. Ballistic Applications

It is vital that the materials used in military applications have high-impact resistance and energy absorption properties for ballistic protection during combat, however UHMWPE suffers from poor inter-yarn friction that limits its protection capabilities, thus to enhance its use in armor applications the inter-yarn friction needs to be improved [5]. To overcome the inert and low surface energy limitation of UHMWPE and enhance its use in soft body armor applications, researchers have investigated the use of chemical treatments, films, and nanoparticle coatings to improve the inter-yarn friction of UHMWPE woven fabric [19,23,37–42]. One major area of research for improving the inter-yarn friction of woven UHMWPE is the infusion of a shear thickening fluid (STF) into the fabric [37–40,43]. Arora et al. infused a STF made from silica particles dispersed in polyethylene glycol into the UHMWPE fabric. This process subsequently increased the inter-yarn friction and impact energy by 427% and 55%, respectively, as shown in Figure 1.8 [37]. A major drawback of STFs is that they can significantly increase the weight of the fabric, and with exposure to moisture and natural aging, STFs can lose their unique rheological properties [19]. Li et al. impregnated UHMWPE with a STF with a polyethylene glycol additive at different concentrations and molecular chain lengths. This process (a) decreased the mobility of the yarns, (b) accelerated the transverse response, and (c) increased the inter-yarn friction to improve the stab response. Specifically for PEG10000/4% at a drop height of 0.6 m, there was a 27% increase in peak force and a 33% increase in impact energy for a spike threat and for a knife threat there was a 22% increase in load and 7% increase in impact energy [39].

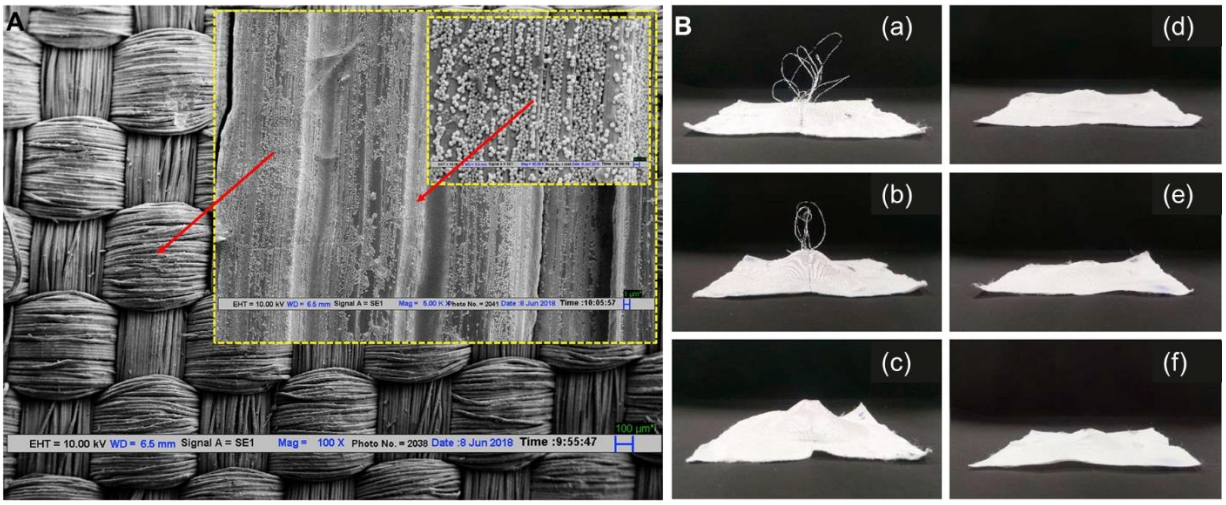

Figure 1.8. (A) SEM image of woven UHMWPE treated with STF. (B) Images of woven UHMWPE fabric failure after impact for a), b) ,c) neat fabric and d), e), f) STF treated fabric [37].

Another method that modified the surface of the UHMWPE fabric to improve the inter-yarn friction, documented by Firouzi et al., used nylon 6,6 and nylon 6,12 to coat the UHMWPE fabric. These nylon coatings improved the puncture resistance of the fabric by 77% and 86%, respectively [41]. The improved performance can be attributed to the fact that the nylon films on the surface of the UHMWPE fibers shrink upon drying, which creates an interlocking mechanism between the fibers [41]. Chu et al. showed that the inter-yarn friction of UHMWPE woven fabric can be improved using a plasma-enhanced chemical vapor deposition (PCVP) treatment. A PCVP treatment period of 2 min resulted in a 91% increase in the coefficient of static friction and a 70% increase in the coefficient of kinetic friction [42]. This improved performance is due to an increased amount of polar groups on the surface of the UHMWPE fibers [42]. It is important to note that plasma treatments did not degrade the tensile properties of the fibers [44–51]. The inter-yarn friction increased by 40% when the UHMWPE fabric was coated with a titanium dioxide/zinc oxide hydrosol [52]. When coated in this manner, the fabric weight does not increase and the tensile properties of the fibers are maintained. However, the energy absorption capabilities of the fabric only increased by 8% [52]. Roy et al. dipped the UHMWPE fabric in different

concentrations of natural rubber of 6% and 9%, where a maximum increase in yarn pullout and tenacity was shown at 9% with an increase of 359% and 52%, respectively. This finding can be attributed to the rubber binding the yarns together, which restricted their movement under loading [53].

In addition to the surface treatment methods described above, grafting nanomaterials onto the surface of the fabric has been employed to improve the inter-yarn friction and ballistic properties of UHMWPE woven fabric. Yang et al. used an alternative approach and coated UHMWPE fabric with hard boron carbide (B_4C) particles to study the effect of different processing and coating distributions. Through a sequence of experiments they found that the stab resistance load and energy absorption performance increased by a maximum of 60% and 63%, respectively, when the particle dimension was 5 microns, the coating thickness 100 microns, and the coating temperature 64 °C, and a ratio of the particle to binder of 2:3 [54]. Firouzi et al. coated UHMWPE fabric with a silicon carbide nanoparticle polyurethane mixture of 30 wt % and 50 wt % and showed a penetration resistance increase of a single UHMWPE ply increased by up to 218-229%. When multiple coated fabrics were stacked, Firouzi et al. showed an increase in spike puncture and hydro dermic needle resistance by 57% and 346%, respectively, relative to uncoated fabric [55]. The discussed surface modification techniques that improve the fabric ballistic performance through coatings and nanomaterial grafting confirms the important role of the inter-yarn properties to the impact response and behavior of UHMWPE woven fabrics.

Woven fabrics are useful in soft body armor ballistic protection applications; however, they are not a viable option where load-bearing abilities are also required. Thus, researchers have investigated methods to improve UHMWPE composites for hard armor. Shanmugam et al. coated the UHMWPE fiber surface with a combination of polydopamine and .03 wt % MWCNTs. The

coated fiber structure was then put into a composite with a thermoplastic methyl methacrylate (MMA)-based matrix and impacted at energies of 26 J, 32 J, and 50 J. Results demonstrated that at all three energies, the treated composites demonstrated less structural damage and deflection compared to the untreated composite due to the improved delamination resistance at the fiber and matrix interface [56]. Liu et al. constructed a hybrid panel of UHMWPE and nano-porous functionalized liquid consisting of three things: nano-porous zeolite particles, water, and cellular energy absorption materials. The findings showed that the backface delamination was reduced for the hybrid composite by up to 17% compared to pure UHMWPE fabric panel with the same area density, and this decrease was attributed to the hybrid material being an energy transfer barrier that absorbed a large amount of energy, which prevented localized deformation [57]. Khan et al. used friction stir processing to reinforce UHMWPE composites with nano-hydroxyapatite particles. This reinforcement process improved the impact strength, Rockwell hardness number, and ultimate tensile strength by 27%, 6%, and 11%, respectively, compared to untreated UHMWPE composite [58]. Zheng at al. showed a 7% increase in energy absorption of corona treated UHMWPE fibers in a reinforced vinyl ester composite through increased surface roughness and oxygen containing groups which improve adhesion to the vinyl ester matrix [59]. Hu et al. showed that when UHMWPE fibers were woven into a carbon fabric, the penetration energy and damage tolerance increased by 71% and 10% , respectively, when compared to pure carbon fiber composite due to the excellent energy absorption and damping properties of UHMWPE fibers which restrict the initiation and propagation of cracks and delamination [60]. The improved ballistic performance obtained using the discussed surface modification techniques confirms the important role of the interfacial properties to the UHWMPE composite impact response.

1.3.2. Structural Applications

The inert fiber surface chemistry severely hinders the performance of UHMWPE fiber-reinforced composites for its use in structural applications [61,62]. To improve the fiber-matrix interface of UHMWPE FRPCs, researchers have primarily investigated fiber-surface treatments [63]. Wet and dry chemical treatment methods introduce functional groups and roughness through micro-pits to the UHMWPE fiber surface to increase chemical bonding and mechanical interlocking with the polymer matrix. Dry chemical treatment techniques include chromic acid [64–67], corona discharge [68–73], ultraviolet-irradiation [74,75], and gamma irradiation [76]. Wet chemical treatment techniques include chemical grafting [77,78], oxidative acid etching [79,80], and coating treatments [81–83]. Studies have also shown that plasma treatments can improve the fiber-matrix interface of UHMWPE fiber-reinforced composites through increasing fiber surface roughness and introducing polar functional groups, while preserving the tensile properties [44–51]. Wang et al. found that using a tannic acid-Na^+ coating to introduce reactive functional groups onto the surface of UHMWPE fibers improved the interfacial shear strength (IFSS) of UHMWPE composites by 43%, compared to untreated UHMWPE [79]. Tang et al. performed a 20 wt % sodium hydroxide alkali treatment on the UHMWPE fiber and put them into a polyimide matrix and showed after a 3-min treatment time that the interlaminar shear strength increased by 6%, and the composite tensile strength increased by 13% after a 5-min treatment time, relative to untreated UHMWPE fiber composites. This finding was attributed to increased surface roughness and increased surface oxygen containing functional groups which improve bond between fiber and matrix; however, prolonged alkali treatment can have a negative effect on the UHWMPE fiber mechanical properties [84].

Multiscale fiber surface modifications are another surface treatment to improve the interfacial properties which consists of the application of nanomaterial reinforcements, which add enhanced surface area and mechanical interlocking interactions with the matrix. Mohammadalipour et al. grafted glycidyl methacrylate (GMA) onto the UHMWPE fiber and embedded the fibers into a nano-clay/epoxy resin. They found a 229% increase in IFSS measured using micro-droplet testing [85]. Ahmadi et al. determined that the addition of multi-walled carbon nanotubes to a GMA and amino-thiol chemical treated fiber can yield a 336% improvement in IFSS [86]. Shanmugam et al. coated UHMWPE fibers with 0.03% of multi-walled carbon nanotubes (MWCNTs) that were embedded in a dopamine solution as shown in Figure 1.9. Through transverse fiber bundle testing, it was shown that the bonding between the UHMWPE fibers and the matrix was improved by 43%, relative to untreated UHMWPE fibers [87]. Shanmugam et al. treated UHMWPE with polydopamine and then added .03% of MWCNTs and increased the mode 1 interlaminar fracture toughness and IFSS by 20% and 43%, respectively, relative to untreated UHMWPE thermoplastic composite [88]. However, higher weight fractions of MWCNTs resulted in a heavily entangled uneven coating that led to poor resin wetting.

An alternative to MWCNTs, Jin et al. coated plasma treated UHMWPE fibers with polypyrrole and reported a 848% increase in compressive performance and a 54% increase in IFSS [82], but the tedious coating process was shown to degrade the tensile properties of the fiber due to the catalysis required to induce polymerization [63]. Zhang et al. trapped nano-silicon dioxide (1%) on the surface and diffused them into the UHMWPE fibers during the gel spinning process. The IFSS, measured through a single-fiber pullout test, increased by 148% relative to untreated UHMWPE fibers, but an increase in the nano-silicon dioxide concentration resulted in a decrease in the fiber's mechanical properties [89]. Li et al. performed a potassium permanganate surface

treatment on UHMWPE fiber in an epoxy composite with 0.3 wt % UHWMPE fibers. They found a 27% increase in the interlaminar shear strength and a 13% increase in bending strength which was attributed to the potassium permanganate increasing the fiber surface roughness and oxygen containing groups improving the interface interaction [90]. The fiber-surface treatments covered in this section confirm their use and importance to improve the fiber-matrix interface and thus improving the structural performance and application of UHMWPE composites. However, most current methods to improve UHWMPE woven fabric and composites suffer from a compromised structural integrity of the fiber, the addition of extra weight, and a reduction to fabric flexibility.

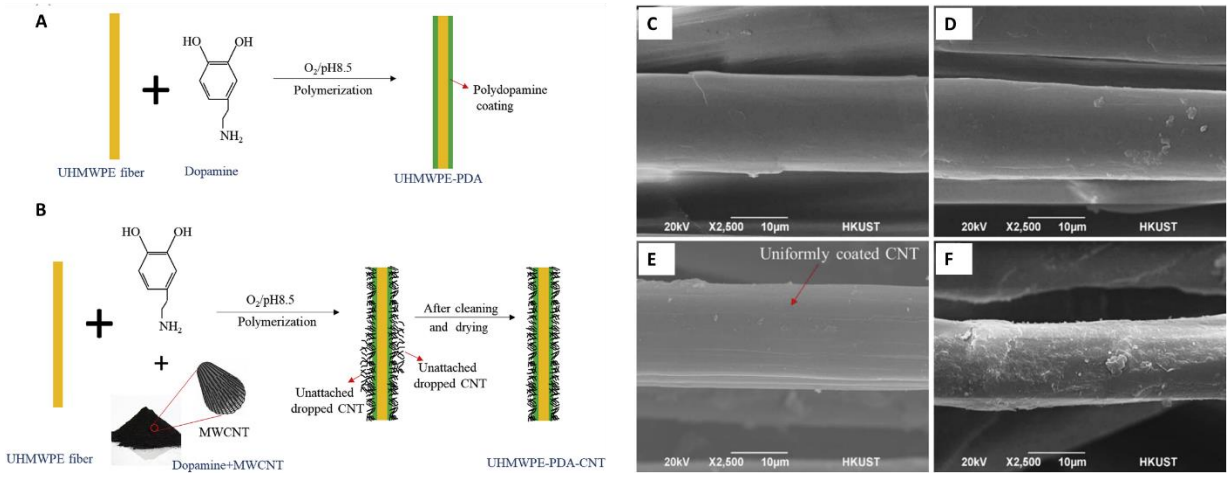

Figure 1.9. Coating of UMWPE with (A) polydopamine and (B) polydopamine + MWCNT. SEM images of UHMWPE fiber surface for (C) untreated, (D) polydopamine coated, (E) polydopamine + 0.03% MWCNTs and (F) polydopamine + 0.1% MWCNTs [87].

1.4. Interfacial Modifications of Aramid Fabric and Fiber-Reinforced Polymer Composites

As discussed in the previous section, the inter-yarn friction plays a vital part in the impact performance and energy absorbing capabilities of woven fabric. Relatedly, the fiber-matrix adhesion plays a crucial part in the overall performance of FRPCs. The literature review presented in this section describes the improvement of the (a) inter-yarn friction, (b) the impact performance,

and (c) the interfacial bonding between the fiber and matrix in aramid woven fabric and FRPCs through chemical and morphological modification techniques to the fiber surface.

1.4.1. Ballistic Applications

Aramid fabric is used in a wide variety of ballistic applications, and because of this the desire to improve the performance has gained interest from researchers to improve the aramid fabric inter-yarn properties and its ballistic performance. One major area in aramid fabric, similar to UHMWPE fabric, is the incorporation of STF to the fabric. There has also been the addition of additives to the STF to further enhance to inter-yarn friction and impact of aramid fabric [91–99]. Mawklieng et al. showed that the addition of graphene nanoplates increased the yarn pullout-force by 25% and led to a 20% increase in energy absorption compared to just STF-treated aramid fabric [92]. Tan et al. showed that STF reinforced with graphene improved the viscosity by 40% and improved the shear thickening efficiency by 32%. In addition, the graphene-reinforced STF increased the yarn pull-out by 300% and ballistic limit by 7% relative to pure STF treated aramid fabric. This increase was due to the coupling integration of the yarns from the graphene-STF which enables more yarns to join together and increase inter-yarn friction and impact resistance [100]. Sun et al. used non-polymerizing reactive plasma gas N_2 and dichlorodimethylsilane to modify the aramid fabric surface for the application of ballistic impact material. Their results showed a 15% and 300% increase in yarn pullout force, respectively, compared to untreated aramid fabric, and they attributed this increase to enhanced surface chemistry and roughness that increased the inter-yarn friction between the yarns due to the plasma polymer layer [101].

An alternative approach to STF and chemical treatments to improve the inter-yarn friction has been through nanomaterial surface modifications to the aramid fabric. LaBarre et al. coated aramid fabric with MWCNTs and found an increase in yarn pull by 230% and an increase in

ballistic limit of 50% compared to untreated aramid fabric. Entanglement among the MWCNTs, along with increased surface roughness and surface area, increased the resistance to motion and improved the impact performance by increasing the energy required to pull-out yarns from the textile and inhibited textile windowing [102]. Nasser et al. used a strong basic solution to generate microscale-to-nanoscale fibrils on the aramid fabric surface, which induced mechanical interlocking between the fibrilized fibers and yarns. This approach enhanced the pullout energy by 665%, pullout load by 550%, and the ballistic V_{50} by 12%, relative to untreated aramid fabric [103]. Nayak et al. coated aramid fabric with boron carbide to bind the threads of the fabric together and resist their movement which increased the knife, ball and pointed stab resistance by 119%, 211%, and 112%, respectively, from untreated aramid fabric [104]. The reported research has demonstrated the efficiency and importance of woven aramid fabric surface modifications through coatings and nanomaterials to improve the inter-yarn friction and thus the ballistic performance.

Although woven aramid fabric is beneficial as soft body armor, it is not a suitable option for hard armor where load-bearing structure in addition to impact performance is imperative. Therefore, researchers have investigated methods to improve aramid FRPCs impact performance. MWCNTs as an epoxy filler has been studied to improve the impact response of aramid fabric composites [105–108]. Taraghi showed that with 0.5% MWCNTs added to the matrix, the penetration limit increased by 40% and the absorbed energy increased by 35% relative to untreated composite, as shown in Figure 1.10, which illustrates a smaller size of damaged area at 0.5 wt% MWCNTs [107]. Mourad et al. showed that with the addition of 0.5% MWCNTs to aramid FRPCs, they had the smallest percentage of damaged area compared to untreated and other concentrations of MWCNT additives [108]. Sharma et al. interleaved bucky paper into aramid fabric composite

along with resin toughening with 0.3 wt % MWCNTs and demonstrated a 31% increase in impact force during low velocity impact and a 30% improvement in backface delamination during high velocity impact [109]. The MWCNTs in the epoxy improves the toughness, while the high surface area bucky paper interleaves offers enhanced interlaminar adhesion and improved energy absorption capabilities [109].

Alternatively to MWCNTs, Majumdar et al. coated aramid fabric with zinc oxide nanostructures and improved the impact energy of the coated aramid fabric composite by 35% relative to untreated aramid fabric due to the zinc oxide nanostructure providing better interlocking between the fiber and the matrix [110]. Rahman et al. added varying weight fractions of nano clay to the epoxy matrix of aramid composite panels and found that 10 wt % nano clay epoxy filler improved the ballistic impact load by 26% and energy absorption by 24% as well as improving the UV degradation and water absorption relative to untreated aramid fabric [111]. These improvements were due to the nano clay increasing the packing density and chemical bonding with the base molecular chains, and reduced porosities of the epoxy matrix [111]. Simic et al. showed that the addition of 0.3% tungsten disulfide inorganic nanotubes (INT-WS_2) in the matrix had an increase in impact toughness by 36%, reduced backface depths by 12%, and increased knife stab energy absorption by 9% as compared to untreated aramid composite [112]. Xia et al. coated aramid fabric with boron carbide in an epoxy resin and showed approximately a 900% increase in the tearing load and a maximum increase in ultimate puncture load per weight of 428% compared to untreated fabric [113]. The reported improved ballistic performance of aramid FRPCs demonstrates the effectiveness of an aramid fiber surface and matrix modifications to improve the fiber-matrix interphase.

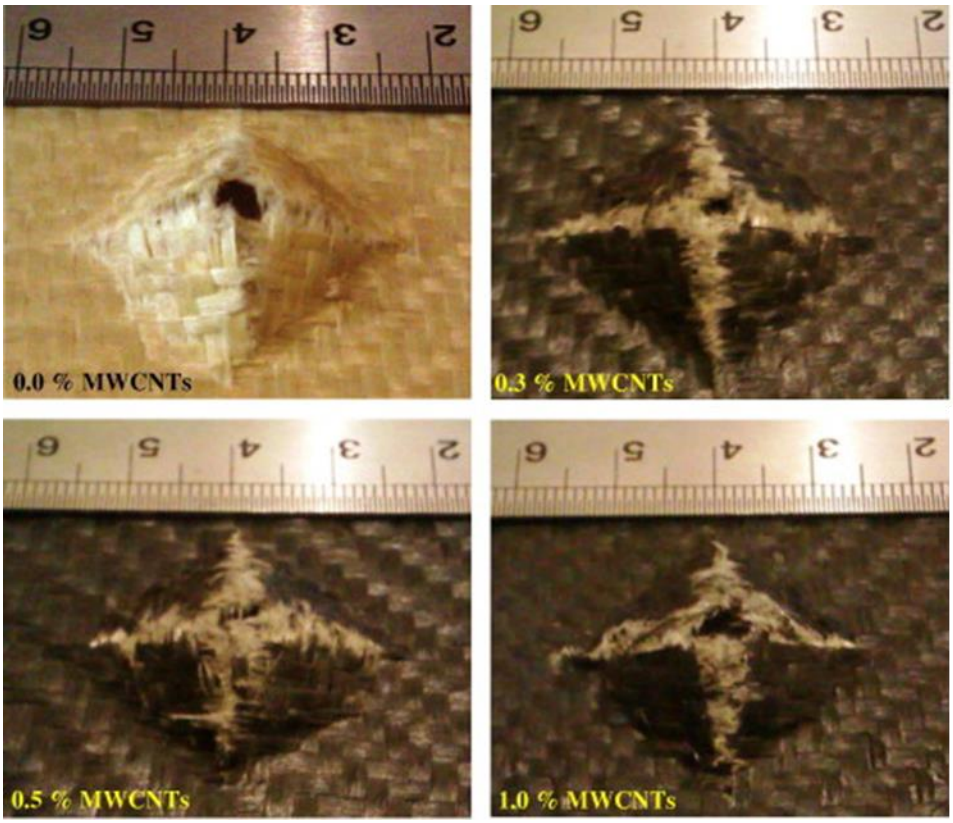

Figure 1.10. Effect of varying content of MWCNT on the damage development of aramid/epoxy composites [107].

1.4.2. Structural Applications

The fiber-matrix interface plays a critical role in FRPCSs, and through fiber and matrix modifications researchers have improved the structural performance of aramid composites. One aramid fiber surface modification method is to chemically treat the fiber surface to improve adhesion with the matrix. Yue et al. chemically treated aramid fibers with acetic anhydride and a 3-min methanol treatment and found a 60% increase in the aramid composite IFSS due to the enhanced chemical and mechanical interlocking with the matrix from an oxygen rich and roughened fiber surface [114]. Jia et al. grafted 3-aminopropyltriethoxysilane (APS) onto aramid fibers through γ-ray irradiation, which increased the IFSS by 51%, relative to untreated fibers. The increase in IFSS was attributed to chemical crosslinking with resin and the induced grooves on the

aramid fiber, which provided mechanical riveting between fiber and resin matrix to improve the bonding between the fiber and the matrix [115].

A widespread modification method is the addition of nanomaterials to the aramid fiber surface to improve the adhesion between the fiber and the matrix. Nasser et al. generated nanoscale aramid fibrils on the surface of aramid fabric through treatment from a strongly basic solution. This process, in turn, improved the IFSS by 128% and short beam strength by 62% relative to untreated composites through enhanced mechanical interlocking between the fiber and the matrix, and enhanced chemical interaction through an increase in oxygen-containing functional groups on the fiber surface. [116]. Wang et al. grew titanium dioxide (TiO_2) nanoparticles prepared without and with PEG on the surface of aramid fibers and showed a 40% and 67% increase without and with PEG, respectively. The addition of PEG (a) decreases the TiO_2 NP size, as shown in Figure 1.11, (b) increased the interaction area between the fiber and the matrix, and (c) reduced the stress concentration between the fiber and the matrix material [117]. Zhang et al. grew nano-silicon dioxide (SiO_2) on aramid fiber surface at varying pressures to change the size of the nano-SiO_2 particles. As a result of this process, the IFSS increased by 64% for the fibers treated with nano-SiO_2 under 14 MPa pressure, which demonstrated a more densely packed morphology due to the increased roughness of the fiber surface from the nanoparticles. This process, in turn, enhanced the interfacial adhesion of the aramid fibers with the matrix [118].

Graphene oxide is a widely studied reinforcement for aramid fiber composites [119–121]. Tian et al. first coated aramid fibers with polydopamine (PDA) to improve the adhesion of carboxylate and aminated graphene oxide (CGO and AGO) to the aramid fiber and demonstrated the IFSS and ILSS of CGO-PDA-aramid fibers increased by 64% and 50%, respectively. They also found that the IFSS and ILSS of AGO-PDA-aramid fibers increased by

77% and 63%, respectively, relative to untreated aramid fiber. The graphene oxide improves the mechanical interlocking between the fiber and the matrix and the enhanced improvement in the AGO-PDA-aramid fibers is due to the abundant amino groups on the surface which enhances the chemical interaction with the epoxy matrix [121].

Modifications to the matrix have also been demonstrated to improve the adhesion between the fiber and the matrix in aramid composites. Suresha et al. incorporated MWCNTs at 0.15%, 0.3%, and 0.5% by weight into aramid fiber-reinforced epoxy composites. They found the optimal MWCNT addition percentage to be 0.3%, which increased the tensile strength by 46%, tensile modulus by 22%, flexural strength by 74% and flexural modulus by 54%. These findings were attributed to the MWCNTs increasing the interface area and bridging the fiber and the matrix, which suppressed the growth and propagation of cracks in the matrix [122]. A larger percentage of MWCNTs leads to agglomerations and weakens the fiber-matrix interface, and by extension, the mechanical properties. The interfacial reinforcement techniques detailed in this section demonstrate the ability of aramid fiber surface and matrix modifications to improve the fiber-matrix adhesion and thus improve the structural performance of aramid FRPCSs. However, some current treatment methods have disadvantages, including that they damage the surface of the fiber resulting in a reduction in tensile strength, are not scalable, and are cost and time inefficient—all characteristics that limit their use in structural applications.

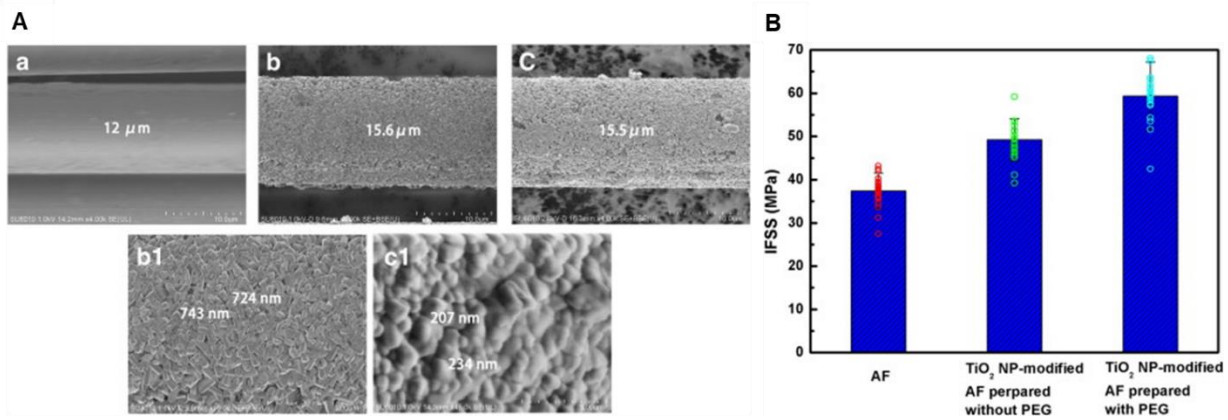

Figure 1.11. (A) SEM images of untreated aramid fibers and aramid fibers with TiO2 nanoparticles prepared with and without PEG on the surface. (B) IFSS values of untreated aramid fibers and aramid fibers with TiO2 nanoparticles prepared with and without PEG on the surface [117].

1.5. Structural Health Monitoring of Ballistic and Structural Composite Materials

Aramid fiber-reinforced composites are prone to significant structural and ballistic damage due to harsh operating environments, thus risking catastrophic failure in the employed structure. The ability to detect such damage can help assess the health of the structure, monitor its state, and most importantly avoid catastrophic failure by detecting damage while in its early stages. While damage detection can be achieved in conductive fiber-reinforced composites (e.g., carbon) using their innate piezoresistivity to correlate changes in electrical resistance to generated damage, this remains a challenge in aramid composites due to their electrically insulating nature. Thus, new techniques capable of monitoring damage in fiber-reinforced composites are needed to improve their safety and reliability.

Researchers have monitored in-situ damage in fiber-reinforced polymer composites using a wide variety of methodologies such as through optical fibers [123,124], acoustic emission testing [125,126], and resistance-based sensing [127,128]. Early approaches to in-situ damage sensing of carbon fiber-reinforced polymer composites took advantage of the inherent piezoresistivity of carbon fibers by monitoring the electrical resistance of the fibers during loading [129–132]. This

is commonly achieved using the four-probe resistance monitoring technique where a direct current is applied through the area under investigation while the resultant voltage across the same area is monitored. The impedance can then be calculated using Ohm's law. As damage, such as fiber fracture or delamination, occurs within the carbon fiber-based composite, the conductive pathways along the fiber are disrupted resulting in a measurable increase in the electrical impedance [129–132]. Moreover, different modes of damage are distinguishable by changing the direction of the resistance measurements. As fiber breakage is more detectable using measurements along the fiber axis, the detection of delamination is enhanced when performing measurements through the thickness of the composite [132]. However, such damage sensing approaches are limited to composites containing conductive fiber reinforcement, such as carbon.

To overcome this limitation, researchers have investigated carbon-based nanofillers, such as carbon black [127], graphene nanoparticles [133] and sheets [134], carbon nanotubes (CNTs) [127,128,135–137], and CNT paste [138] as means to introduce conductivity into traditionally insulating fiber-reinforced composites. For example, Alexopoulos et al. showed that adding CNT-based fibers between glass fabric plies adds piezoresistivity to an otherwise insulating composite [136]. The resultant modified glass fiber-reinforced composites were shown to exhibit a direct correlation between the electrical impedance and the applied tensile strain without any degradation of the mechanical performance when compared to the untreated composite [136]. However, CNTs present dispersion challenges due to their tendency to agglomerate as a result of van der Waals interaction, leading to non-uniform piezoresistivity and less than theoretical mechanical performance [139,140]. Sanchez et al. dispersed doped graphene nanoparticles within the uncured matrix of glass fiber-reinforced composites, which introduced conductive networks to detect deformation and damage [133]. The reported results conclusively show a correlation between the

resistance of the specimen and the crack length during Mode I and Mode II interlaminar fracture toughness testing [133].

In contrast to glass and carbon FRPCSs, multiple studies have focused on post-service damage assessment of aramid FRPCs, using methods which include ultrasonic air C-scan [141], micro computerized tomography [142], and laser Raman microprobe [143]. While these methods are capable of successfully detecting impact damage in aramid composites, all require the removal of the impacted area of the composite from the structure and additional sample preparation prior to employing the damage detection technique.

To overcome the need to remove the composite from service for damage assessment, researchers have developed methods using integrated sensors. Zivkovic et al. demonstrated in-situ damage sensing in aramid fiber-reinforced laminates by monitoring changes in optical signals through embedded fiber optic sensors [144]. However, integration of the fiber optic sensors within the composite requires extensive sample preparation and can produce a defect, which reduces material strength. Rosa et al. proposed another technique that used embedded polyvinylidene fluoride (PVDF) acoustic emission sensors that were used for in-situ damage detection in aramid fiber-reinforced composites [145]. Additionally, Groo et al. demonstrated the use of hydrothermally grown zinc oxide nanowires on aramid fibers with carbon fiber electrodes to detect multiple modes of damage by passively monitoring the voltage emission across a composite [146]. Dai et al. adopted a different approach, which modified the aramid FRPCs by coating the aramid fabric with carbon nanotubes to generate isotropic electrical conductivity. The researchers then measured the changes in electrical properties, which demonstrated a linearity in the piezoresistive responses due to elastic tensile and compressive strains, and plastic deformation [147]. Dai et al. also demonstrated the use of electrical impedance tomography, which was able to detect square

holes, narrow cuts, and progressive impacts. However the size and shape of these varying damage modes were not accurately represented [148]. Luo et al. used a spray coating method to fabricate single-walled carbon nanotube film sensors on glass fiber, polyaramid fiber, nylon fiber, and PET fiber and during the composite manufacturing process the SWCNT-FibSen provided real time monitoring and information during the resin curing process [149]. Rodriguez-Uicab et al. performed in-situ strain sensing on CNTs incorporated only into the matrix and coated on the aramid fibers along with dispersed in the matrix of aramid fiber-reinforced polypropylene composites. The researchers demonstrated that the CNTs during quasi-static and cyclic loading were capable of sensing tensile strain. It was also found that the composites containing CNTs in the matrix and on the fibers had higher piezoresistive sensitivity; however, the method to coat the aramid fiber was designed for individual fibers that required separation of fibers from the yarns and is not idea for larger scale production of woven aramid fabrics [150]. Nevertheless, these methods mentioned typically require more intensive sample preparation to incorporate damage detection capabilities that presents challenges in manufacturing and scale up for industrial use. Despite the widespread research on resistance-based sensing for carbon and glass fiber-reinforced polymer composites, similar efforts have not been widely used with aramid fiber-reinforced polymer composites, especially during ballistic impact.

1.6. Choice of Nanomaterials

While there is a wide variety of nanomaterial reinforcements reported in the literature, this dissertation focuses on the novel use of three nanomaterials: aramid nanofibers (ANFs), zinc oxide nanowires (ZnO NWs) and laser induced graphene (LIG). These nanomaterials reinforcements are used to improve the interfacial and inter-yarn properties of UHMWPE and aramid fibers with

scalable and efficient approaches. The synthesis, properties, and uses of each material are discussed below.

1.6.1. Aramid Nanofibers (ANFs)

Yang et al. proposed ANFs in 2011 as a polymeric nanoscale building block that could be utilized in a wide range of applications [151–153]. To generate ANFs, bulk aramid fibers are added to a basic DMSO/KOH solution and stirred to start the dissolution and deprotonation process. As shown in Figure 1.12, this process breaks apart the hydrogen bonds between the chains. Hydrolysis also takes place in the dissolution process and forms carboxylic acids and amines on the surface of the ANFs. The resulting large aspect ratio ANFs have the same crystal structure as precursor bulk aramid fibers and presumably, maintain the same (a) mechanical properties, (b) chemical properties, and (c) thermal resistance as macroscale aramid fibers. Unlike bulk aramid fibers, ANFs have increased surface reactivity with polar functional groups, such as carboxylic acids, carbonyls, and hydroxyls (Figure 1.12) [151,154]. The thermal decomposition of ANFs does not start until 536 °C and melting point is not detected until 300 °C, demonstrating the high thermal stability of ANFs is preserved [155]. The ANFs display outstanding water repellency, and provide high ultra-violet (UV) radiation protection [152] .

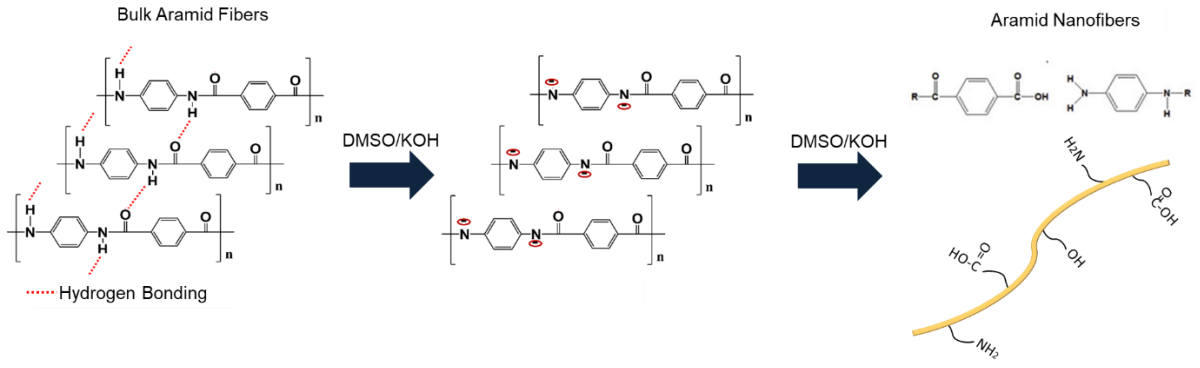

Figure 1.12. Dissolution and deprotonation process to obtain ANFs.

ANFs can form two-dimensional (2D) and three-dimensional (3D) nanoscale-based structures, such as nanofiller, films/nanopaper, coatings, aerogel fiber, particles/beads, and hydrogels. [152,153]. ANFs as nanofillers are used to blend and function as a network matrix material in a variety of other materials including polyethylene glycol [156,157], polyurethane [158], CNTs [159,160] graphene oxide [161–163], gold nanoparticles [164], and boron nitride nanosheets [165,166]. In addition, ANFs and their composites have been used in applications within many fields including, energy storage [167–170], battery separators [171,172], absorption and filtration [173,174], biomedicine [175–178] electromagnetics [179,180], electrical insulation [181], and infrared protection[182]. Taken together, ANFs are a widely-used nanomaterial with the potential to be integrated into a variety of large-scale production and demonstrates its multifunctional abilities.

ANFs have also been utilized as an interphase and as nanofillers in certain FRPCs to provide mechanical reinforcement. Lin et al. isolated ANFs in the form of a powder, which was then dispersed into an epoxy matrix to study the ANFs impact on the mechanical performance of the resulting nanocomposites [183]. The reported results showed that the ANFs were highly compatible with the epoxy matrix and yielded considerable improvements related to elastic properties and fracture toughness of the nanocomposites [183]. When the ANF-reinforced epoxy resin was used to fabricate aramid laminates using vacuum-assisted resin transfer molding (VARTM), the short beam strength (SBS) improved by 43%, and Mode I fracture toughness improved by 17% [184].

Nasser et al. used a dip-coating method instead to directly assemble ANFs onto the surface of aramid fibers by means of physisorption and hydrogen bonding, which resulted in a 70% and 25% increase in IFSS and SBS, respectively [185]. A similar dip-coating process was used to

directly assemble ANFs onto the surface of positively charged fiberglass through electrostatic adsorption, resulting in an 83% and 36% improvement in IFSS and SBS, respectively [186]. In the case of carbon fibers, Lee et al. used an electrophoretic deposition approach to assemble the ANFs onto the surface of the carbon fibers, which resulted in a 35% increase in IFSS [187]. The reported improvements in IFSS can be attributed to enhanced mechanical and chemical interactions between the fiber and the matrix due to the ANFs ability to increase both the roughness and chemical reactivity of the fiber surface.

1.6.2. Zinc Oxide Nanowires (ZnO NWs)

ZnO NWs have gained attention as a multifunctional material due to their attractive piezoelectric and semiconducting properties as well as their enhancement of the mechanical properties of the host composite [188]. ZnO NWs are a ceramic nanomaterial with a wurtzite crystal structure that is synthesized in mainly two classifications: a vapor phase and a solution phase. During the vapor phase, the ZnO NWs are synthesized at 500 to 2000 ^{o}C in a closed chamber where vapor of a desired material is generated by evaporation or chemical reduction. The vapor is then deposited on a solid surface substrate. The solution phase, on the other hand, is executed at lower temperatures (<200 ^{o}C) in a growth solution of aqueous solution, organic solution or a combination of an aqueous and organic solution, which offers enhanced flexibility for the use of organic and inorganic substrate [189].

ZnO NWs are used in a wide variety of applications such as sensing [190–194], energy harvesting [195–197], UV detection and shielding [198,199], field emission devices [200], solar cells [201–203] and photocatalysis [204]. Researchers have also demonstrated the effectiveness of ZnO NWs as a reinforcing material in fiber-reinforced composites [205–212], which is done by growing the ZnO NWs directly onto the fibers using a benign hydrothermal growth solution. Lin

et al. demonstrated that by providing enhanced mechanical interlocking abilities and increased surface area interaction, a ZnO NW interphase can improve the IFSS of carbon fiber-reinforced composites by 133% (Figure 1.13) [207]. ZnO NWs also reduce the stiffness gradient, resulting in a reduction of stress concentrations at the interface between the varying fiber and matrix material [213]. Galan et al. optimized the nanowire morphology and improved the IFSS of ZnO NW-reinforced carbon fiber composites by 228% [208]. Previous research has also demonstrated that the use of ZnO NWs can enhance the IFSS of aramid fiber-reinforced composites by 51% [210]. Swaminathan et al. reported that a ZnO NW interphase with a glass fiber reinforcement could increase the IFSS by 430% [212]. Nasser et al. evaluated ZnO NW-coated carbon and glass fiber-reinforced composites under varying strain rates during single-fiber pullout tests. This testing showed that the IFSS increased at low strain rates (benefiting structural performance) and decreased at high strain rates (beneficial under ballistic loading conditions), therefore demonstrating the use of ZnO NWs as a multifunctional interphase [205,206]. Taken together, these results highlight the use of a ZnO NW interphase to improve the IFSS of fiber-reinforced composites and indicate a potential reinforcement for UHMWPE fiber composites.

For soft body armor applications, Hwang et al. determined that ZnO NWs grown on woven aramid fabric can improve yarn pullout load by a factor of 23 and energy absorption capabilities by a factor of 11 [214]. The improved aramid fabric performance was due to the interlocking mechanism of the ZnO NWs and the buildup of the nanowires at the yarn crossover points [214,215]. The improved inter-yarn performance of ZnO NW-coated aramid fabrics was also explored by Malakooti et al., where a 66% improvement in the impact resistance of the fabric was reported [216]. Arora et al. demonstrated that the energy absorption capability of loosely-woven UHMWPE fabric can be improved with the use of ZnO nanorod grafting, and the energy

absorption capability of tightly-woven UHMWPE fabric can deteriorate when altered by the addition of these ZnO nanorods [217]. These studies demonstrate the potential of a ZnO NW interphase to improve the inter-yarn friction and ballistic performance of woven textile fabrics.

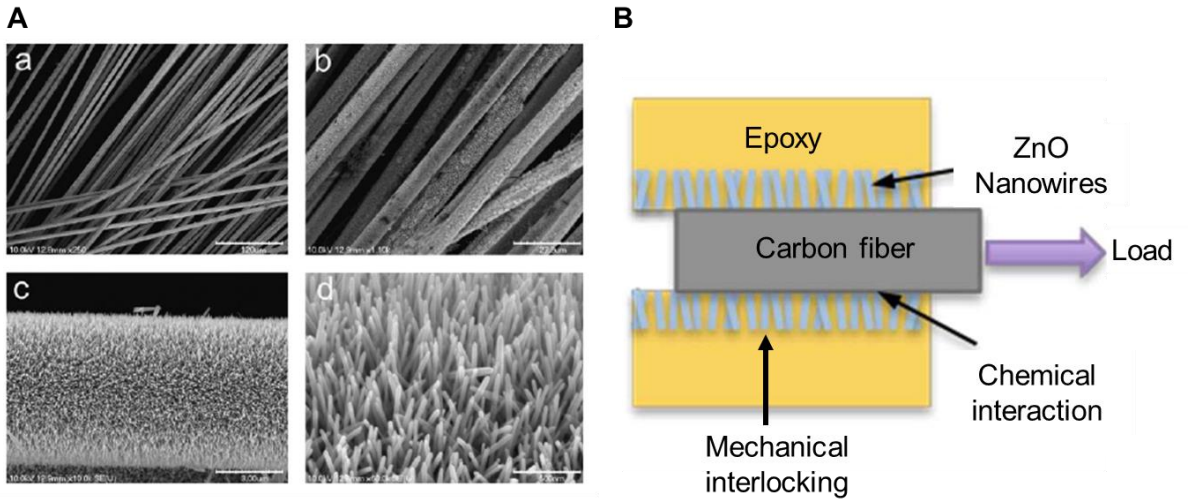

Figure 1.13. (A) SEM images of ZnO NWs grown on carbon fiber [207]. (B) Schematic of carbon fiber coated with ZnO NWs being pullout out from epoxy matrix [209].

1.6.3. Laser Induced Graphene (LIG)

A 3D porous graphene structure called laser induced graphene (LIG) has recently gained research traction due to the ease of production and inherent piezoresistivity [218]. The graphitic structure is obtained through the photo-thermal conversion of sp^3-carbon atoms in polyimide to sp^2-carbon using a commercial CO_2 infrared laser in an ambient environment, which results in a highly conductive, flexible surface with excellent thermal and electrical properties [218]. LIG films were characterize by X-ray diffraction (XRD), X-ray photoelectron spectroscopy (XPS) and Fourier-transform infrared spectroscopy (FTIR) which confirmed the presence of sp^2-carbon and Raman spectroscopy demonstrated a 2D band profile that is found in 2D graphene consisting of randomly stacked graphene layers and a high degree of graphitization was indicated by XRD. High resolution transmission electron microscopy (TEM) images showed an abundance of pentagon-

heptagon pairs, thus representing the ultra-crystalline feature of the LIG. By tuning the laser parameters such as power, speed and pulsing density, LIG with different morphology and microstructure can be produced [219]. Since its initial discovery and its ease of production, the potential applications of LIG have expanded to include joule heating [220], resistive memory devices [220], biomedical applications [221,222], flexible sensors [219,223], and composite strain sensors [220,224–226].

Although LIG is most commonly generated from polyimide films, Chyan et al. demonstrated that LIG could be directly formed on a wide variety of polymeric and non-polymeric surfaces, including aramid fibers, which can be exploited for the use in fiber-reinforced composites [221]. Recently, Nasser et al. reported that LIG directly printed on aramid fabric and LIG transfer printed onto carbon fiber prepregs exhibit an improved the fiber-reinforced composites short beam strength and Mode I interlaminar fracture toughness due to an increased interlocking mechanism and chemical interaction in the interlaminar region [227]. The application of LIG in structural health monitoring applications was recently investigated by Groo et al. who utilized LIG-coated aramid fabric as the reinforcement for self-sensing fiber-reinforced composites (Figure 1.14) [226]. The modified aramid-based composites were shown to be capable of tracking both tensile and flexural strain in addition to detecting tensile damage in-situ. Therefore, the combination of the piezoresistive properties of LIG and the ease of application with aramid fabrics presents a material with promising potential with regards to in-situ and resistance-based damage detection for aramid fiber-reinforced composites. However, up to this point, the ballistic impact performance and sensing capabilities of the LIG-coated aramid fabrics is yet to be investigated despite the traditional ballistic applications of aramid-based composites.

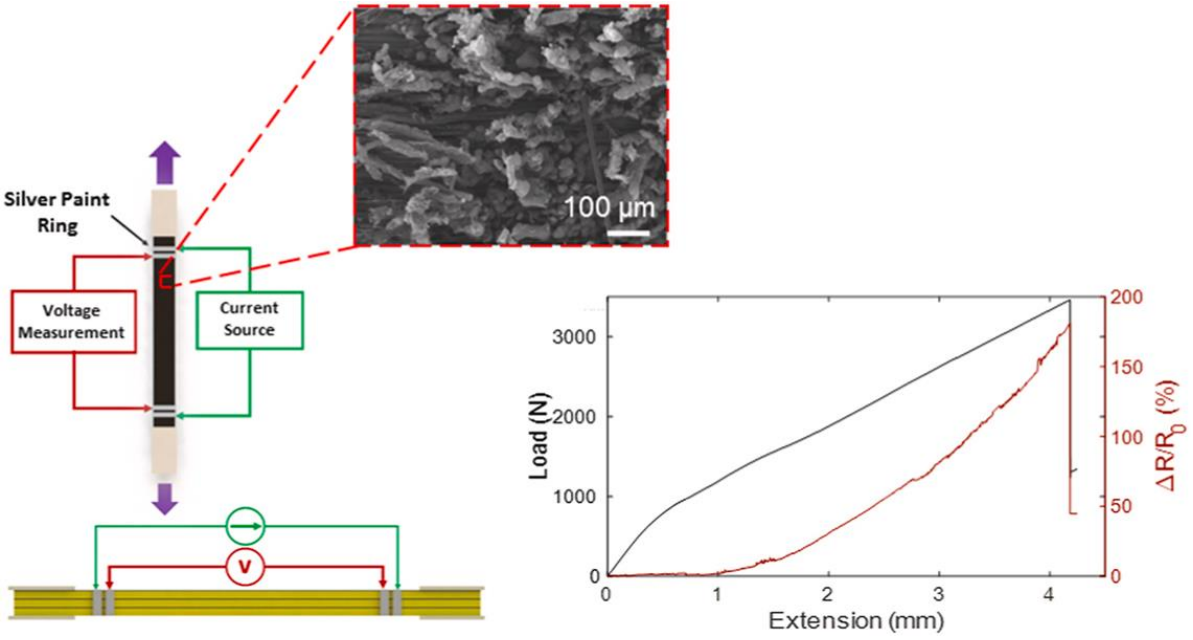

Figure 1.14. Schematic of the four point probe method of tensile test sample and SEM image of LIG-coated aramid composite along with the measured change in resistance and load under tension [226].

1.7. Overview of Research

This section describes the research conducted in each of the subsequent chapters. Chapter 2 explores the use of an ANF interphase to improve the fiber matrix interface in UHWMPE composites under quasi-static loading. The chapter starts with a review of the approaches to measuring the interfacial properties of FRPCs through single-fiber testing methods. The simple ANF dip-coating process for the assembly onto plasma functionalized UHMWPE fiber is then explained. The chemistry, morphology, and roughness of the ANF-coated fiber is characterized by Fourier-transform infrared spectroscopy (FTIR), X-ray photoelectron spectroscopy (XPS), scanning electron microscopy (SEM), and atomic force microscopy (AFM). The ANF-treated UHMWPE fibers displayed an increase in surface roughness and polar functional groups, which allowed for enhanced surface area interactions and chemical bonding with the epoxy matrix to improve fiber-matrix interactions. The structural integrity of the treated fibers was maintained and

assessed using single-fiber tensile testing, which demonstrated the benign nature of the treatment. The interfacial properties due to the introduced ANF interphase were evaluated through single-fiber pullout testing and a maximum increase of 173% in interfacial shear strength was measured through a combination of enhanced chemical interaction and mechanical interlocking. The findings in this chapter demonstrate that an ANF coating improves the interfacial properties of UHMWPE composites to maximize the production of high-performance UHMWPE fiber-reinforced composites.

In an effort to explore additional nanostructure interphases in UHWMPE composites, Chapter 3 examines the use of a ZnO NW interphase under quasi-static loading to improve the UHMWPE fiber-matrix interface. Prior to the hydrothermal growth of ZnO NWs on the UHMWPE fiber, the fiber surface was subjected to varying oxygen-plasma treatment durations to change the surface oxygen content to study the effect and improve ZnO NW adhesion. The post-functionalized surface chemical structure was examined using FTIR and XPS. The morphology and uniformity of the growth were characterized using a SEM. The benign nature of the surface treatment and ZnO NW growth was confirmed through single-fiber tensile testing. Using single-fiber pullout testing, the interfacial shear strength of UHMWPE composites with a 30-s oxygen-plasma treatment prior to ZnO NWs showed a maximum increase in IFSS of 135% through enhanced surface area interactions and mechanical interlocking between the fiber and the matrix. The findings in this chapter demonstrate that a simple oxygen-plasma functionalization and grafting of a ZnO NW interphase on the surface of UHMWPE fibers can significantly increase the IFSS of UHMWPE composites, and therefore, expand the use of UHMWPE FRPCs in structural applications.

Building on the findings of Chapter 3, Chapter 4 utilizes an oxygen-plasma functionalization and ZnO NW reinforcement in woven UHMWPE fabric to improve its inter-yarn friction and ballistic performance. The woven UHMWPE fabric was first oxygen-plasma functionalized to optimize the adhesion of the ZnO NWs to the surface of the fabric. Next, the surface chemistry was examined through XPS. The ZnO NWs were then grown using a hydrothermal growth process and the resulting nanowires were characterized using SEM and thermogravimetric analysis (TGA). The inter-yarn friction and pullout energy of the treated UHMWPE fabric were assessed using the yarn pullout method, which exhibited a maximum 664% increase in pullout load, and the pullout energy increased by 823% for ZnO NW-coated UHMWPE fabric that was treated with oxygen-plasma for 30 s. Due to the increase in inter-yarn friction, the V_{50} ballistic limit and energy absorption increased by a 59% and 227%, respectively, measured through projectile impact testing. The observed improved inter-yarn and impact performance can be attributed to mechanical interlocking and increased surface area provided by the ZnO NWs between neighboring yarns, which limits yarn movement during impact and improves resistance to pullout and penetration of the projectile. The findings from this chapter demonstrate a simple surface modification technique to yield-improved inter-yarn friction and ballistic performance of woven UHMWPE fabrics, which allows for further advancement and performance of the fabrics use in ballistic applications.

Chapter 5 investigates the use of LIG for improved ballistic and structural performance, in-situ impact damage and delamination detection in aramid FRPCs. First, LIG was directly generated on the aramid fabric using a laser printer before being fabricated into aramid laminates. The morphology of the LIG on the aramid surface was characterized using SEM. The interlaminar fracture toughness, evaluated using mode I interlaminar fracture toughness test and areal-density-

specific V_{50} evaluated using impact tests of the LIG aramid composites, increased relative to untreated aramid composites. This increase was due to the LIG providing an interlocking mechanism and increased surface area interactions between the fabric and matrix from the fibrous LIG microstructure that mechanically bridged the gap between adjacent plies. Using a four-point probe resistance monitoring method during ballistic impact, percent change in electrical resistance was found to correlate to the projectile impact velocity as s result of damage to the LIG interface from fiber breakage and delamination. Monitoring change in resistance during Mode I interlaminar fracture toughness testing, results showed strong correlation between change in resistance and generated delamination length and rate of growth. It was demonstrated that the LIG exhibits multifunctionality in both reinforcing the interface between plies while also enabling in-situ structural health monitoring of this failure-prone area within fiber-reinforced composites. The findings in this chapter demonstrate a simple and effective technique to generate a LIG interface in aramid-based composites to improve structural performance and imbedded sensing of damage and delamination.

The final chapter of this dissertation summarizes the key findings and results of the work discussed throughout this dissertation. After the overview, the main contributions of this dissertation are discussed and their influence on future research, advancing the use of nanostructured-based surface modifications on the field of ballistic materials, and advancing the use of UHMWPE composites in structural applications. Finally, suggestions for future work building on findings in this dissertation are presented in the final section of this chapter.

Chapter 2. Aramid Nanofiber Interphase for Enhanced Interfacial Shear Strength in Ultra-High Molecular Weight Polyethylene/Epoxy Composites

2.1. Chapter Introduction

Applications of ultra-high molecular weight polyethylene (UHMWPE) fiber in structural composites are limited due to the fiber's chemically inert and smooth surface, which results in poor adhesion with matrix materials and ultimately affects the overall mechanical properties of the composite. In order to combat the poor bonding of the UHMWPE to matrix materials, prior research has shown that multi-scale modification of the fiber surface using nanomaterials is a promising approach to improve the interfacial properties of composite materials, which uses a combination of mechanical interlocking and chemical interactions. The focus of this chapter is the use of an aramid-based nanomaterial interphase to improve the interfacial properties of UHMWPE composites for structural applications.

In this work, the effectiveness of a simple dip-coating process for the assembly of an aramid nanofiber (ANF) interphase onto the surface of plasma-treated UHMWPE fibers is demonstrated. The ANF dip-coating treatment increases the surface roughness of UHMWPE fibers and populates them with polar functional groups, which allows for enhanced chemical bonding with the epoxy matrix. The chemical composition of post-treatment UHMWPE fiber surface was characterized using Fourier-transform infrared spectroscopy (FTIR) and X-ray photoelectron spectroscopy (XPS), and was found to exhibit an increase in polar functional groups. Through scanning electron microscopy (SEM) and atomic force microscope (AFM), the UHMWPE fiber surface was found to have an increased roughness, which is desirable for a stronger interfacial interaction via

mechanical interlocking between the fiber and the matrix. Through single-fiber pullout testing, the interfacial shear strength (IFSS) was observed to increase when an ANF interphase was introduced while maintaining the tensile strength of the treated UHMWPE fibers. The performance of the interphase was enhanced by varying the ANF dip-coating treatment periods. These results demonstrate a simple and cost-efficient technique to improve the interfacial properties of UHMWPE composites through the introduction of an ANF fiber surface reinforcement.

2.2. Review on Micromechanical Interfacial Testing Methods

The interphase between the fiber and matrix is a highly important factor in the development of fiber-reinforced polymer composites (FRPCs) since it has a critical impact on the overall strength of the composites. For this reason, there has been a variety of methods to measure the fiber-matrix adhesion, where some methods are for larger scale composites and others are for single-fiber composites. However, for a more direct assessment of adhesion, specifically the IFSS, it is generally accepted that the single-fiber composite test is the most suitable approach [228,229]. Although there is no set standard for measuring the IFSS, the four common methods used are single-fiber fragmentation (SFF) [210], single-fiber pushout [230], micro-droplet [231–233], and single-fiber pullout (SFP) [198].

In a SFF test, a single fiber is embedded into a polymer matrix and is loaded in tension, as depicted in Figure 2.1A. As the specimen is loaded and elongated, stress is transferred to the fiber, and once it reaches its tensile strength, the fiber begins to fracture until fiber fracture saturates [234,235]. The IFSS is then calculated based a shear-lag analysis using the tensile strength of the fiber at a critical length and the maximum number of fiber fractures [236]. The test is usually performed under polarized light, which enables the operator to view brightly colored distributions at the fiber fractures; however, when unusual fiber failure patterns occur, it can be difficult to

determine, measure, and analyze the fiber fractures [237]. Thus, the SFF test is limited to transparent matrix materials, and is not suitable for high failure strength fibers since the matrix may yield prior to fiber fracture saturation [238,239].

Single-fiber pushout is another method and is shown in Figure 2.1B. By using a nanoindenter, single fibers are pushed out of a flat matrix specimen, and the corresponding force applied is measured [230,240]. This test has some advantages of being able to test multiple fibers prepared in one specimen, which allows this to be a fast-testing method as well as a clear demonstration of debonding failure. However, there can be non-uniform contact between the probe and the fiber that causes destruction of the fiber from the concentrated compressive stress. Thus, this method is not suitable for soft polymer fibers where the indenter can potentially damage the soft fiber instead of pushing it out of the matrix [238].

The third technique is the micro-droplet test where a small droplet of polymer matrix is deposited on a single fiber and then threaded between two jaws of a microvice as shown in Figure 2.1C. As the fiber is pulled, the droplet is caught and held by the microvice until the fiber debonds and is pulled out from the matrix [232]. Great care must be taken for a variety of parameters during sample preparation such as of the droplet length and shape, and dragging of the droplet which can create an undesired film on the fiber which dictates loading conditions, leading to high variability and inaccurate measurements of the collected data [233,238]. The small volume used for the droplet changes the curing kinetics of the polymer matrix, which can affect the legitimacy of the data collected [241,242].

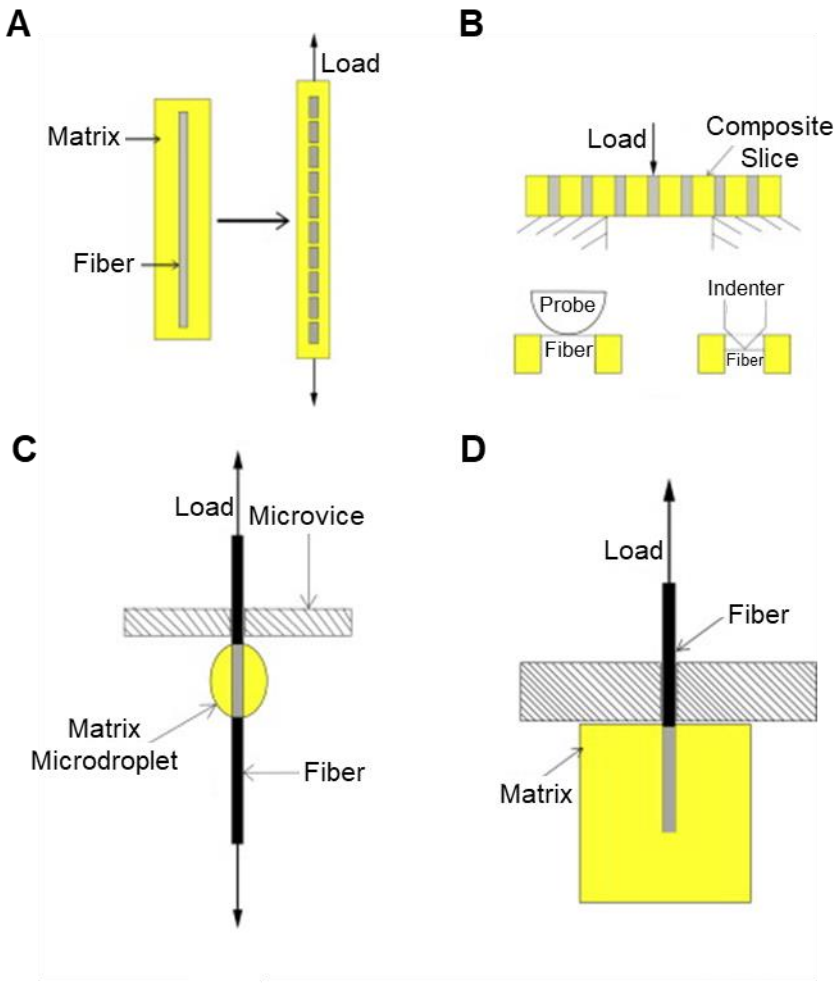

Figure 2.1. Schematics of singe fiber composite micromechanical tests to determine the interfacial shear strength for (A) single-fiber fragmentation, (B) single-fiber pushout, (C) micro-droplet, and (D) single-fiber pullout [228].

The final alternate method is SFP, where a single fiber is embedded into a polymer matrix block at a predetermined length, and an external force is applied to the free end of the fiber to achieve fiber pullout, as shown in Figure 2.1D [236,243,244]. The simple and easy design along with the catastrophic nature of the failure at the fiber matrix interface makes SFP a good candidate for the measurement of interfacial properties [229,245]. Therefore, in this research, SFP will be used to measure the IFSS of the composites. The IFSS (τ) of a specimen during SFP test is expressed as [243]:

$$\tau = \frac{F}{\pi d l} \tag{2.1}$$

Where F is the peak load when pullout occurs, d is the diameter of the fiber, and l is the embedded fiber length. The embedded length is adjusted so that fiber pullout occurs instead of tensile failure of the fiber. Using the applied load to calculate the tensile stress (σ_f) which can be expressed as:

$$\sigma_f = \frac{F}{\pi r^2} \tag{2.2}$$

where r is the radius of the fiber. The maximum possible embedded length of the fiber inside the polymer matrix can be determined by combining Equations 2.1 and 2.2 and expressed as:

$$l = \frac{r\sigma_f}{2\tau} \tag{2.3}$$

Therefore, considering the tensile strength (~ 3 GPa), diameter (~ 40 μm) and the IFSS (~ 3 MPa) of UHMWPE fibers, the maximum embedded length is calculated as ~ 10,000 μm. However, to ensure fiber pullout and accuracy of the test results, a safety factor of 10 is used so the actual embedded length was kept shorter than 1000 μm. To eliminate the possibility of cross-sectional effects having an impact on the measurements, the embedded length should not be less than 50 μm [244]. Hence, the SFP interfacial testing method can yield clear debonding failure, which allows for direct and accurate measurement of the IFSS of a composite.

2.3. Assembly of ANF onto UHMWPE Fiber Surface

UHMWPE plain-weave fabric (Spectra® fabric style 932 received from Saati) was cleaned using successive sonication for 30 min in acetone and ethanol and then dried in an oven at 80°C for 1 hour. Following cleaning, the fabric was oxygen-plasma treated inside a SPI Plasma Prep II with an oxygen atmosphere (99.6% purity) for 30 s to introduce oxygen functional groups. Individual fibers were then removed from the woven fabric and partially attached to Teflon frames

using 5-min epoxy, leaving one end of the fiber hanging free, as shown in Figure 2.2. A 0.2 wt% ANF solution was prepared according to the dissolution and deprotonation method described by Yang et al. [151]. Macroscale aramid fibers were dissolved in a DMSO/KOH solution and stirred at 350 revolutions per min (rpm) at room temperature until the aramid fibers were completely dissolved. The solution was then poured into a 500 ml beaker and the Teflon frame was submerged in the beaker for treatment periods of 1, 3, 5, and 7 min (see Figure 2.2). Once the dip-coating process was completed, the fibers were rinsed in water and dried in a vacuum oven at 60 °C for 24 hours.

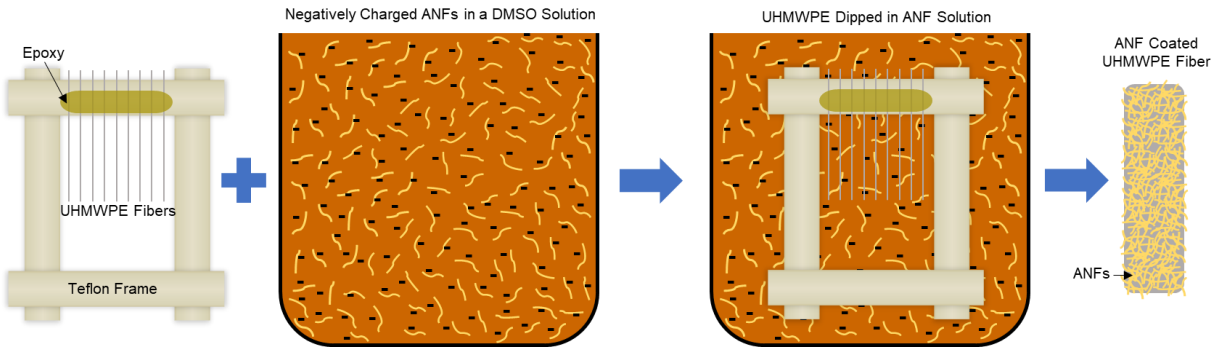

Figure 2.2. Schematic of the ANF dip-coating treatment process.

2.4. Surface Characterization

The chemical structure and composition of the ANF-coated fiber surface was characterized by Fourier-transform infrared spectroscopy (FTIR) and X-ray photoelectron spectroscopy (XPS). The UHMWPE surface morphology was characterized by scanning electron microscopy (SEM), and the surface roughness was measured by atomic force microscopy (AFM).

2.4.1. FTIR Characterization of ANF on the UHMWPE Fiber Surface

Following the ANF dip-coating process, the surface chemistry and morphology of the UHMWPE fibers were characterized using multiple techniques. To confirm the presence of ANFs and characterize the chemical structure of the ANF interphase on the surface of the UHMWPE

fibers, FTIR was performed using a Nicolet iS60 spectrometer (Thermo Scientific) with a SMART diamond iTR accessory.

FTIR was used to investigate changes in the chemical structure of the UHMWPE fiber surface post-plasma and ANF dip-coating treatments. FTIR was performed on the ANF-coated UHMWPE fibers with various treatment periods of 1, 3, 5, and 7 min (see Figure 2.3A). As shown in Figure 2.3B, the surface plasma treatment performed prior to the ANF coating yields new oxygen-based functional groups at 1735 cm^{-1} and 1110 cm^{-1}, which correspond to C=O and C-O-C, respectively [246]. The addition of these oxygen groups on the originally inert UHMWPE fiber surface can potentially enable a higher degree of chemical interaction between the fiber and polar ANFs. Once an ANF interphase is introduced, the FTIR spectra of the treated fibers displayed distinct ANF absorbance peaks which correspond to C=O stretching (1648 cm^{-1}), C-N stretching (1542 cm^{-1}), C=C stretching (1523 cm^{-1}), and Ph-N stretching (1316 cm^{-1}), irrespective of treatment periods (see Figure 2.3A). In addition, all of the treated fibers displayed polyethylene absorbance peaks, which correspond to C-H stretching (2914 cm^{-1}, 2848 cm^{-1}, 1472 cm^{-1}, and 716 cm^{-1}). The results confirmed that the dip-coating process successfully produces an ANF coating on the fiber surface. The results also confirmed the addition of polar functional groups on the surface of the UHMWPE fiber due to the ANFs, which have been previously demonstrated to be compatible with epoxy functional groups, therefore providing a mechanism to improve chemical interactions at the fiber-matrix interface [183,184]. It should be noted that no significant polyethylene absorbance peak shifts were observed, which confirms the fiber treatment does not damage the fiber's chemical structure. When comparing the ANF dip-coating treatment period (see Figure 2.3C), the absorbance peaks corresponding to C=O stretching, C-N stretching, C=C stretching, and Ph-N stretching are found to increase with increased soaking. The increase in

absorbance peaks signals a correlation between the amount of ANFs introduced onto the fiber surfaces and treatment period.

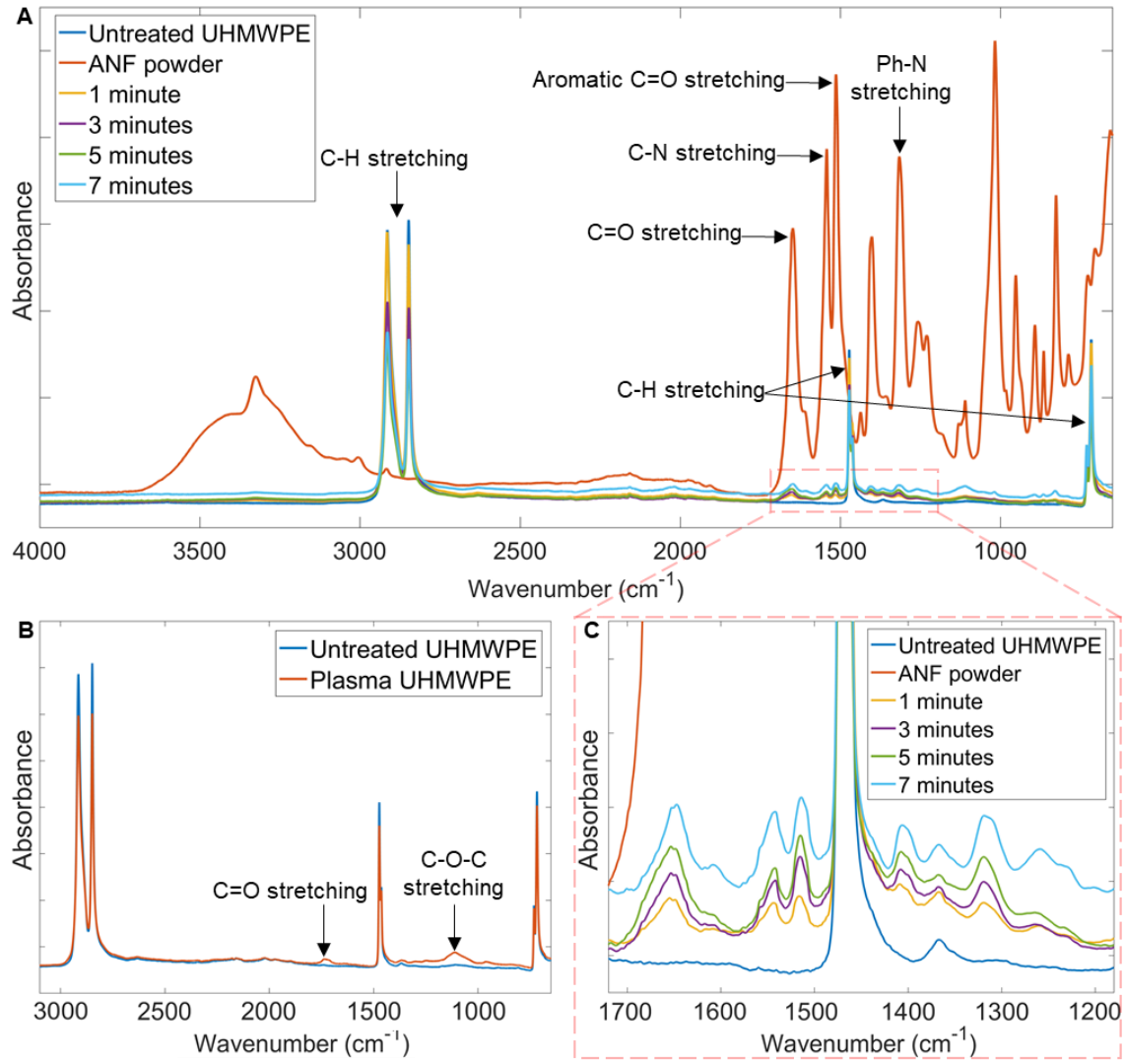

Figure 2.3. (A) FTIR spectra of untreated UHMWPE, isolated ANFs, and ANF-coated UHMWPE fibers for various treatment periods. (B) FTIR spectra of untreated UHMWPE and 30 s plasma-treated UHMWPE. (C) FTIR spectra of untreated UHMWPE, isolated ANF, and ANF-coated UHMWPE fibers for various treatment periods with wavelengths ranging between 1715 cm^{-1} and 1190 cm^{-1}.

2.4.2. XPS Characterization of ANF on the UHMWPE Fiber Surface

The changes to the chemical composition of the fiber surface due to the introduced ANFs were characterized using XPS obtained from a Kratos axis ultra XPS. A broad spectra and C1s spectra

were obtained and decomposed using CasaXPS software that utilized a Marquette regression function to create deconvoluted peaks of 70–30% Gaussian-Lorentzian distributions with the full-width, half max constrained to 0.8-1.7 eV and energy bands of 284.5-285.5, 285.5-287.0, 286.5-288.0 and 288.0-290.0 eV were fitted. Each peak corresponds to a different moiety, for C-C (carbon) , C-N (amine), C=O (ketone), and COOH (carboxyl) bonds, respectively [247,248].

XPS analysis was used to further investigate the chemical composition of the UHMWPE surface following the plasma and ANF dip-coating processes. The XPS broad spectra concentrations of carbon, oxygen, and nitrogen of untreated, plasma-treated, and ANF-coated fibers are shown in Table 2.1. Post-plasma treatment, the UHMWPE fiber surface oxygen content was increased considerably from 6.41% to 15.2%. Once ANFs were introduced, the fiber surface was found to be enriched with up to 7.53% nitrogen when compared to the untreated and plasma-treated samples, which both measured at 0% nitrogen. The addition of nitrogen is a result of aramid's amide bonds and confirms the presence of an ANF coating on the UHMWPE fiber surface.

Table 2.1. Broad XPS survey concentrations of overall carbon, nitrogen, and oxygen contents of untreated, oxygen-plasma treated, and ANF-coated UHMWPE fiber surfaces.

UHMWPE Fiber	C%	O%	N%
Untreated	93.59	6.41	0.00
Plasma-treated	84.17	15.20	0.00
ANF-coated	82.56	9.91	7.53

The normalized C1s XPS spectra of untreated UHMWPE, ANF-coated UHMWPE fibers for various treatment periods, and isolated ANF powder are shown in Figure 2.4. Figure 2.4 shows that the ANF-coated UHMWPE surface exhibits similar chemical composition peaks to that of the

ANF powder, confirming the presence of ANFs on the fiber surface. The C-C (carbon) and C=O (ketone) peaks decrease while the C-N (amine) and COOH (carboxyl) peaks increase with increased treatment periods. After a 7-min treatment period, the C1s spectra is similar to the ANF powder, which is likely caused by the ANF coating exceeding the interaction volume of XPS during the longer soak times. The decomposed C1s energy state concentrations of the ANF-coated fibers for various treatment periods are shown in Table 2.2. The presence of oxygen functional groups on the fiber surface after the ANF treatment presents the potential to enhance the chemically interaction at the fiber-matrix interface.

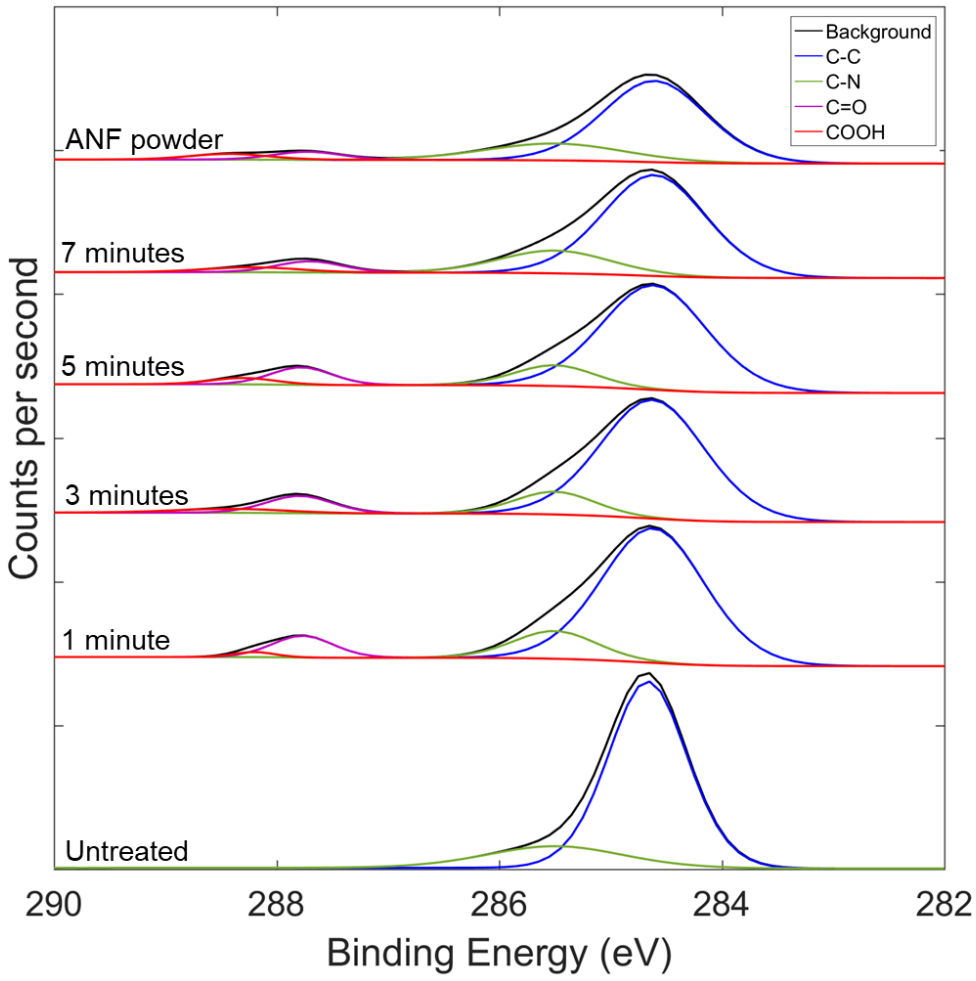

Figure 2.4. C1s XPS spectra of untreated UHMWPE, ANF-coated UHMWPE fibers for various treatment periods and ANF powder, deconvoluted by existing carbon states.

Table 2.2. XPS decomposed C1s energy state concentrations for ANF-coated UHMWPE fibers for various treatment periods compared to isolated ANF powder.

Treatment periods (min)	C-C% (Carbon)	C-N% (Amine)	C=O% (Ketone)	COOH% (Carboxyl)
1	78.31	13.03	7.47	1.18
3	78.53	11.44	7.24	2.79
5	77.66	11.89	7.55	2.90
7	73.53	17.93	5.25	3.20
ANF Powder	71.51	20.00	4.68	3.82

2.4.3. SEM of ANF Coated UHMWPE Fiber Surface

The ANF-coated UHMWPE fiber-surface morphologies were SEM imaged using a JEOL 7800 FLV. SEM images were used to investigate the surface morphology of the UHMWPE fibers following ANF dip-coating. As shown in Figure 2.5A-B, the untreated fiber surface displayed a smooth texture, which does not provide the opportunity for mechanical interlocking between the matrix and fiber. As a result, the interfacial interaction was primarily dominated by chemical bonding. However, UHMWPE has a naturally inert surface that does not offer opportunities for chemical bonding between the fiber and matrix. Following a one-min ANF dip-coating treatment, the fiber surface was found to display a rougher morphology due to adsorption of entangled ANFs (see Figure 2.5C-D). As the treatment period was increased to 3 min, the ANF coating was found to densify and completely cover the fiber surface, forming a complete ANF interphase. As shown in Figure 2.5G-J, once the treatment period was increased to 5 min or longer, signs of ANF surface agglomerations began to appear, yielding non-uniform and porous coatings.

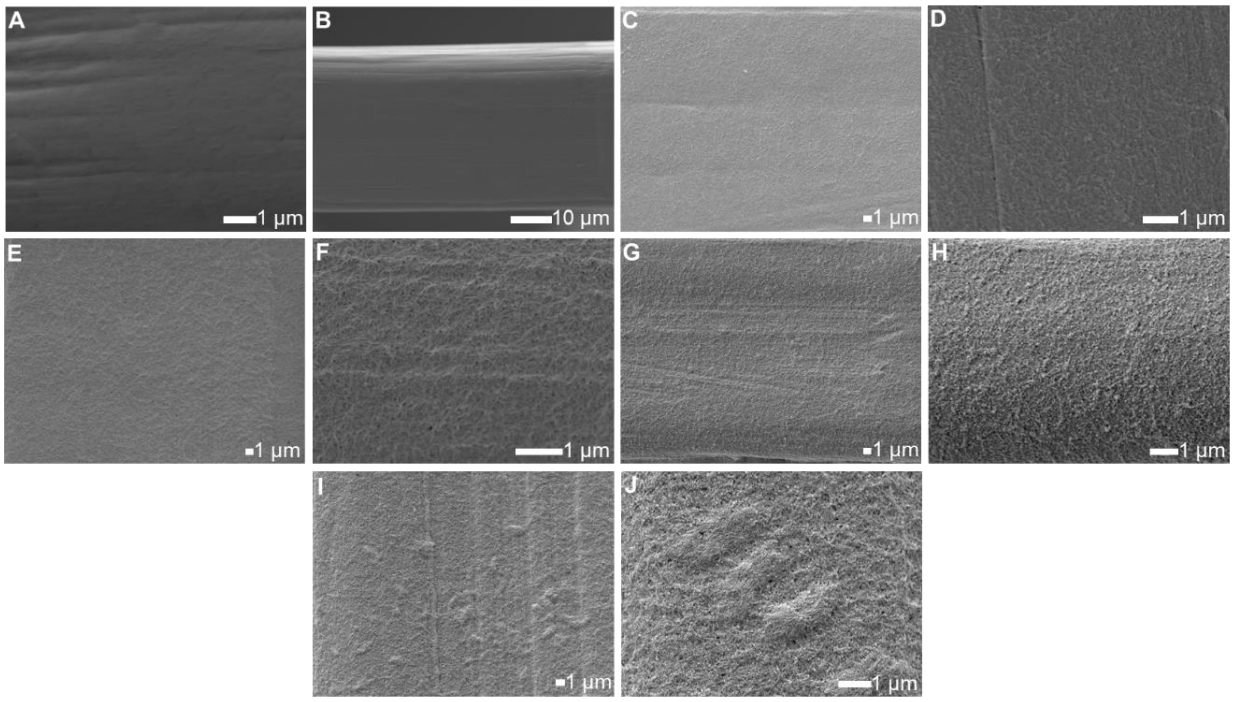

Figure 2.5. SEM images of untreated UHMWPE and ANF-coated UHMWPE fiber surfaces for varying treatment periods. (A-B) Untreated UHMWPE fiber surface. (C-D) 1-min treatment period. (E-F) 3-min treatment period. (G-H) 5-min treatment period. (I-J) 7-min treatment period.

2.4.4. AFM of ANF Coated UHMWPE Fiber Surface

The surface roughness of the fiber was measured using a Park Systems XE-70 AFM in non-contact mode. The ANF-induced changes in surface morphology were also quantified using AFM characterization. In agreement with SEM imaging, Figure 2.6 displays a significant increase in fiber surface roughness with increasing treatment periods. Both the root-mean square (RMS) (*Rq*) and the average roughness (*Ra*) of the fiber surface were measured using XEI (PSIA Corporation) analysis software (see Table 2.3). Both *Rq* and *Ra* of ANF-coated UHMWPE fibers were found to increase with increasing treatment period, reaching a maximum increase of 267% and 227% after a treatment period of 7 min, respectively. The roughened surface as shown in the SEM images and AFM scans due to the ANF coating yields a larger interaction surface area between the fiber and matrix and provides the opportunity for mechanical interlocking, which can

contribute to strengthening the interfacial adhesion within UHMWPE composites. The large increase in surface roughness shown after 5 and 7 min can signify the formation of agglomerations and a non-uniform surface, which are expected to be undesirable since they can hinder the resin from properly wetting the fiber surface, and ultimately cause interfacial defects and voids that have the ability to reduce the interfacial strengthening effect of the proposed interphase.

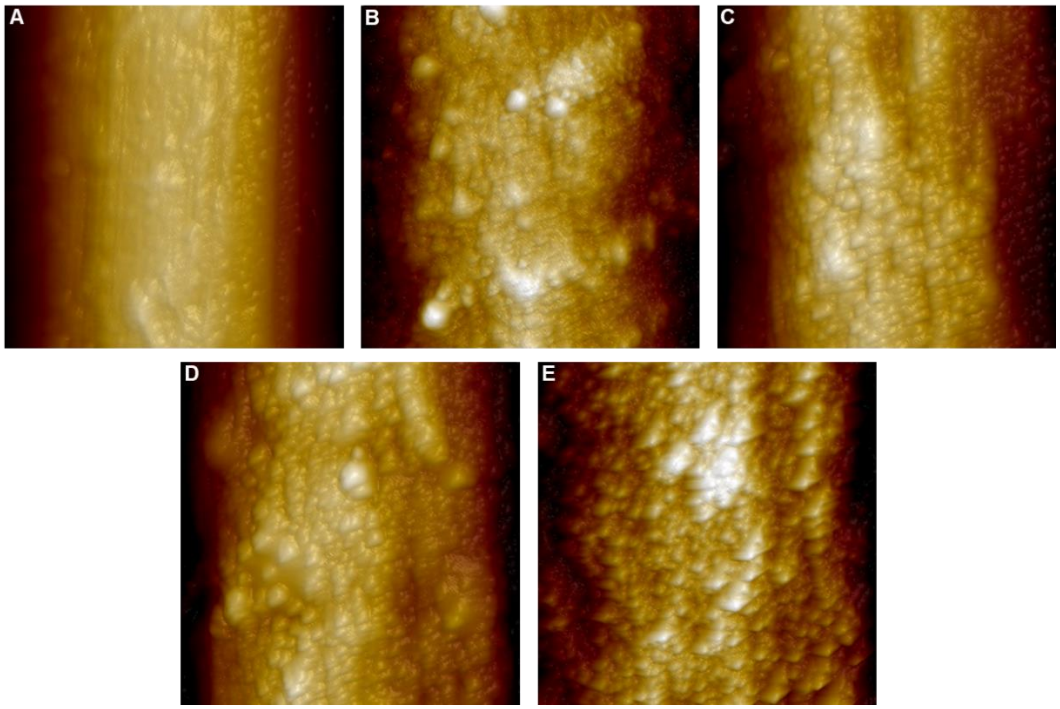

Figure 2.6. Non-contact surface AFM scans of (A) untreated and ANF-coated UHMWPE fiber surfaces at (B) 1-min, (C) 3-min, (D) 5-min, and (E) 7-min shows increased surface roughness with increased treatment periods.

Table 2.3. Measured RMS Rq and Ra of untreated UHMWPE and ANF-coated UHMWPE with varying dip-coating treatment periods.

Treatment period (min)	R_q (nm)	R_a (nm)
Untreated	12	11
1	19	15
3	27	24
5	37	32
7	44	36

2.5. Mechanical Tests

The structural integrity of the treated fibers was assessed using single-fiber tensile testing, while changes in interfacial properties due to the introduced ANF interphase were evaluated through single-fiber pullout testing.

2.5.1. Fiber Tensile Strength Measurement

2.5.1.1. Single-fiber tensile test experimental setup

To ensure the structural integrity of the UHMWPE fibers was not compromised during the ANF dip-coating process, single-fiber tensile tests were performed according to ASTM C-1557 [249]. Due to the inert surface of the untreated fiber and the fiber's tendency to slip through the tabs during testing, a modified tensile testing method was used. The ends of individual UHMWPE fibers were sandwiched between two 38 mm x 13 mm pieces of sandpaper using high shear strength epoxy (Loctite® 9430™ Hysol®) cured at 82°C for 1 hour, such that a gauge length of 12.7 mm was attained (see Figure 2.7). The samples were then tested with a 5-N load cell on a 5982 Series Instron load frame at a rate of 0.05 mm/s. To avoid slippage during testing, alligator clips were used to clamp the tabs into place.

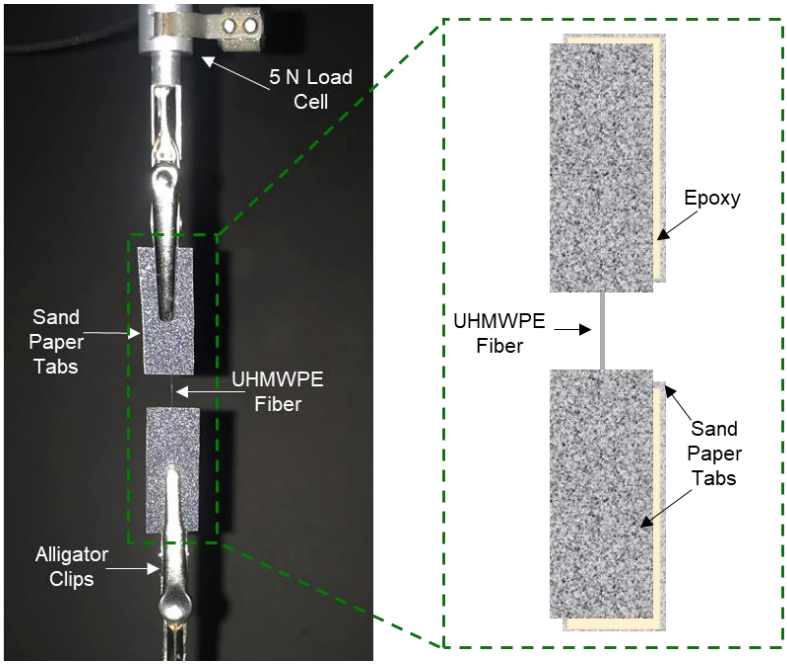

Figure 2.7. Schematic of a single UHMWPE fiber tensile test specimen.

2.5.1.2. Single-fiber tensile test results

A critical component of any proposed fiber surface treatment is to ensure that the structural integrity of the fiber is not affected by the interfacial enhancement method. To confirm that the ANF dip-coating process does not degrade the mechanical strength of the UHMWPE fibers, single-fiber tensile tests were performed, at least 10 samples per treatment period. As shown in Figure 2.8, the tensile strength of the untreated and ANF-coated fibers was found to have no statistical difference, regardless of treatment period. The lack of statistical difference is expected since the short dip-coating treatment period used in this dissertation limits the exposure of the polymeric fibers to the basic ANF/DMSO solution and avoids damaging the fibers due to chemical exposure. The conservation of the tensile properties in the fibers following ANF dip treatment is consistent with previously reported studies [155,185,186].

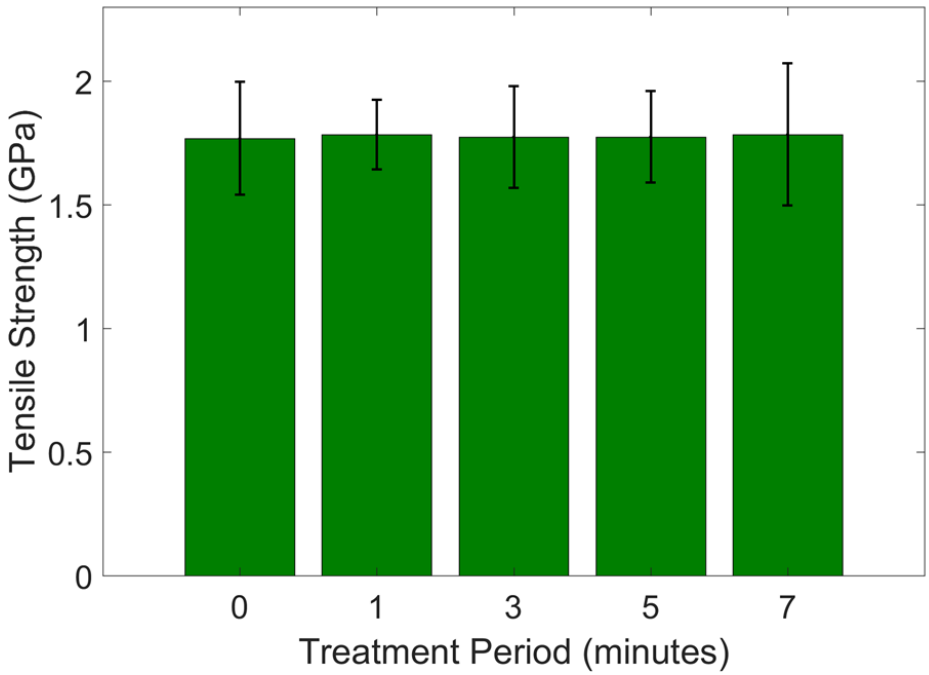

Figure 2.8. Tensile strength of untreated and ANF-coated UHMWPE single fibers.

2.5.2. Interfacial Shear Strength Measurements

2.5.2.1. Single-fiber pullout test setup

To evaluate the IFSS of the ANF-coated UHMWPE fibers, single-fiber pullout tests were performed. Individual treated fibers were inserted into a slit of a silicon mold, where the embedded length was less than 300 μm, verified with an optical microscope [116,250]. The silicon molds were filled with an Epon 862 and Epikure 3230 epoxy mixture at a weight ratio of 100:35 and cured at 80°C for 8 hours. Following the curing process, the samples were removed from the silicon molds and tabs were added to the free end of the fiber using the same Epon 862/Epikure 3230 resin mixture. A schematic of the sample preparation process is shown in Figure 2.9A. After the resin mixture was applied for the tabs, the fiber was cured at 80°C for 8 hours. Large epoxy tabs were used so that the tabs could be sufficiently gripped and to ensure fiber pull out before slipping in the tab could occur. The single-fiber pullout test was performed on a 5982 Series Instron frame

equipped with a 5-N load cell at a displacement rate of 0.016 mm/s. To avoid slippage during testing, alligator clips were used to clamp the tabs into place (see Figure 2.9B). It should be noted that if slipping was observed, the data was deemed invalid and excluded from the results.

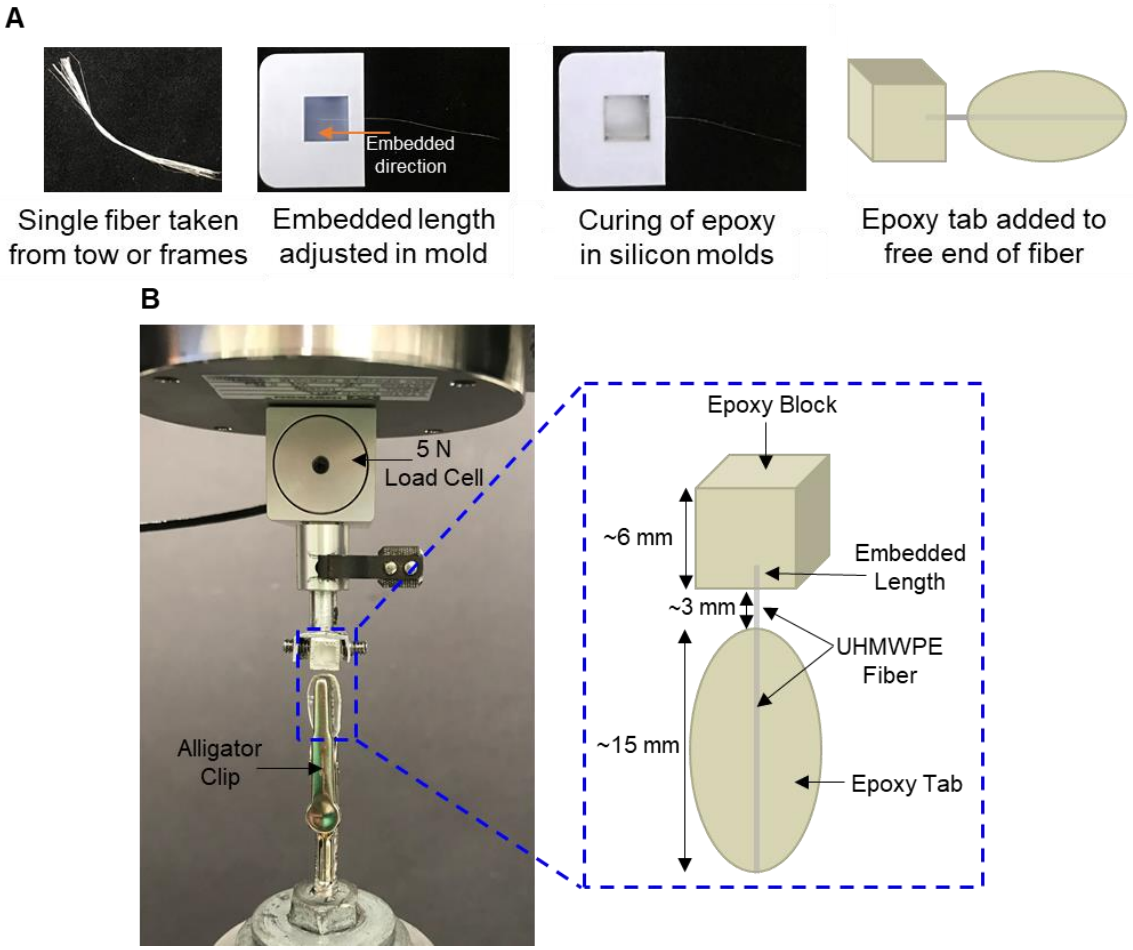

Figure 2.9. Single-fiber pullout (A) schematic of specimen fabrication process and (B) experimental setup.

2.5.2.2. Single-fiber pullout test results

Given the importance of interfacial adhesion to the overall performance of composite materials, single-fiber pullout testing was performed to evaluate the IFSS of the ANF-coated UHMWPE fibers. Pullout testing allows the direct measurement of the interfacial debonding force between an individual fiber and the matrix [244,245]. The measured IFSS of untreated and ANF-coated fibers are shown in Figure 2.10 where at least 10 samples were tested for each treatment

period, and after only a 1-min treatment, the ANF-coated fibers (6.97 MPa) displayed a 123% increase in IFSS relative to untreated fibers (3.12 MPa). Interfacial adhesion was further improved after a 3-min treatment, where an 173% increase in the IFSS of ANF-coated fibers (8.51 MPa) was measured, relative to untreated fibers. The increased fiber surface roughness due to the ANFs coating allows for the fiber to be firmly embedded into the epoxy matrix, increasing interfacial surface area and enhancing the mechanical interlocking mechanism between the fiber and the matrix. By hierarchically nano-structuring the fiber-matrix interface, the ANF interphase contributed to a reduction in interfacial stress concentration and an improvement in load transfer between the typically smooth fiber and epoxy matrix. As the treatment period was increased to 5 and 7-min, the IFSS of the ANF-coated fibers experienced a 11% and 20% decrease in IFSS, respectively, relative to those samples treated for 3-min. This decrease can be attributed to a non-uniform and porous coating, as well as the formation of ANF agglomerations on the fiber surface (see Figure 2.5G-J).

Such fiber surface characteristics can increase the density of defects at the interface and act as site for failure initiation, thus introducing discontinuity within the interfacial region and ultimately yielding a lower IFSS in UHMWPE composites [186,187]. It should be noted that, irrespective of the treatment period, the IFSS was substantially increased relative to untreated fibers. The ANF interphase promoted a greater degree of chemical bonding between the typically inert UHMWPE surface and the epoxy matrix. The chemical interaction between the ANFs polar functional groups and the polar groups found in the epoxy matrix were enabled, which allowed for improved surface wetting and chemical bonding between the ANF-coated fibers and the epoxy matrix. These results show that the use of a dip-coating method to introduce an ANF interphase

on the surface of UHMWPE fibers is an effective method to improve interfacial adhesion in the fiber's corresponding epoxy matrix composites.

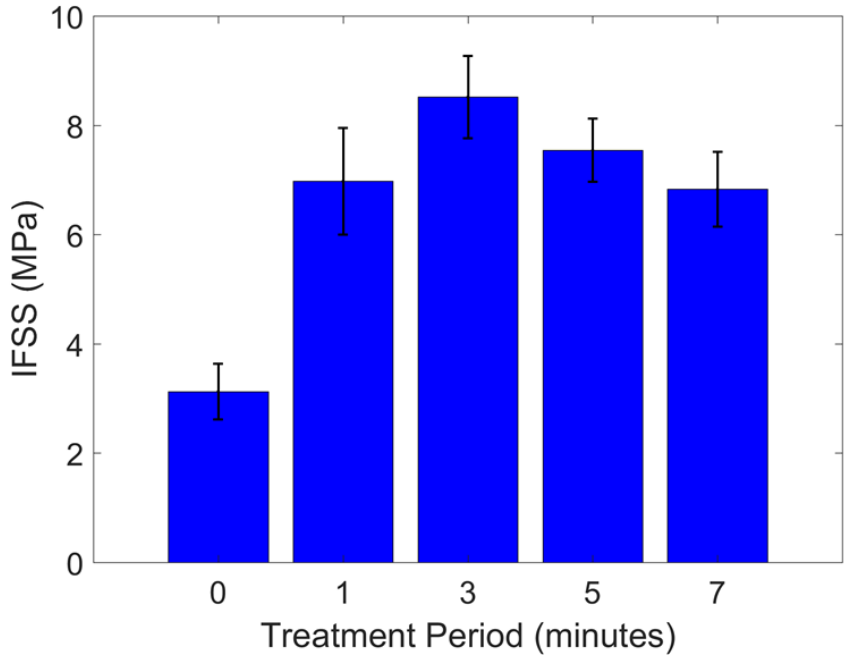

Figure 2.10. Single-fiber pullout IFSS measurement of untreated and ANF-coated UHMWPE fibers for various treatment periods.

2.5.2.3. Post-pullout SEM failure analysis

Post-pullout SEM imaging was performed to further understand the interfacial failure mechanism where the UHMWPE fibers displayed a smooth, clean, and ANF-free surface (see Figure 2.11). As shown in Figure 2.5A-D, the fiber surfaces were originally coated with an entangled ANF interphase that provided a roughened surface morphology. Due to the larger interaction area between the ANFs and the epoxy matrix when compared to the ANFs and the fiber, the ANFs debonded from the fiber surface and remained embedded in the epoxy matrix, as demonstrated in Figure 2.11E. Therefore, the resulting interfacial failure is observed at the ANF-UHMWPE fiber interphase.

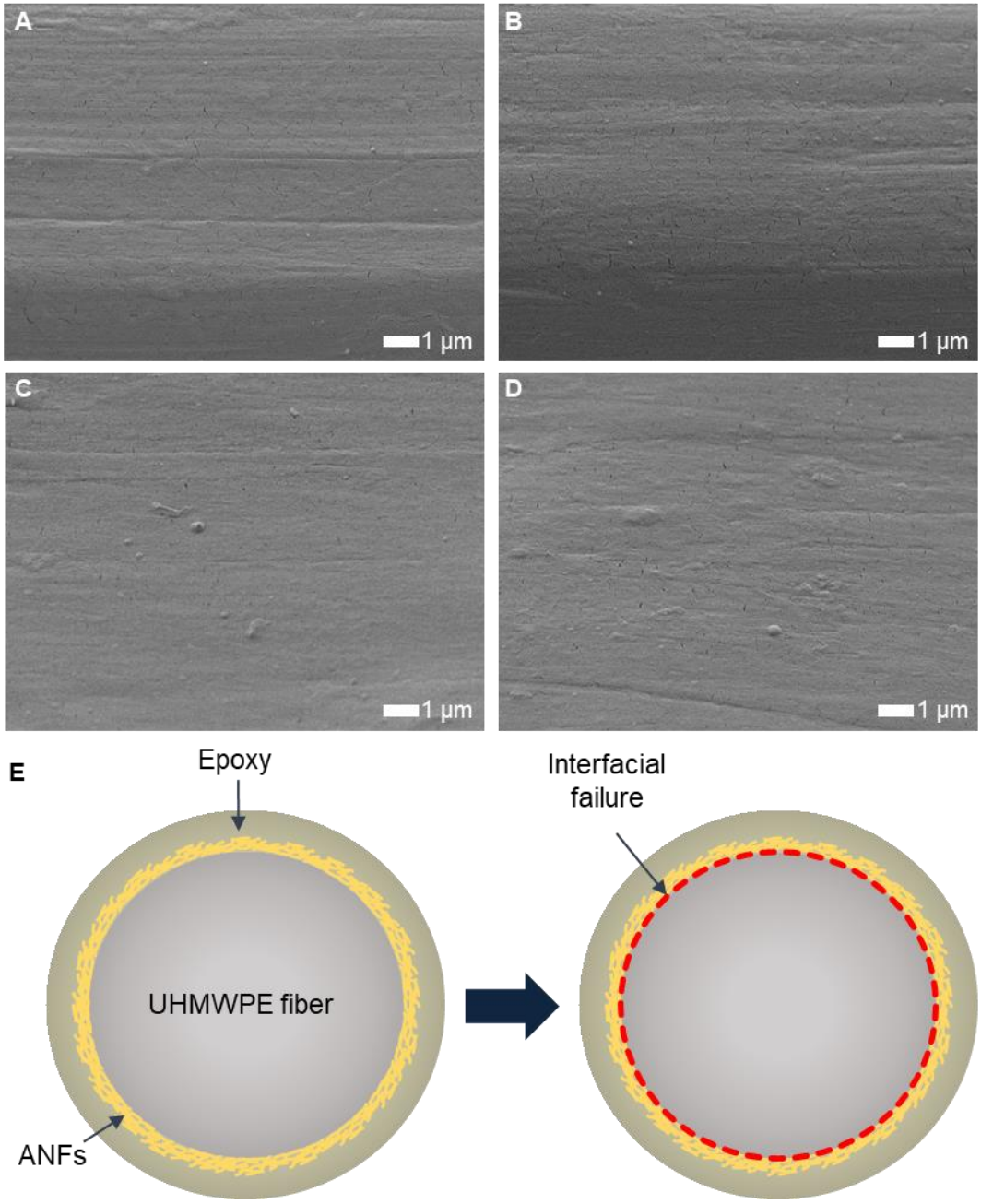

Figure 2.11. SEM images of debonded ANF-coated UHMWPE fiber surfaces after single-fiber pullout testing. (A) 1-min treatment period. (B) 3-min treatment period. (C) 5-min treatment period. (D) 7-min treatment period. (E) Schematic of interfacial failure.

2.6. Chapter Summary

This chapter presents a straightforward and rapid method to introduce ANFs onto the surface of UHMWPE fibers, which improve the fiber's interfacial adhesion to the epoxy matrix.

Uniform and well-adhered ANF coatings were introduced on the surface of plasma-treated fibers using a short dip-coating process. As the dip-coating treatment period increased, the concentration of ANFs on the surface of the fiber also increased providing a nanostructured interphase with greater polar functional groups to improved resin wetting and chemical interaction between the fiber and epoxy matrix. The ANF interphases also yielded greater surface roughness, increasing RMS roughness *Rq* by a minimum of 58% relative to untreated fibers, therefore providing a much-needed mechanical interlocking mechanism between the originally smooth UHMWPE fiber surface and epoxy matrix. The ANF coating was found to increase the interfacial shear strength by more than 100%, irrespective of treatment period, with a maximum improvement of 173% after soaking for 3-min. The process was shown to preserve the tensile strength of the fibers therefore avoiding trade-offs between the interfacial improvement and the in-plane strength of UHMWPE composite materials. This work has shown that an ANF coating has the potential to be integrated into the continuous production of high-performance UHMWPE FRPCs.

Chapter 3. Enhanced Interfacial Shear Strength in Ultra-High Molecular Weight Polyethylene Epoxy Composites Through a Zinc Oxide Nanowire Interphase

3.1. Chapter Introduction

A well-adhered interface is typically desired when fiber-matrix interactions dictate the mechanical properties of fiber-reinforced composites. Ultra-high molecular weight polyethylene (UHMWPE) fibers, however, suffer from poor interfacial properties due to their smooth and inert surface, which has limited their use to ballistic applications. Therefore, enhancing the interfacial properties of such composites will effectively lead to an increased use in structural applications where high modulus, high tenacity, low density, and high impact and abrasion resistance properties are needed. Recent studies have shown that the introduction of nanomaterial reinforcements onto the surface of the fiber can significantly improve the interfacial properties in composite materials, and subsequently their mechanical performance in structural applications.

This chapter investigates an interfacial modification process, which consisted of an oxygen-plasma surface functionalization followed by the grafting of zinc oxide nanowires (ZnO NWs) onto the UHMWPE fiber surface to improve the fiber-matrix interaction in UHMWPE polymer matrix composites. The UHMWPE fiber surface was subjected to varying oxygen-plasma treatment durations to increase the surface oxygen content and improve the adhesion between ZnO NWs and the fiber surface. Post-functionalization, surface chemistry was studied and quantified using both Fourier-transform infrared spectroscopy (FTIR) and X-ray photoelectron spectroscopy (XPS). The ZnO NWs grown on the UHMWPE fiber surface were characterized with scanning electron microscopy (SEM) and the nanowires increased the surface area interaction and

mechanical interlocking abilities between the fiber and matrix. The tensile strength of the UHMWPE fibers was examined using single-fiber tensile tests and was shown to be preserved irrespective of oxygen-plasma treatment durations and ZnO NW growth. Through single-fiber pullout testing, the interfacial shear strength (IFSS) of oxygen-plasma functionalized and ZnO NW-coated UHMWPE fibers was shown to increase. The results detailed in this chapter demonstrate a benign, simple, and effective surface functionalization and nanowire coating to significantly improve the interfacial properties of UHMWPE fiber-reinforced composites.

3.2. Oxygen-Plasma Functionalization and Growth of ZnO NW on UHMWPE Surface

UHMWPE fibers were first cleaned to remove any contaminants through sonication in acetone and then ethanol, followed by drying in an oven at 80°C for 1 hour. The fibers were then functionalized through an oxygen plasma treatment to introduce oxygen functional groups onto the UHMWPE surface. The fibers were treated for varying treatment durations (15 s, 30 s, 60 s and 90 s) in an SPI Plasma Prep II with an oxygen atmosphere of 99.6% purity.

Following the plasma treatment, single UHMWPE fibers were attached to a Teflon frame using 5-min epoxy, with one end of the fiber left unbonded and free (Figure 3.1). The Teflon frame was then dipped in a ZnO nanoparticle (NP) seeding solution [251]. The ZnO NP solution was prepared by first dissolving 0.0125 M of zinc nitrate and 0.02 M of sodium hydroxide separately in ethanol at 50 °C and 60 °C, respectively. Once both solutes were completely dissolved, the zinc nitrate solution was diluted with ethanol to 0.0014 M and the sodium hydroxide solution was diluted with ethanol to 0.0057 M. The zinc nitrate and sodium hydroxide solution were then mixed at a ratio of 18:7 and stirred at 55 °C for 45 min. The Teflon frame with the fibers attached was then dipped into the seeding solution 3 times with annealing at 85°C for 10 minutes in between dipping. After dipping, the fibers were dried for 1 hour at 85°C. The ZnO NWs were then grown

on the UHMWPE fibers using a hydrothermal growth method, where the hydrothermal growth solution consisted of an aqueous solution 2 mM of zinc nitrate hexahydrate, 2 mM of hexamethylenetetramine, and 2 mM of polyethyleneimine. The UHMWPE fibers on the Teflon frame is placed inside a glass beaker that was filled with the ZnO NW hydrothermal growth solution and placed into an oven at 85°C for 5 hours. After the growth, the fibers were rinsed with deionized water and dried at 85°C for 2 hours. The full process schematic is shown in Figure 3.1.

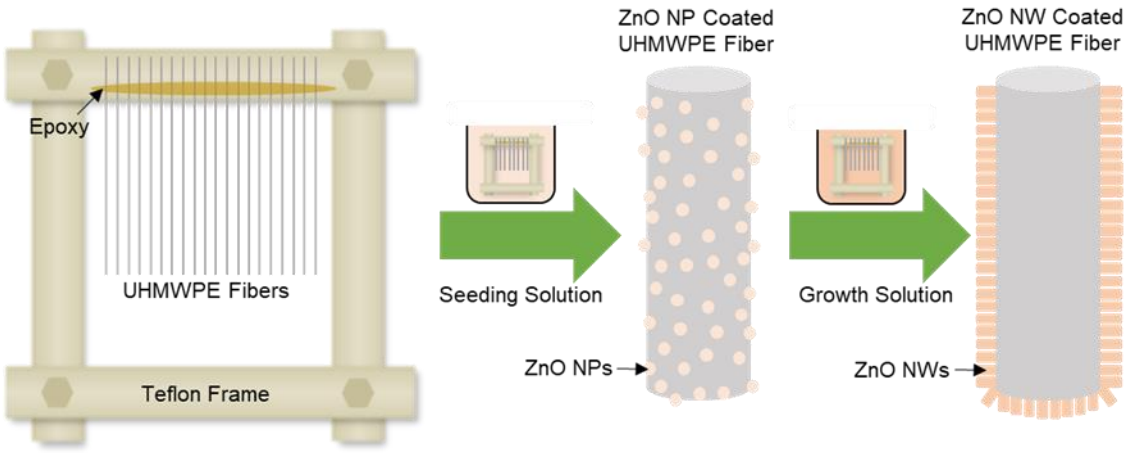

Figure 3.1. Hydrothermal growth method schematic.

3.3. Surface Characterization

To understand the effect the oxygen-plasma treatment had on the UHMWPE chemical structure, fibers with varying treatment durations were investigated via FTIR. XPS was used to further characterize the chemical composition of the UHMWPE fiber surface after oxygen-plasma treatment. The morphology, uniformity, and quality of the ZnO NW growth on the surface of the UHMWPE fiber is imperative to ensure consistent interfacial properties and were characterized using SEM.

3.3.1. FTIR of Functionalized UHMWPE Fiber Surface

The effect of the plasma functionalization treatment on the chemical structure of the UHMWPE fiber surface was investigated through FTIR using a Nicolet iS50 spectrometer with a

SMART diamond iTR attachment. Untreated UHMWPE has distinct absorbance peaks at 2914 cm^{-1}, 2848 cm^{-1}, 1472 cm^{-1}, and 716 cm^{-1} corresponding to C-H stretching. After plasma treatment, the C-H peaks and the new oxygen-containing groups that occur at wavenumbers of 1736 cm^{-1}, 1644 cm^{-1}, 1353 cm^{-1}, and 1113 cm^{-1} remained visible [246] (see Figure 3.2). It is important to note that after the plasma treatment, there were no significant C-H peak shifts, which indicated that the chemical structure of the UHMWPE fiber was not altered by the fiber surface treatment. When comparing fibers that were plasma treated for various durations, the absorbance peaks remained relatively the same which can be attributed to the differences among the varying treatment durations are difficult to observe when compared to the large interaction volume measured during FTIR. Nonetheless, oxygen functional groups have been reported to aid in the adhesion between ZnO NWs and surface of fibers [209]. Therefore, the presence of these oxygen functional groups on the surface of the UHMWPE fiber highlights the potential for enhanced chemical bonding with the ZnO NWs.

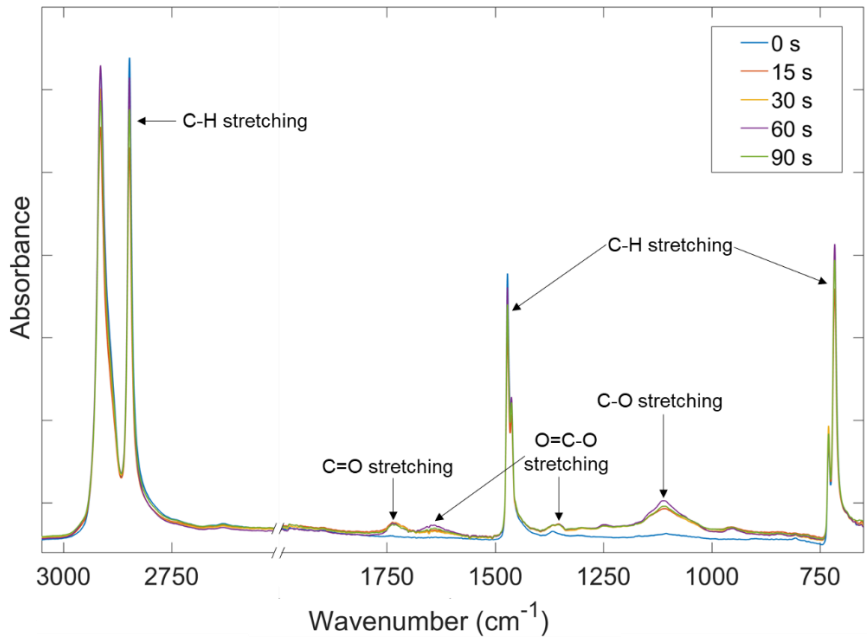

Figure 3.2. FTIR of the UHMWPE fiber surface with varying oxygen-plasma treatment durations with oxygen functional group peaks labeled.

3.3.2. XPS of Functionalized UHWMPE Fiber Surface

To investigate the presence and concentration of oxygen functional groups added to the surface of the UHMWPE fiber after plasma functionalization, XPS was performed using a Kratos Axis Ultra XPS with an X-ray neutralizer that compensated for any charge loss and an Al Kα (1486 eV) monochromatic X-ray source. All binding energy peaks were constrained to a full width-half max of 1.1 eV to 1.7 eV and the curves were fitted using CASA XPS software with a Gaussian 70%-Lorentzian 30% curve mixture. The C1's peaks were fitted at energy bands of 284.5−285.5 eV, 285.5−287.0 eV, 286.5−288.0 eV, and 288.0−290.0 eV, which corresponds to C-C (carbon), C-OH (hydroxyl), C=O (ketone), and COOH (carboxyl) functional groups, respectively [247,248].

The C1's spectrum was obtained from fibers with varying oxygen-plasma treatment durations and Figure 3.3 displays the peak fitting for each oxygen-plasma treatment duration, and the corresponding concentration percentages are shown in Table 3.1. The carbon percentage (C-C%) decreases drastically after a 15 s plasma treatment and introduces ketone and carboxyl functional groups to the UHMWPE fiber surface. When treated with 30 s oxygen-plasma, the ketone and carboxyl functional groups reach their peak concentrations of 12.45% and 8.52%, respectively. When the plasma treatment was increased to a duration greater than 30 s, the concentrations of the ketone and carboxyl functional groups decrease while the hydroxyl group concentration increases.

Initially the weak UHMWPE surface layers are removed, as the highly active ionized O_2 in the oxygen plasma chamber reacts with the UHMWPE surface to introduce oxygen functional groups. When the treatment period is short, the dominant role of the plasma is to introduce active functional groups on the surface of the UHMWPE fiber [252–255]. With a 15 s treatment duration, the C-OH is the dominate active functional group introduced onto the UHMWPE surface. When

the treatment increases to 30 s, more active groups are introduced onto the surface, specifically C=O and COOH. However, when the treatment is prolonged, surface etching occurs, thus removing a portion of the active functional groups introduced onto the UHMWPE surface in the beginning stage of plasma treatment [252–255]. Thus, after a 30 s plasma treatment duration, the recently grafted C=O and COOH bonds are cleaved, causing a reduction in their concentrations and an increase in C-OH concentration. The ketone functional group has been shown to have the highest compatibility with ZnO NWs due to its lack of steric hindrance, which allows for the highly-polar lone pair of electrons on the ketone oxygen atom to be accessible to the zinc ions [209]. The 30 s plasma treated UHMWPE fiber surface had the highest ketone concentration that could potentially provide the strongest adhesion to the ZnO NWs.

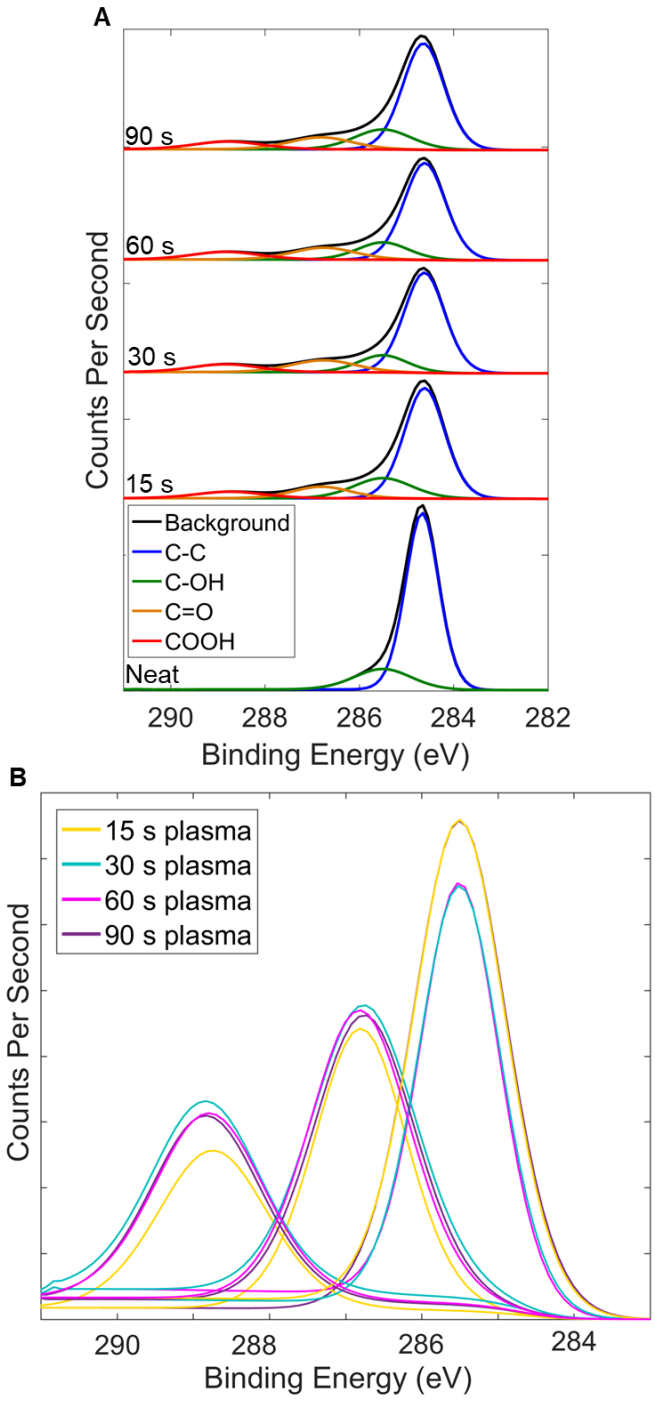

Figure 3.3. (A) Deconvoluted C1's XPS spectrums for varying oxygen-plasma treatment durations of UHMWPE fiber. (B) Comparison of COOH, C=O, and C-OH functional groups for the varying oxygen-plasma treatment durations.

Table 3.1. XPS C1's concentrations of carbon, hydroxyl, ketone, and carboxyl functional groups for varying oxygen-plasma treatment durations of UHMWPE fiber

Plasma-Treatment Durations (s)	C-C% (Carbon)	C-OH% (Hydroxyl)	C=O% (Ketone)	COOH% (Carboxyl)
0	88.40	16.60	0.00	0.00
15	66.24	17.34	9.85	6.57
30	65.54	13.49	12.45	8.52
60	65.09	14.32	12.15	8.44
90	64.80	16.60	10.96	7.64

3.3.3. SEM of ZnO NW Growth on Fiber Surface

The morphology, uniformity, and quality of the ZnO NWs grown on the UHMWPE fibers were then examined through SEM using a JEOL JSM-7800FLV. As shown in Figure 3.4A-B, the surface of untreated UHMWPE is initially smooth, which offers little opportunity for mechanical interactions with the epoxy matrix. With no prior plasma treatment, the ZnO NWs do not adhere well to the inert surface of the UHMWPE, as highlighted by the non-uniform growth on the fiber surface causing poorly adhered ZnO NW sheets to easily fall off (see Figure 3.4C-D). After the oxygen plasma treatment, the UHMWPE fiber surface is found to have an increased population of oxygen functional groups (confirmed by FTIR and XPS), which aid in the adhesion of the ZnO NWs to the surface and allow for a well-adhered uniform growth on the UHMWPE fiber surface (Figure 3.4E-H). The morphology, uniformity and quality of growth of the ZnO NWs grown on the surface of the UHMWPE fiber are observed to be unaffected by the varying oxygen plasma treatment durations. As seen in Figure 3.4E-H, the nanowires for all varying oxygen plasma treatment durations are measured to be approximately 1 μm long with diameters ranging between 40-80 nm and rounded ends, thus demonstrating the uniformity in ZnO NW morphology across

various treatment durations. At least 10 measurements were taken on each UHMWPE fiber with ZnO NWs for the various plasma treatment periods. The nanowires are also well aligned and radiating outward from the fiber surface and have similar growth densities between UHMWPE fibers with varying oxygen plasma durations. Similar characteristic has been observed in prior work where the ZnO NW growth morphology and uniformity was unaffected by surface functionalization [209,214] The modified surface morphology offers a substantial increase in surface area compared to the originally smooth surface and has the potential to improve the IFSS by providing a larger bonding area and introducing mechanical interlocking with the epoxy matrix.

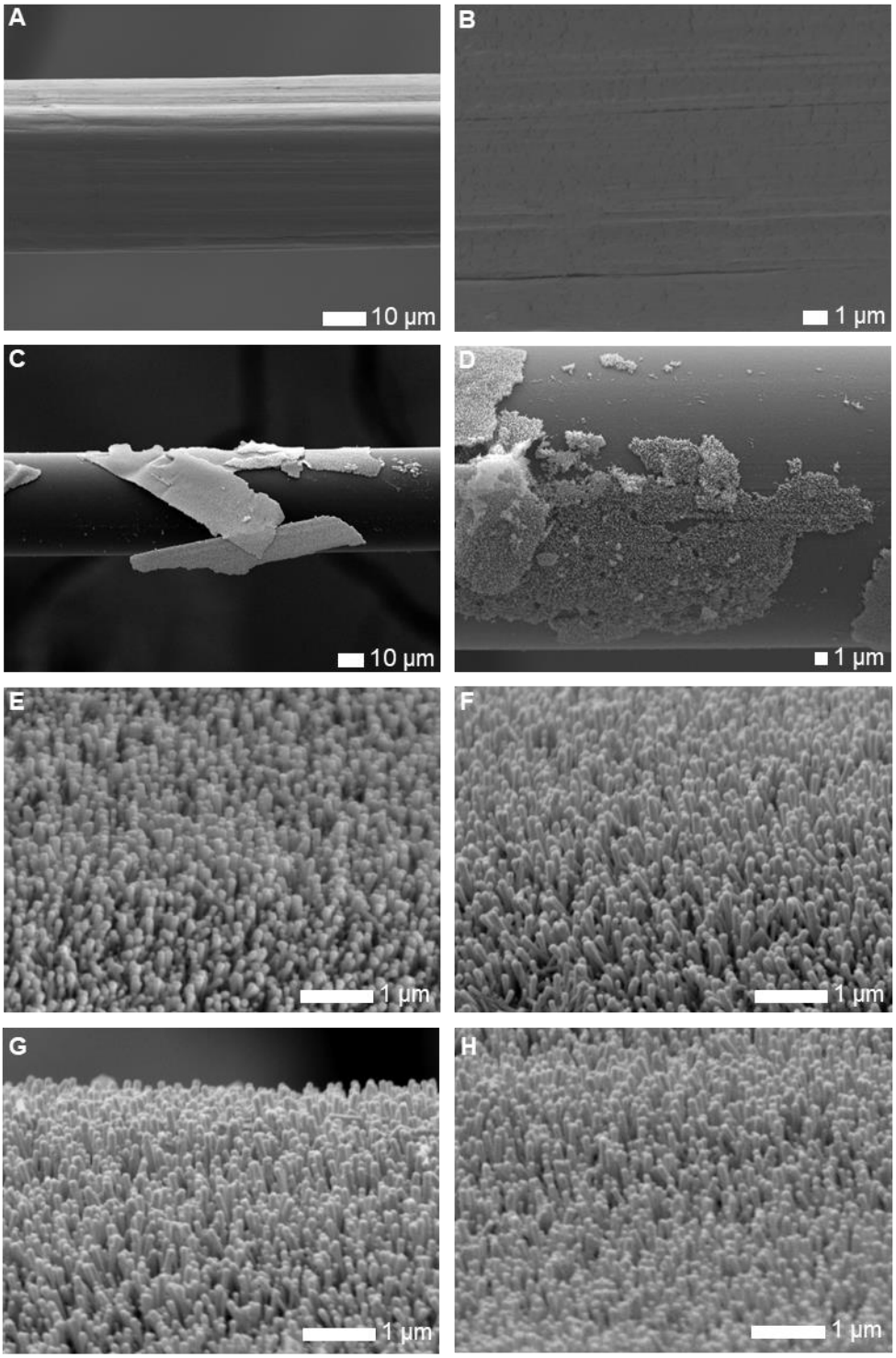

Figure 3.4. SEM images of (A & B) untreated UHMWPE fibers. ZnO NWs grown on plasma treated UHMWPE fibers with oxygen-plasma durations of (C & D) 0 s, (E) 15 s, (F) 30 s, (G) 60 s, and (H) 90 s.

3.4. Mechanical Tests

The fiber mechanical properties were tested using single-fiber tensile tests, which demonstrated property preservation post oxygen-plasma treatment. The IFSS of the ZnO NW-coated UHMWPE fiber with various oxygen-plasma functionalization durations was measured through the use of single-fiber pullout tests. Finally, SEM images of the surface following pullout were taken to analyze the interfacial failure mechanism.

3.4.1. Single-Fiber Tensile Test Measurement

It is important to ensure that the mechanical properties of the UHMWPE fibers remain intact after any surface functionalization. The tensile strength preservation of plasma functionalized and ZnO NW-coated UHMWPE fibers were evaluated using single-fiber tensile tests. A modified testing method was developed to prevent fiber slippage of the smooth inert surface of the untreated UHMWPE fiber. The UHMWPE single fibers were placed between two 38 mm × 13 mm sandpaper tabs at gauge length of 12.7 mm and bonded using a high shear strength epoxy (Loctite® 9430™ Hysol), cured at 82 °C for 1 hour. The samples were then loaded on a 5982 Series Instron load frame and clipped with alligator clips to ensure that no slipping occurred during testing. The samples were tested with a 5 N load cell at a rate of 0.016 mm/s (see Figure 3.5A).

Through single-fiber tensile testing, the tensile strength for oxygen-plasma treated and ZnO NW-coated UHMWPE fibers was observed to be unchanged, regardless of the treatment duration (see Figure 3.5B). These results were expected as the short oxygen-plasma treatment durations allow for functionalization of the surface without damaging the UHMWPE fiber surfaces. In addition, these findings were consistent with other studies in literature demonstrating the benign nature of the plasma treatment to the UHMWPE fiber [46,256–259]. Therefore, an oxygen-plasma

treatment is an efficient method to introduce oxygen functional groups to the surface of the UHMWPE fiber while also preserving the tensile properties Previous work has also shown that the ZnO NW growth is benign when applied to polymer fibers, as it has been reported that the hydrothermal growth method does not affect the tensile properties of the fiber [205–209,211,212]..

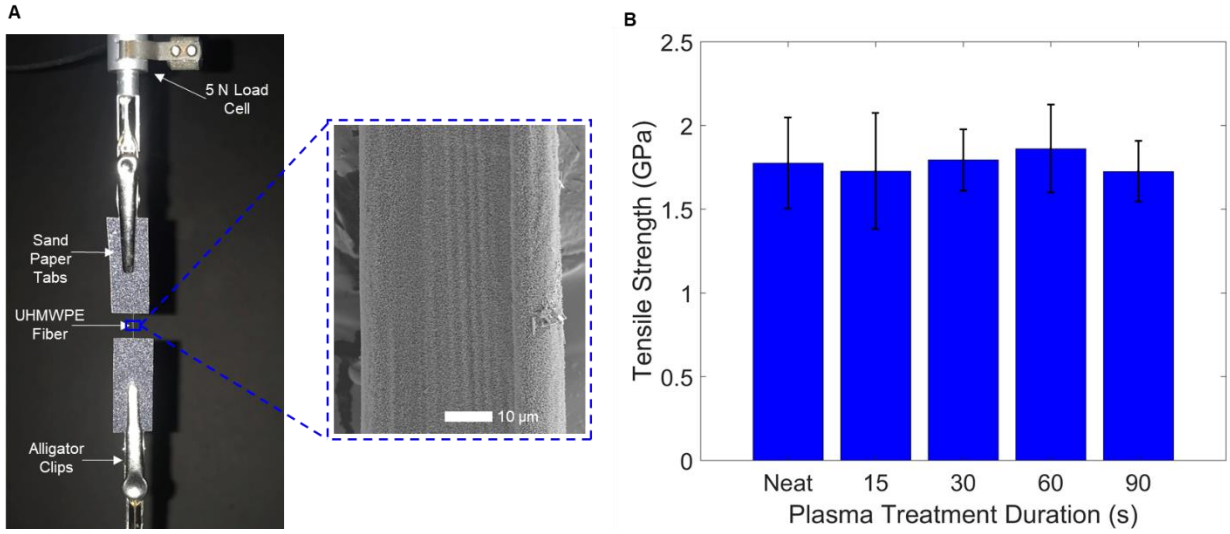

Figure 3.5. (A) UHMWPE single-fiber tensile test setup. (B) Tensile strength of untreated and ZnO NW-coated UHMWPE fiber with varying oxygen-plasma treatment durations.

3.4.2. Single-Fiber Pullout Test Measurements

Single-fiber pullout tests were performed to measure the effect of a ZnO NW interphase and oxygen plasma surface functionalization on the interfacial properties of UHMWPE fiber-reinforced composites. Fiber-matrix debonding is a common failure mode in fiber-reinforced composites, and it can be studied using single fiber pullout tests which allow for direct load measurement during debonding without external interference from the bulk material characteristics [244,245]. The free end of the UHMWPE fibers from the Teflon frame were inserted into a slit in a silicon mold and the embedded length was modified using an optical microscope. Epon 862 resin and Epikure 3230 curing agent, at a ratio 100:35, were added to the silicon mold and cured at 80°C for 8 hours. Once the samples were cured, the epoxy block with

the UHMWPE fiber embedded was removed from the silicon mold, and the same Epon 862 and Epikure 3230 epoxy mixture (ratio 100:35) was used to create tabs on the free end of the fiber (see Figure 3.6A). A large tab, a minimum of 33x larger than the fiber embedded length, was constructed to ensure fiber pullout occurred instead of fiber slippage within the tab (see Figure 3.6A). The single-fiber pullout samples were mounted on a 5982 Series Instron frame, clipped with an alligator clip and tested using a 5 N load cell at a rate of 0.016 mm/s, as shown in Figure 3.6A.

Single-fiber pullout tests were performed for untreated and oxygen plasma treated UHMWPE fibers for durations of 15 s, 30 s, 60 s and 90 s with and without ZnO NWs. Due to the smooth inert surface of the UHMWPE fiber (see Figure 3.4A-B), untreated UHMWPE specimens exhibited a IFSS of 3.13 MPa. When only the plasma treatment was applied to the UHMWPE fiber, the IFSS was found to increase to 4.75 MPa after a 90 s oxygen plasma treatment. This slight increase can be attributed to an increase in the chemical interaction between the UHMWPE fiber and the epoxy matrix due to the addition of oxygen functional groups on the surface of the UHMWPE fiber. Therefore, to increase the IFSS, ZnO NWs were grown on the oxygen plasma treated UHMWPE fiber. When a 30 s oxygen plasma surface treatment was applied in combination with a ZnO NW interphase, the IFSS was found to increase to 7.35 MPa, which corresponds to a 135% improvement, relative to untreated fibers. When the oxygen plasma treatment was further increase to 60 s and 90 s, smaller IFSS improvements of 120% and 108% were observed, respectively, relative to untreated fibers.

The increase in IFSS can be attributed to the mechanical interlocking and increased surface area between the UHMWPE fiber and the epoxy matrix, as the ZnO NWs coated on the fiber are firmly embedded in the epoxy matrix. The ZnO NWs also improve the load transfer during fiber

pullout by reducing the stiffness gradient between the fiber and the matrix. Due to the fact that the morphology, uniformity and quality of the ZnO NW interphase on the UHMWPE fiber are unaffected by the oxygen-plasma treatment, it can be concluded that the IFSS of the specimen is dictated by the adhesion between the ZnO NWs and the UHMWPE fiber surface. Therefore, a comparison between the oxygen functional groups' concentrations and IFSS can provide further inside into the performance of the ZnO NW interphase in UHWMPE composites.

Through experimental and molecular dynamics simulations it has been proven that the ketone functional group has the strongest affinity to the ZnO NWs [209]. This is due to fact that the ketone functional group has lone pair of electrons which are accessible to the zinc ions and are not blocked by protons elsewhere on the molecule. Similar interactions between ZnO NWs and ketone functional groups have also been demonstrated in previous work [205–207,209,212] Therefore, the C=O% obtained using XPS was correlated to the IFSS measurements of ZnO NW coated UHMWPE with various oxygen plasma treatment durations. Figure 3.6C shows that the trend of IFSS is in agreement with the C=O% as a result of the plasma treatment, which confirms that the performance of the ZnO NW interphase is significantly dependent on its adhesion and chemical interaction with the fiber surface. It can be concluded that, to produce the strongest adhesion between ZnO NWs and the UHMWPE fiber surface, the C=O functional group should be maximized on the surface of the fiber.

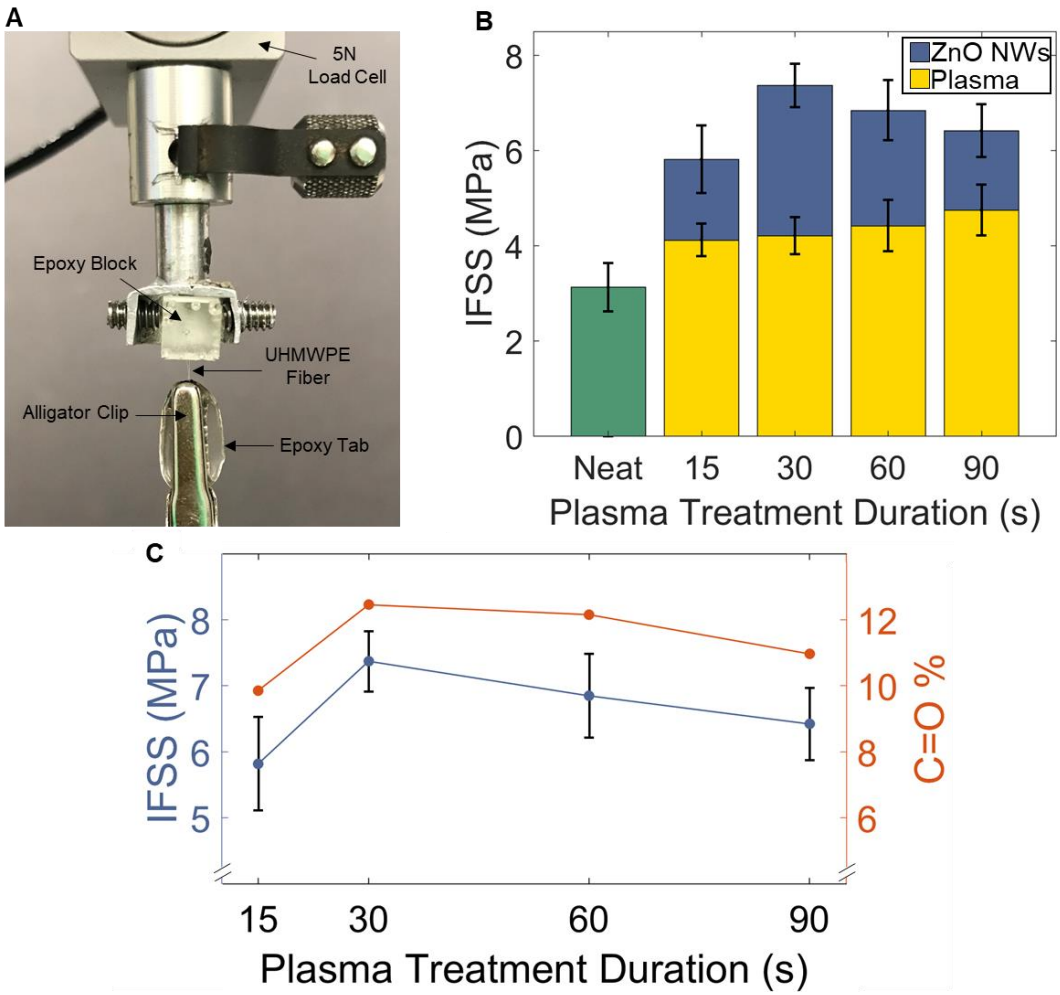

Figure 3.6. (A) Single-fiber test setup and schematic of a single-fiber pullout test specimen. (B) IFSS of UHMWPE fiber with varying oxygen-plasma treatment durations with and without ZnO NWs. (C) Correlation between the IFSS of ZnO NW-coated UHMWPE fibers and C=O% for varying oxygen-plasma treatment durations.

3.4.2.1. Post-pullout SEM failure analysis

To fully understand the reinforcing mechanism of the ZnO NW interphase in UHMWPE composites, SEM images of the fiber surface were taken following pullout. The ZnO NWs act as a hierarchically micro-structured interphase that bridges the discontinuities fiber-matrix interface and introduces a functional gradient that reduced interfacial stress concentrations. This functional gradient reduces shear strain concentrations and transition them away from the weaker fiber-matrix interface and into the tougher, more crack resistant matrix [213]. Furthermore, the nanowire

interphase further increases the distance between the fiber and the matrix, which reduces the overall shear stress experienced by the matrix according to the shear lag theory [260]. Initially, the ZnO NWs are chemically bonded to the UHMWPE fiber surface through oxygen functional groups and then embedded in an epoxy matrix once introduced in a composite, thus introducing a large bonding area between the fiber and the matrix and providing a mechanical interlocking mechanism. During fiber pullout, the sample fails at the weaker interface, which is between the ZnO NWs and the UHMWPE fiber, causing the ZnO NWs to detach from the UHMWPE fiber surface and remain embedded inside the epoxy matrix. This can be confirmed through SEM imaging shown in Figure 7, where all fibers, regardless of oxygen plasma treatment duration, display a ZnO NW-free, clean surface post pullout. This can be attributed to the interaction area between the ZnO NWs and the fiber surface being significantly smaller than that between ZnO NW and epoxy matrix, causing for interfacial failure to occur in the form of ZnO NWs debonding from the fiber surface. This failure mechanism is consistent with previous studies reported in the literature that study the interfacial properties of ZnO NW coated fibers [205–207,209,212].

To improve the IFSS of the UHMWPE composites, further improvements in the bonding strength between the ZnO NWs and the UHMWPE fiber can be explored. For example, different surface functionalization can be developed to enhance the ketone concentration on the surface of the UHMWPE fiber to improve bonding with the ZnO NWs. Additionally, the morphology of the ZnO NWs can be optimized to study the effect of bonding with the fiber and mechanical interlocking between the nanowires and the [208]. For example, larger diameter ZnO NWs would result in an increased surface area interaction between individual nanowires and the UHMWPE fiber which can potentially improve ZnO NW-fiber surface bonding. Additionally, changing the

aspect ratio of the ZnO NWs would provide further study into the interlocking mechanism and ZnO NW-epoxy interface interaction to further optimize the IFSS of UHMWPE composites.

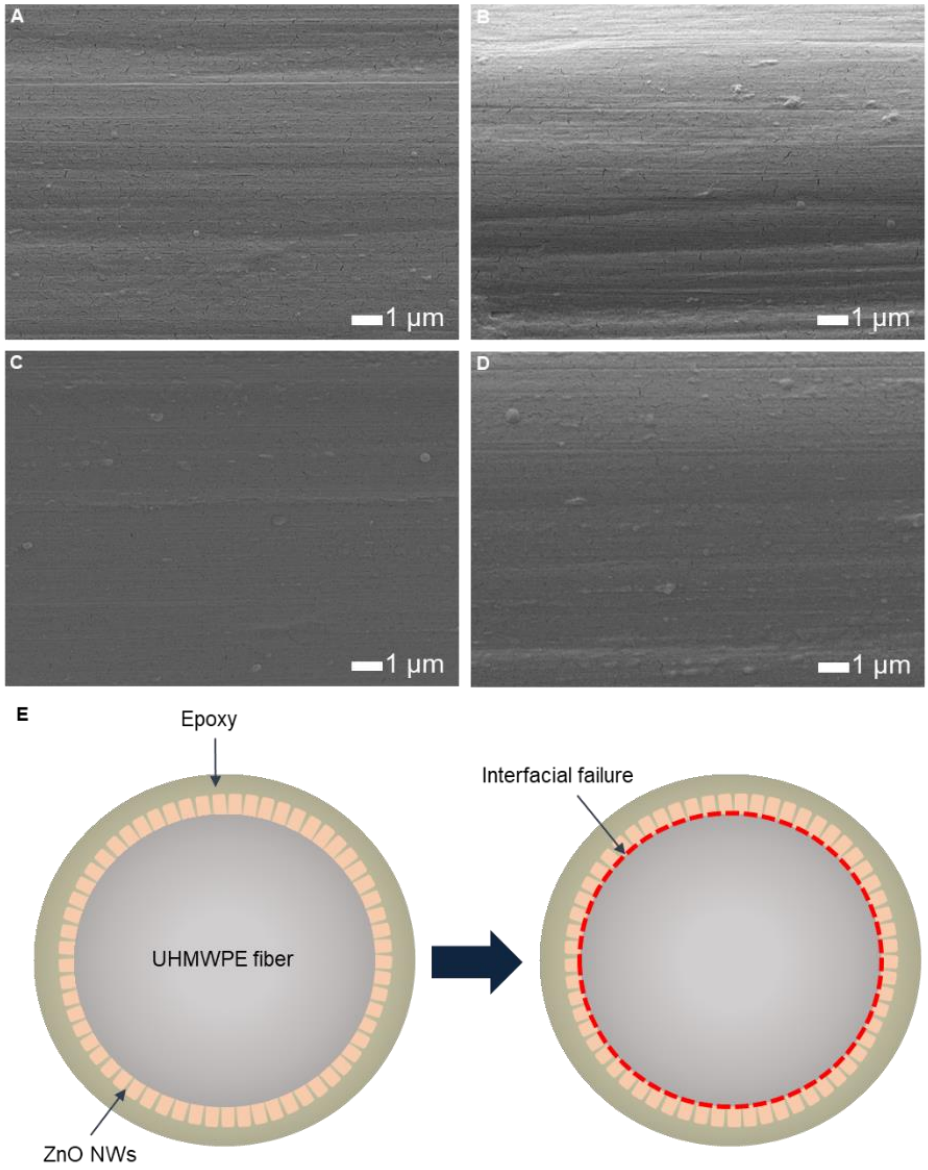

Figure 3.7. SEM images of the UHMWPE fiber surface following single fiber pullout after a (A) 15 s plasma treatment, (B) 30 s plasma treatment, (C) 60 s plasma treatment and (D) 90 s plasma treatment. (E) Schematic of interfacial failure.

3.5. Chapter Summary

This chapter demonstrated an improved IFSS of oxygen-plasma functionalized and ZnO NW-coated UHMWPE fiber-reinforced composites. The ZnO NWs grown on untreated

UHMWPE fibers were shown to have poor adhesion to the fiber; therefore, oxygen-plasma functionalization was applied to the UHMWPE fiber surface to overcome this weak interface. The UHMWPE fibers were oxygen-plasma treated to populate the fiber surface with oxygen functional groups, specifically the ketone functional group, which have been proven to provide enhanced ZnO NW adhesion. XPS showed that the ketone functional group had a maximum concentration of 12.45% after a 30 s plasma treatment duration. Single-fiber tensile tests showed that the tensile strength of the UHMWPE fiber was preserved regardless of oxygen-plasma treatment duration and ZnO NW growth. Through single-fiber pullout testing, the IFSS of UHMWPE composites improved by over 86% for all oxygen-plasma treatment durations with ZnO NWs and exhibited a maximum increase of 135% with a 30 s plasma treatment prior to the ZnO NW growth. This increase in IFSS can be attributed to the enhanced surface area and mechanical interlocking between the ZnO NWs and the matrix. The IFSS results correlated with the XPS data, and the 30 s plasma treatment had the highest ketone functional group concentration, which resulted in the strongest adhesion between the UHMWPE fiber and the ZnO NWs. The process of a simple oxygen-plasma functionalization and grafting of a ZnO NW interphase on the surface of UHMWPE fibers significantly increased the IFSS of UHMWPE fiber-reinforced composites, and therefore, has the potential to be implemented into industrial composite manufacturing and expand the use of UHMWPE fiber-reinforced composites as a whole.

Chapter 4. Improved Inter-Yarn Friction and Ballistic Impact Performance of Zinc Oxide Nanowire Coated UHMWPE

4.1. Chapter Introduction

Ultra-high molecular weight polyethylene (UHMWPE) woven fabrics' properties have spurred an increase in the use of UHMWPE fabric in ballistic protection applications. When subjected to dynamic impact, the primary failure mode of UHMWPE woven fabric is yarn pullout, which results from poor inter-yarn friction between the weft and warp yarns. To overcome yarn pullout, this work investigates the use of zinc oxide nanowires (ZnO NWs), which are grown on plasma functionalized UHMWPE woven fabric, to improve the inter-yarn friction, energy absorption, and impact response of the fabric. The fabric is first oxygen-plasma treated to optimize the adhesion of the ZnO NWs to the UHMWPE surface, and the resulting surface chemistry is examined through X-ray photoelectron spectroscopy (XPS). Then, ZnO NWs are grown on the UHMWPE fabric using a hydrothermal growth method. Once grown, the morphology of the nanowires is characterized using a scanning electron microscope (SEM), and the weight percentage is characterized with thermogravimetric analysis (TGA). Single-fiber tensile tests are performed to ensure the preservation of the tensile strength post oxygen-plasma treatment and ZnO NW growth on the UHMWPE fabric. The inter-yarn friction and pullout energy of the treated UHMWPE fabric is assessed using the yarn pullout method. Due to the direct correlation between inter-yarn friction and ballistic performance, the V_{50} ballistic limit and energy absorption of the oxygen-plasma-treated and ZnO NW-coated UHMWPE fabric are measured through projectile impact testing. The results of this work demonstrate that the application of a simple surface

modification technique to UHMWPE woven fabric is an effective technique to improve inter-yarn friction, impact resistance, and ballistic energy absorption capabilities; thus, further improving the fabric's performance in ballistic applications.

4.2. Growth of ZnO NW on UHMWPE Fabric Surface

4.2.1. Fabric Surface Oxygen-Plasma Functionalization

Plain weave UHMWPE woven fabric (Spectra 1000) with a yarn linear density of 650 denier and weight of 165 g/m^2 was used in this chapter. This type of fabric is commonly used in various soft body armor applications and component parts for military vehicles [261]. The UHMWPE fabric was cleaned by sonication in acetone and ethanol for 10 min each, followed by drying at 90 °C for 60 min to remove any contaminants followed by plasma treatment in an SPI Plasma Prep II with an oxygen atmosphere (99.6% purity) for varying periods of 15 s, 30 s, 60 s, and 90 s.

4.2.2. ZnO Nanoparticle and Nanowire Synthesis on Fabric Surface

A zinc oxide nanoparticle solution was first synthesized as described by Hu et al. [251]. A solution of zinc acetate dihydrate (0.0125 mol) in ethanol and a solution of sodium hydroxide (0.02 mol) in ethanol were heated separately to 60 °C in water baths. Once both solutions were dissolved completely, 32 mL of the zinc acetate solution was diluted in 256 mL of ethanol, while 32 mL of the sodium hydroxide solution was diluted in 80mL of ethanol followed by heating in water baths under stirring to 55 °C. Once both solutions reached 55 °C, the sodium hydroxide solution was added to the zinc acetate solution dropwise and stirred for 45 min at 55 °C. After 45 min, the final solution was quenched in an ice-water bath to prevent further nucleation.

Using the previously synthesized nanoparticles as precursors, vertically aligned ZnO NWs were grown on the surface of the UHMWPE fabric through a hydrothermal approach. The fabric was

first dipped in the colloidal ZnO nanoparticle seeding solution to ensure a uniform coating, followed by annealing at 80 °C for 10 min in a convection oven. Once removed from the oven, the fabric was cooled at room temperature for 10 min. The described seeding process was repeated two more times prior to ZnO NW growth. The ZnO NW growth solution was prepared as described in Malakooti et al. [215]. A solution containing zinc nitrate hexahydrate (67 mmol), hexamethylenetetramine (34 mmol), polyethyleneimine (9 mmol), and sodium hydroxide (48 mmol) was prepared in ultra-pure water (580 mL). After the reagents dissolved, the fabric was immersed in the covered growth solution and remained in solution at 85 °C for 8 hours. After the growth was completed, the fabric was rinsed with ultra-pure water and dried at 80 °C for an hour.

4.3. Surface Characterization

4.3.1. XPS of Functionalized UHMWPE Fabric Surface

The surface chemistry after plasma functionalization was analyzed using Kratos axis ultra XPS with an Al Kα (1486 eV) monochromatic X-ray source and an X-ray neutralizer that compensates for charge loss. The XPS curves were fit using CASA XPS software with Gaussian 70%-Lorentzian 30% curve mixture (GL30). All peaks were constrained to a full width half maximum of 1.1eV-1.7eV and energy bands of 284.5-285.5, 285.5-287.0, 286.5-288.0, and 288.0-290.0 eV were fitted. Each peak corresponds to a different moiety, for C-C (carbon), C-OH (hydroxyl), C=O (ketone), and COOH (carboxyl) bonds, respectively [247,248].

The UHMWPE woven fabric was functionalized using oxygen-plasma with varying treatment periods of 15 s, 30 s, 60 s, and 90 s. The gas molecules in the chamber were ionized by the plasma, which produces highly active species that bombard and react with the UHMWPE surface to remove weak surface layers and introduce a variety of oxygen functional groups on the UHMWPE fabric surface [252,253]. The surface chemistry of the neat and plasma treated

UHMWPE fabric was investigated by XPS. To confirm the presence and measure the types and concentration of oxygen functional groups, the C1s peaks were fitted primarily with C-C (carbon), C-OH (hydroxyl), C=O (ketone), and COOH (carboxyl) at energy bands of 284.5−285.5, 285.5−287.0, 286.5−288.0, and 288.0−290.0 eV, respectively. The peak fittings are shown in Figure 4.1, while the corresponding concentrations of each are detailed in Table 4.1. The C-C (carbon) concentration decreased and the C-OH (hydroxyl) concentration increased with increased oxygen-plasma-treatment periods. The maximum C=O (ketone) concentration was observed after a 30 s oxygen-plasma-treatment period. Due to experimental error, low variability, and the accuracy of the XPS at low percentages, all less than 5%, the COOH (carboxyl) energy band concentrations for the varying oxygen-plasma-treatment periods have not been examined and compared in depth. However, it is important to note that compared to neat UHMWPE fabric, which had a concentration of 0%, the oxygen-plasma treatment induced some carboxylic acid functional groups. Previous research has shown that a higher oxygen surface content results in better adhesion of ZnO NWs to the fiber surfaces [209]. Specifically, the ketone functional group has been reported to have the strongest affinity for zinc ions, due to the high polarity of the lone pair electrons on the oxygen atom of the ketone group not being sterically hindered [209]. Previously reported results suggest that due to an overall increase in surface oxygen content and specifically the ketone functional group, plasma surface treatment has the potential to improve adhesion between ZnO NWs and the surface of UHMWPE fabric.

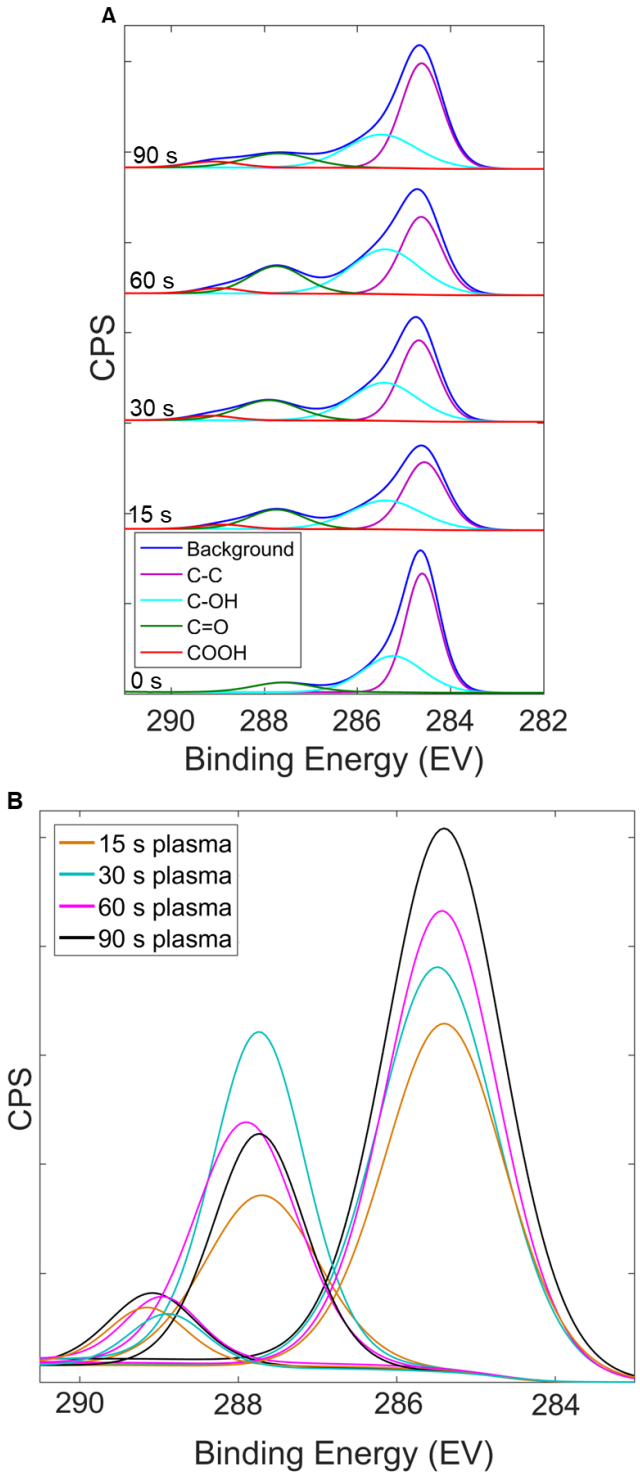

Figure 4.1. (A) C1s deconvoluted XPS spectrums for 0 s, 15 s, 30 s, 60 s, and 90 s oxygen-plasma-treatment periods. (B) Comparison of COOH, C=O, and C-OH functional groups for the varying oxygen-plasma treatment durations.

Table 4.1. Carbon, hydroxyl, ketone, and carboxyl functional groups contents in 0 s, 15 s, 40 s, 60 s, and 90 s oxygen-plasma-treated UHMWPE fabric.

Plasma-Treated Durations (s)	C-C% (Carbon)	C-OH% (Hydroxyl)	C=O% (Ketone)	COOH% (Carboxyl)
0	64.13	25.09	10.78	0.00
15	57.18	28.95	11.11	2.76
30	53.33	29.04	15.46	2.17
60	52.19	29.41	15.45	3.16
90	51.66	30.49	14.30	3.56

4.3.2. SEM of ZnO NW Growth on Fabric Surface

The morphology and uniformity of the ZnO NWs on the fabric were characterized by JEOL JSM-7800FLV field-emission SEM. Energy-Dispersive X-ray Spectrometry (EDS) was taken of the coated fabric to confirm the presence of the ZnO NWs.

The hydrothermal growth of ZnO NWs on the UHMWPE fabric can be initially confirmed through visual inspection, as the color of the fabric changes from glossy off-white to matte-white (see Figure 4.2). The fabric was imaged using SEM to ensure uniform morphology and coating of the ZnO NWs along the surface of the fabric (see Figure 4.3). EDS was performed on the ZnO NW-coated UHMWPE fabric to confirm the growth of the ZnO NWs. As shown in Figure 4.3H, zinc and oxygen were present, thus confirming the growth of ZnO NWs. It should be noted that the gold identified in the EDS spectrum was due to the conductive coating applied to prevent charging during SEM imaging. As shown in Figure 4.3C, the adhesion of the ZnO NWs to the as-received UHMWPE fabric was poor, resulting in the nanowires failing to adhere to the inert UHMWPE surface. To overcome poor adhesion, the oxygen-plasma functionalization was used to alter the surface chemistry of the UHMWPE fabric prior to the ZnO NW growth. Figure 4.3D-G

shows SEM images of 15 s, 30 s, 60 s, and 90 s oxygen-plasma treated UHMWPE fabric with ZnO NWs. These images demonstrate that following the plasma treatment, the ZnO NWs completely and uniformly coated the fabric. The nanowires were well-aligned and displayed uniform lengths ranging between 1–2 μm and diameters ranging between 40–80 nm. The images confirm that the ZnO NW morphology, uniformity, and quality of growth were unaffected by the various oxygen-plasma treatment durations. At least 10 measurements were taken on each UHMWPE fiber with ZnO NWs for the various plasma treatment periods. The addition of the ZnO NWs offered a significant increase in the surface area of the traditionally smooth UHMWPE fabric (see Figure 4.3A-B), which provided a new interlocking mechanism that can increase the inter-yarn friction. However, other factors, such as adhesion between the ZnO NWs and the fabric surface, can also considerably affect the inter-yarn friction.

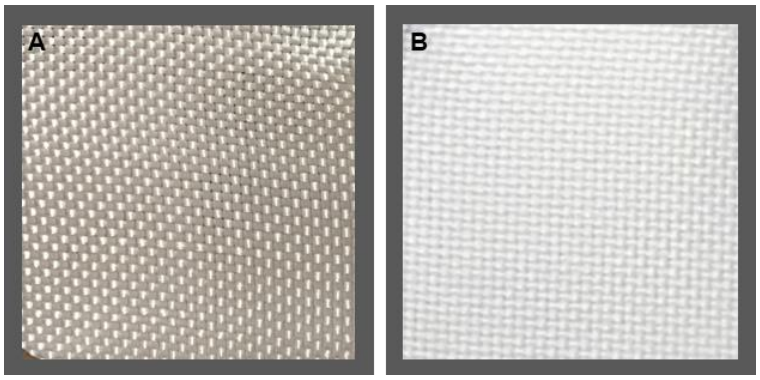

Figure 4.2. (A) Neat UHMWPE fabric. (B) ZnO NWs grown on UHMWPE fabric.

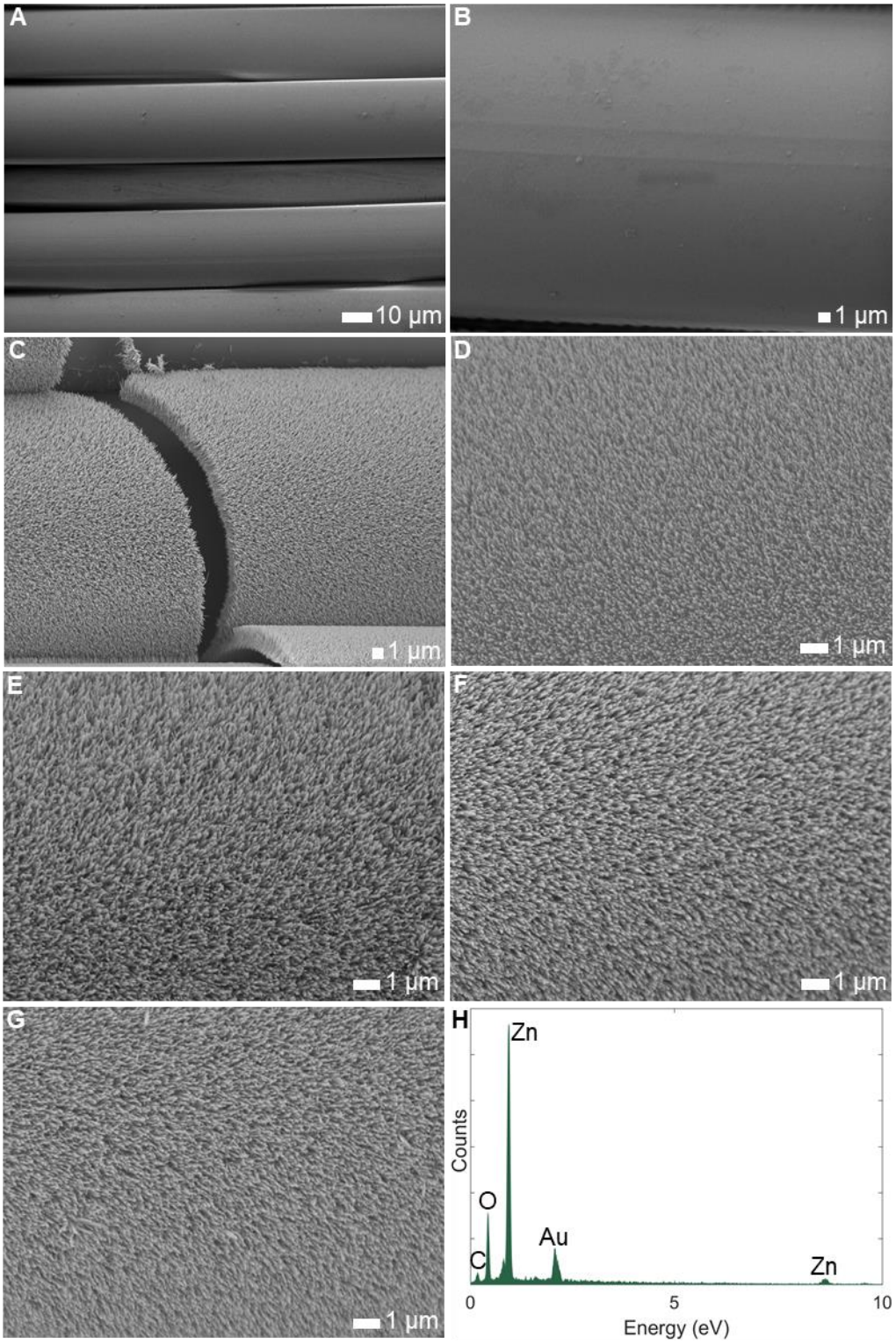

Figure 4.3. (A & B) Neat UHMWPE fabric. (C) 0 s plasma treated UHMWPE fabric with ZnO NWs. Oxygen-plasma-treated UHMWPE fabric with ZnO NWs for (D) 15 s, (E) 30 s, (F) 60 s, and (G) 90 s. (H) EDS of ZnO NW-coated UHMWPE fabric.

4.3.3. TGA of ZnO NW Growth on UHMWPE Fabric Surface

Changes to the composition and overall weight of the UHMWPE fabric due to the introduced ZnO NWs were investigated using TGA. The decomposition temperature of UHMWPE fabric and the weight percentage of the ZnO NWs coated onto the UHMWPE fabric surface were measured by a DSC-TGA on an SDT-Q600, TA Instruments. The samples were tested under nitrogen at a rate of 10 °C/min with a temperature range of 30 °C to 600 °C.

The decomposition and major weight loss in both the neat and ZnO NW-coated UHMWPE samples were observed at a temperature range of 400 °C–500 °C (see Figure 4.4), which is consistent with the thermal decomposition temperature of UHMWPE [262]. Given the ceramic nature of ZnO, it did not decompose in this temperature range. As a result, the contribution of the introduced interphase to the overall increase in UHMWPE fabric's weight could be accurately measured and characterized. Since the hydrothermal growth process can yield slight variations in ZnO NW interphase density throughout the woven fabric, samples with various oxygen-plasma treatment durations of 0 s, 15 s, 30 s, 60 s, and 90 s were tested. The overall increase in the weight of UHMWPE fabric due to the ZnO NWs was found to vary between 5–8% for all specimens and therefore the weight was not found to correlate to the oxygen-plasma-treatment period. While an increase in the weight of ballistic materials is undesirable, especially when used in ballistic protection components such as military vests and shields where overall weight critically affects maneuverability, the ZnO NW interphase is a considerably lighter and more flexible option when compared to other surface modification techniques suggested for ballistic materials, such as nylon coating and STF [37,41].

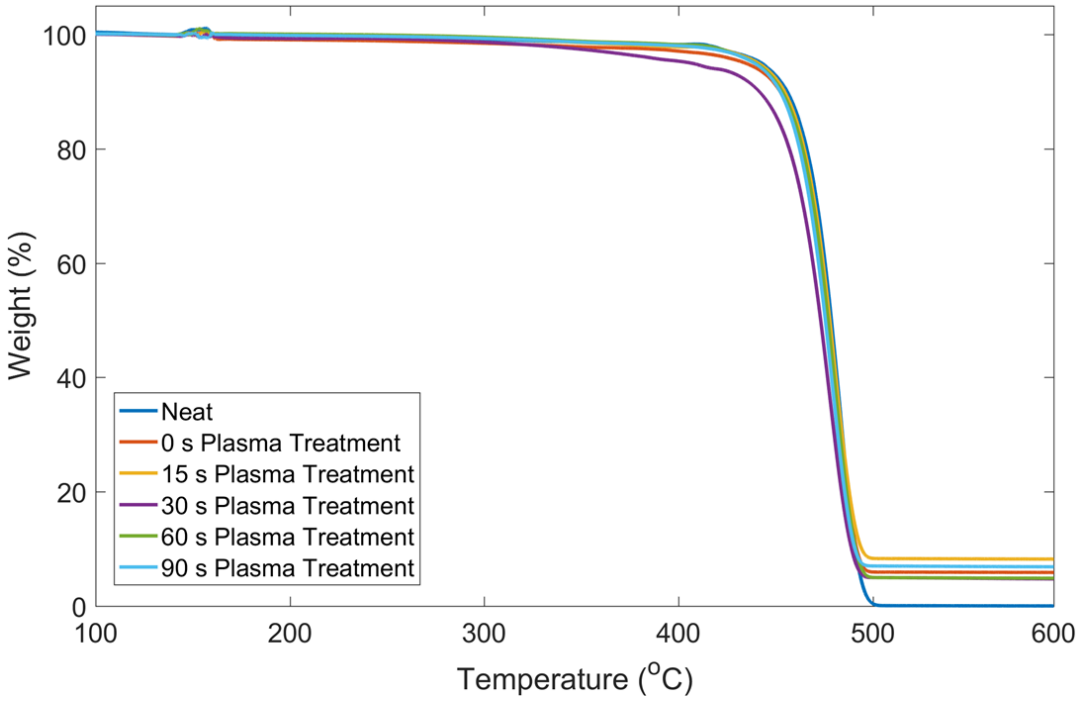

Figure 4.4. TGA curves of neat and ZnO NW-coated UHMWPE fabric with various plasma treatment times of 0 s, 15 s, 30 s, 60 s, and 90 s.

4.4. Tensile Test of Plasma Treated and ZnO NW Coated UHMWPE Fabric

To ensure that the tensile properties of the UHMWPE fibers are maintained post-oxygen-plasma treatment and ZnO NW growth, single-fiber tensile tests were performed on both neat and treated fibers. At least 10 samples were tested for each sample set. The UHMWPE fibers were removed from the fabric of each sample set and positioned between two sandpaper tabs (38 mm × 13 mm) at a gauge length of 12.7 mm and bonded together with high shear strength epoxy (Loctite® 9430™ Hysol), which was cured for 1 hour at 82 °C. The samples were gripped with an alligator clip on a 5982 series Instron load frame and tested at 0.016 mm/s on a 5 N load cell.

Single fibers were removed from the various oxygen-plasma-treated and ZnO NW-grown fabrics for testing. The tensile strength of the UHMWPE fibers was found to be unaffected by either the oxygen-plasma treatment or the ZnO NW growth, which resulted in the treated fibers' tensile strength being maintained in relation to the untreated fibers (see Figure 4.5). This finding

confirmed that the short duration of the oxygen-plasma-treatment periods is capable of sufficiently functionalizing the fiber surface without inducing surface damage, which is consistent with other studies reported in the literature [42,44–51]. The hydrothermal growth of the ZnO NWs was carried out at a significantly lower temperature than the melting point of UHMWPE (145 °C) and was, therefore, a benign approach compatible with UHMWPE fabric. This type of growth method has been previously shown to preserve the tensile strength of various textiles and fabrics [205–211,214–216,263,264].

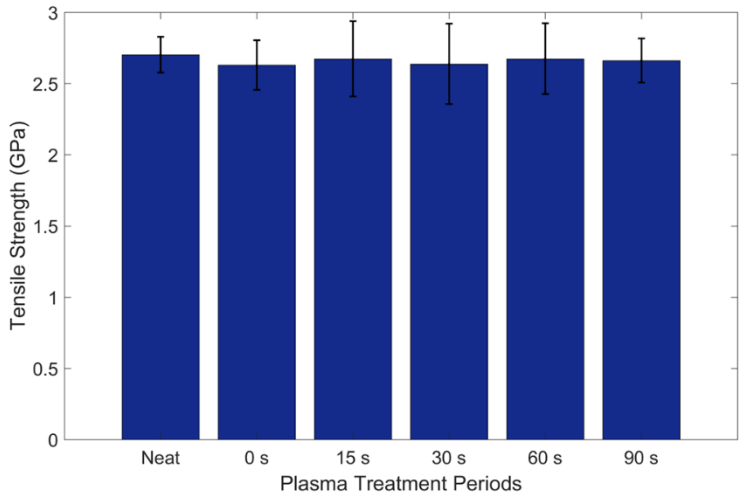

Figure 4.5. Tensile strength of neat and ZnO NW-coated UHMWPE fibers with various oxygen-plasma treatment periods.

4.5. Tow Pullout Test

4.5.1. Tow Pullout Experimental Test Setup

Inter-yarn friction was determined using a yarn pullout method under controlled transverse tension using a custom setup similar to the one described by Hwang et al. and is a commonly used setup for inter-yarn friction measurements (Figure 4.6A) [103,214]. UHMWPE fabric with dimensions of 18 cm × 15 cm was used for the neat and treated samples, where only 17 successive transverse yarns were kept. Ten yarns evenly spaced out along the lateral direction were also kept to be pulled out from the sample. These 10 yarns had an overhang of 114 mm and were separated

by a distance corresponding to 7 removed yarns (see Figure 4.6B). Tabs made of a combination of 5-minute epoxy and duct-tape were added to the free ends of the lateral 10 yarns to allow for an adequate gripping area and to prevent slippage inside the grip during testing. The fabric was clamped into a 90 mm wide custom frame with a fixed column at one end and an adjustable link at the other end. The distance between the two clamping columns was adjusted by a lead screw to keep a constant lateral tension of 100 N. The applied lateral load was measured using a 445 N (100 lb) load cell placed between the lead screw and the other fixed column. The yarns were adequately clamped at the tab and then vertically loaded on a 5982 Instron using a 100 kN load cell and were pulled out with a constant crosshead speed of 50 mm/min. Sample dimensions and the testing setup are shown in Figure 4.6A-B. The recorded load-displacement curves were then mathematically integrated to calculate the amount of energy absorbed, known as pullout energy.

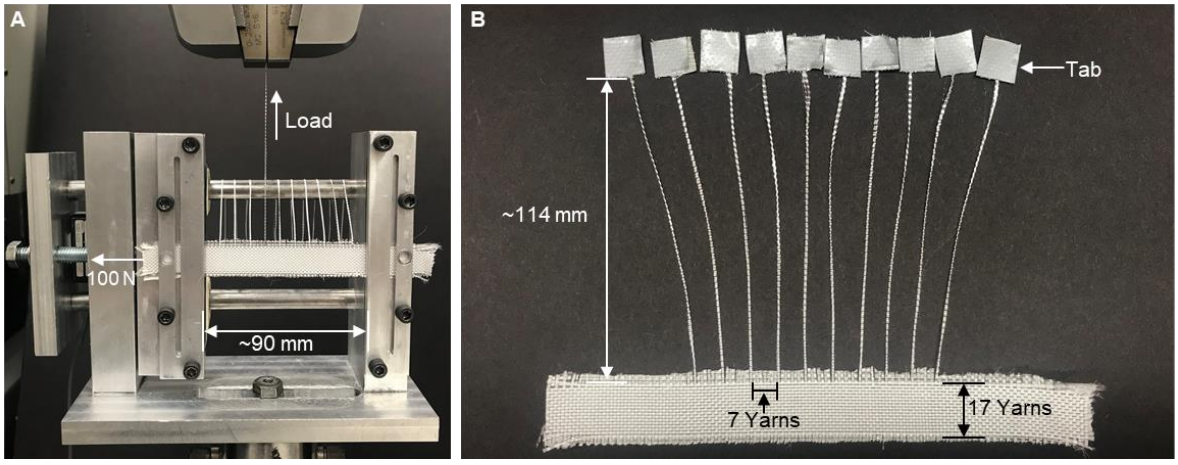

Figure 4.6. (A) Yarn pullout testing setup. (B) Yarn pullout sample and dimensions.

4.5.2. Tow pullout Test Results

Yarn pullout was performed to investigate what effect the ZnO NWs and plasma functionalization has on the inter-yarn friction of UHMWPE woven fabrics. This method allows assessment of the inter-yarn interaction by comparing the maximum load required to pull one yarn from the woven fabric. The pulled yarn exhibits both static friction and kinetic friction during

testing (see Figure 4.7A). Initially, the yarn exhibited static friction until it was completely pulled across the first transverse yarn, resulting in a significant drop in load [26]. As the yarn continued to be pulled from the fabric, it experienced kinetic friction while crossing the remaining 16 transverse yarns [26]. The mean peak load of 10 yarns pulled from the oxygen-plasma treated and ZnO NW-coated UHMWPE fabric with varying oxygen-plasma-treatment periods is shown in Figure 4.7B.

Due to the smooth and inert surface of the UHMWPE fiber (see Figure 4.3A-B), neat UHMWPE fabric experienced a maximum pullout load of 0.93 N. When only the plasma treatment was applied to the UHMWPE fabric, the pullout load was found to increase by 60% after a 90-s oxygen-plasma treatment. This slight increase can be attributed to an increase in the chemical interaction between the UHMWPE yarns due to the addition of oxygen functional groups on the surface of the UHMWPE fiber. Therefore, to increase the pullout load, ZnO NWs were grown on the UHMWPE fiber. A maximum pullout load of 3.01 N was observed in the case of ZnO NW-coated UHMWPE fabric with 0 s plasma treatment, corresponding to a 224% improvement relative to the neat fabric. To quantify the amount of energy expended during pullout, the load vs. displacement curves were numerically integrated, and the averaged pullout energy for each case is shown in Figure 4.7C. The neat UHMWPE fabric displayed a pullout energy of 4.9 mJ, compared to the ZnO NW-coated fabric with 0 s plasma treatment that had a pullout energy of 17.39 mJ and correlated to a 255% increase. For greater understanding of the yarn pullout reinforcement mechanism, the pullout load-displacement curves were investigated (see Figure 4.7A).

When the maximum load is experienced at the first peak, it has been concluded from previous research that mechanical interlocking is the dominant effect for ZnO NW-coated fabric [214,264]. The pullout load-displacement curves presented in Figure 4.7A show that for the ZnO

NW-coated fabric, the load peak is the first initial peak, which indicated that mechanical interlocking of the nanowires is the dominant effect for the increase in pullout force. Additionally, the maximum peak load for the ZnO NW-coated fabric was experienced at a significantly larger (>200%) extension than the neat fabric. This observed delay in the pullout failure of the treated UHMWPE fabric confirmed the increased interlocking mechanism occurrence and interaction between neighboring and intersecting yarns, thus further increasing the resistance to yarn pullout. This yarn pullout behavior is consistent with other research of polymeric fabrics with nano-structured coatings [103,214].

The oxygen-plasma treatment has the potential to improve the adhesion between ZnO NWs and the surface of the UHMWPE fabric. Therefore, varying plasma treatment durations were applied to the surface of the UHMWPE fabric prior to the ZnO NW growth in order to study the effect on inter-yarn friction. UHMWPE fabrics treated for 15 s, 30 s, 60 s, and 90 s showed maximum pullout loads of 3.54 N, 7.09 N, 6.97 N, and 4.68 N, corresponding to a 281%, 662%, 648%, and 403% increase relative to neat fabric (0.93 N), respectively (see Figure 4.7B). It should be noted that the standard deviation in pullout energy of different yarns from the same fabric is relatively small (< 3.4 mJ), thus confirming the absence of any dependencies between the inter-yarn performance of successively pulled yarns. After calculating a one-way ANOVA with $p < 0.01$, there is no statistically significant difference between the 30 s and 60 s plasma-treated periods (p-value = 0.37). When 30 s oxygen-plasma treatment was applied to the UHMWPE fabric prior to ZnO NWs, a maximum pullout energy of 45.22 mJ was observed, which corresponded to an 823% increase relative to the neat fabric. Since the morphology of the ZnO NWs was unaffected by the various oxygen-plasma treatment durations (see Figure 4.3), the improvements in inter-

yarn-friction and pullout energy can be attributed to the improved adhesion between the ZnO NWs and the UHMWPE fabric post-oxygen-plasma treatment.

When inspecting the load vs. displacement curves of the oxygen-plasma-treated specimens (see Figure 4.7A), the maximum peak was the initial peak. This corresponds to mechanical interlocking between the ZnO NWs of neighboring yarns as the primary contributor to the improved yarn pullout performance. For all cases, a delay in pullout failure was observed relative to the neat UHMWPE fabric. This increase in extension before sliding demonstrated the improved resistance due to the increased interlocking mechanism between yarns as a result of the ZnO NW interface. The larger extension at maximum load led to a greater pullout energy in the 30 s plasma-treated sample compared to the 60 s plasma treated sample, even though they had insignificant differences in maximum pullout load.

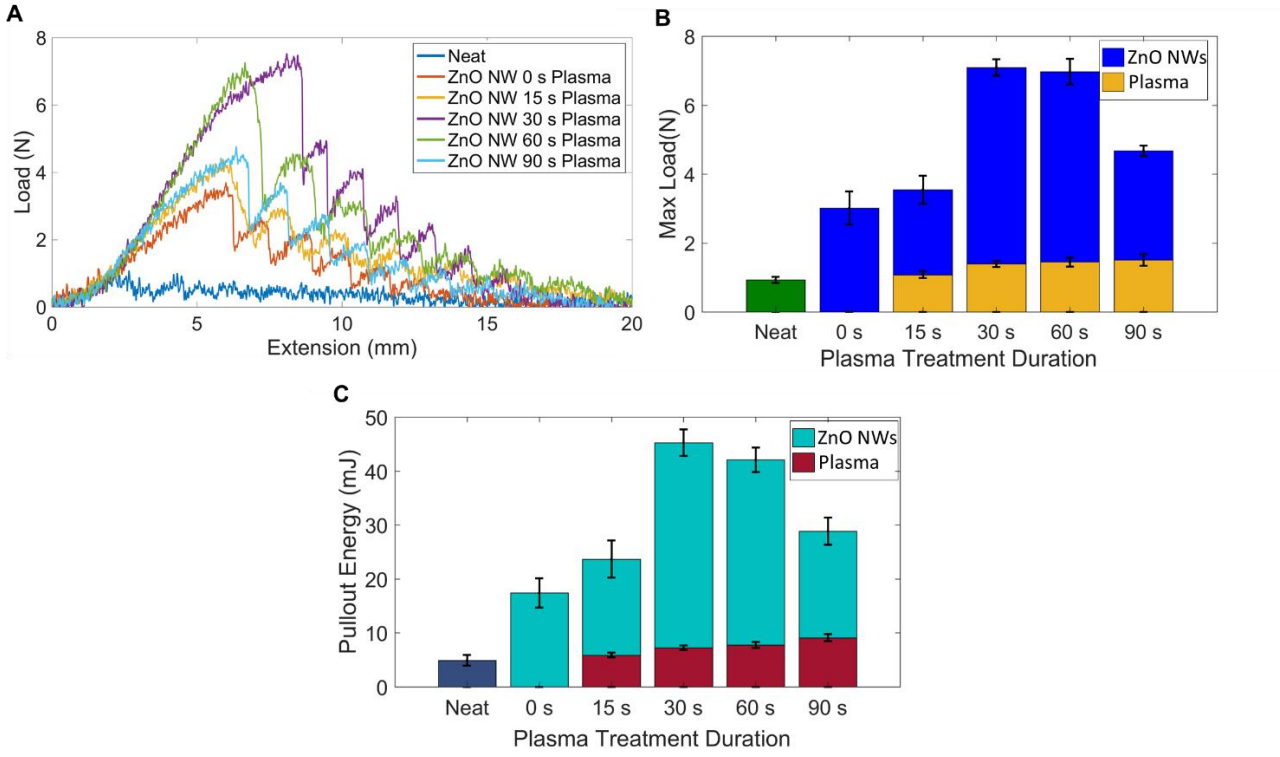

Figure 4.7. Yarn pullout for neat and ZnO NW-coated UHMWPE with varying oxygen-plasma treatment durations. (A) Representative load vs. extension plots. (B) Average peak loads. (C) Average pullout energies.

To further understand the effect oxygen-plasma treatment had on the adhesion between ZnO NWs and UHMWPE fabric, a comparison between the surface XPS analysis and the yarn pullout data was conducted (see Figure 4.8). Since the ZnO NW morphology and uniformity were unaffected by the oxygen-plasma-treatment periods, the mechanical interlocking mechanism between neighboring yarns within the fabric was the same during yarn-pullout. However, the surface concentration of the ketone functional group was found to follow the same trend as that of the UHMWPE yarn pullout load (15 s < 90 s < 60 s = 30 s), which confirmed that adhesion between the ZnO NWs and the fabric surface is primarily dependent on surface chemistry. As shown in Table 4.1, 30 s and 60 s plasma-treated samples had the two highest ketone concentrations, which also corresponded to the highest pullout load and energy. This trend can be expected since previous work has shown that the ketone functional group improves the adhesion between ZnO NWs and the treated surface [209]. The adhesion of ZnO NWs to the surface of the UHMWPE fabric, which is primarily dependent on ketone surface concentrations [209], is critical to the inter-yarn reinforcing performance in UHMWPE woven fabrics.

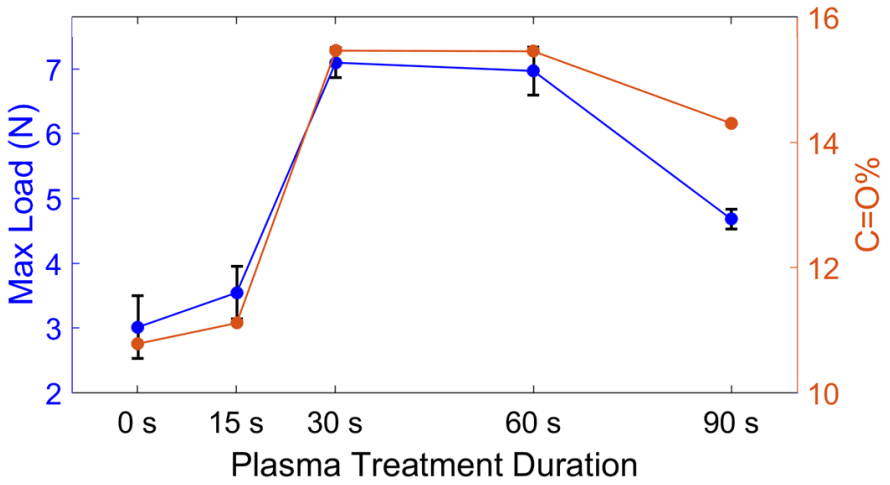

Figure 4.8. Correlation between the pullout load of ZnO NW-coated UHMWPE fabric and C=O% for varying oxygen-plasma treatment durations.

4.6. Ballistic Impact Test

4.6.1. Ballistic Impact Experimental Test Setup

A customized gas gun setup was used to measure the impact load and ballistic limit of neat and ZnO NW-coated UHMWPE fabric samples, where details of the setup can be found at Stenzler et al. [265] and a schematic is shown in Figure 4.9. The UHMWPE fabric was clamped in a custom loading plate, as shown in Figure 4.10A, to ensure no slipping of the fabric occurs during impact, and then the plate was screwed to the gas gun clay trap box (see Figure 4.10B). A 29 g, 4130 alloy steel projectile with an 11.4 mm diameter hemispherical face instrumented with a load cell and an accelerometer (Kistler K-Shear® 8742A50) provided load measurements during impact (see Figure 4.10C). The muzzle was placed 6.35 mm away from the sample and was pressurized with argon to a predetermined level to produce a desired velocity. Two photoresistors at the end of the barrel were used to calculate the velocity of the projectile immediately prior to impact. The V_{50} ballistic limit was obtained by testing a minimum of 12 samples, where the outcome produced at least 5 samples where the projectile penetrated the fabric, and 5 samples where the projectile did not penetrate the fabric. Once all samples were tested, the average of the 3 highest velocities where the projectile did not penetrate the fabric and the 3 lowest velocities where the projectile did penetrate the fabric were used to calculate the V_{50} ballistic limit of the fabric.

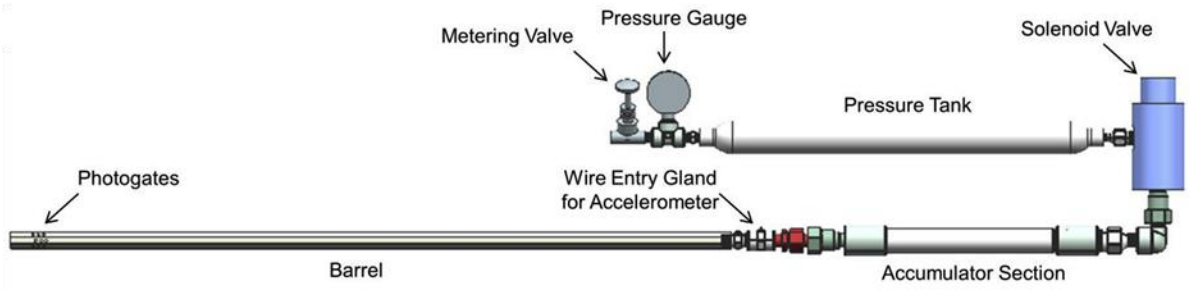

Figure 4.9. Schematic of the gas gun impact testing setup.

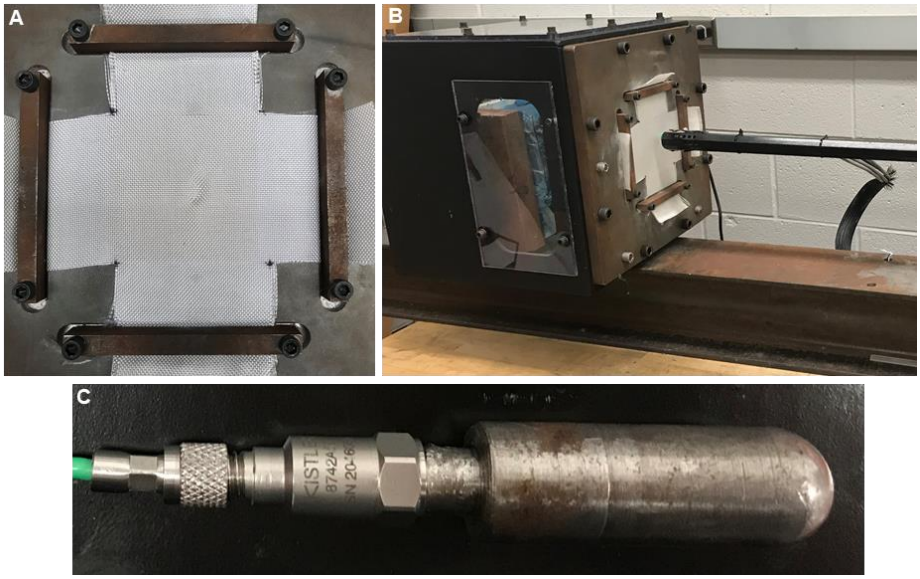

Figure 4.10. (A) Fabric clamping. (B) Ballistic setup. (C) Projectile with mounted load cell and shock accelerometer.

4.6.2. Ballistic Impact Test Results

Correlation between the inter-yarn friction and improved energy absorption with impact resistance has been extensively reported [5,23–30], and therefore, the observed improvement in the inter-yarn interaction of plasma treated and ZnO NW-coated UHMWPE fabric should yield an enhanced impact performance. In addition, the V_{50} ballistic limit of the modified fabric is assessed through ballistic impact tests. Substantial improvements in the pullout load and energy of woven fabrics are needed in order to observe any significant enhancements to their ballistic limit and impact energy [37,53,91,98,100,102,103,214,216,266]. For example, yarn pullout is one of many contributing factors to the failure of woven fabrics under ballistic impact, in addition to other failure modes such as fiber rupture. Therefore, it is typically necessary to achieve a significantly large increase in inter-yarn friction when aiming to sufficiently improve ballistic limit and energy in order to justify the integration of such surface modification techniques in the fabrication of woven fabrics for commercial/military. Since 30 s plasma and 60 s plasma treatments yielded

identical maximum yarn pullout load improvement, yet the 30 s plasma treatment resulted in a slightly higher pullout energy, the UHMWPE woven fabric was plasma treated for only 30 s prior to ZnO NW growth. To analyze the effect the ZnO NWs have on the impact performance of woven UHMWPE fabric, the V_{50} and impact load of one ply of neat fabric were compared to one treated ply.

The V_{50} ballistic limit is defined as the average value of the three highest velocities where the bullet did not penetrate and the three lowest velocities where it did penetrate through the fabric. To be considered penetrated, the bullet and sabot must pass completely through the fabric. According to the results shown in Table 4.2, relative to neat fabric, the V_{50} of the ZnO NW-coated UHMWPE fabric increased by 59%, from 23 m s^{-1} to 36.6 m s^{-1}, respectively. Similarly, the mean impact load increased by 227%, from 388 N to 1271 N, respectively. It should be noted that the load measurement was not collected for the treated sample impacted at 37.30 m s^{-1}, thus the average mean impact load was taken from the remaining 11 samples. The increase in the V_{50} resulted from the interlocking mechanism and increased surface area interactions between neighboring yarns with ZnO NWs, which limited the mobility of the individual fibers and yarns.

The increased friction between the yarns delayed their movement, which allowed the fabric to stop the projectile delivered from higher velocities, improving its impact resistance. During the impact of the projectile, multiple modes of failure such as yarn pullout, yarn rupture, fabric bowing, or a combination of them can occur. In all the neat samples where the projectile penetrated the fabric, the failure mode was primarily due to yarn slippage and pullout at the location where the projectile impacted the fabric, which can be attributed to the low inter-yarn friction between neat UHMWPE yarns (see Figure 4.11B). However, in the ZnO NW-coated fabrics, where higher velocity projectile penetration occurred, failure was dominated by fiber breakage instead of yarn

pullout, which resulted in considerably smaller yarn slippage (see Figure 4.11D). This can be attributed to the reduced ability of yarns to slide against each other due to the increased inter-yarn friction.

As mentioned earlier, ballistic impact performance can be correlated to the increased inter-yarn friction, as confirmed here. Due to the many factors in ballistic failure, the 662% improvement in inter-yarn friction translates to a 59% increase in the fabric's V_{50}. Similarly, the 822% improvement in pullout energy translates to a 227% improvement in maximum impact load. The discrepancy between the improvement in inter-yarn friction and ballistic performance of the UHMWPE woven fabric was due to the fact that multiple failure modes occur during ballistic impact, such as fiber rupture, that were not considered in yarn pullout. It should be noted that the observed considerable improvements in the ballistic performance (227% increase in impact load) of the UHMWPE woven fabric clearly outweigh the slight increase (5-8%) in the overall weight of the fabric (see Figure 4.4), thus highlighting the advantage of the ZnO NW interphase and justifying its introduction into such ballistic materials. Overall, the use of an oxygen-plasma functionalization with a ZnO NW interphase design method is capable of increasing the impact resistance of UHMWPE fabric through improving its inter-yarn properties, and providing an overall improved ballistic performance.

Table 4.2. Speeds, penetration status, load, and corresponding V_{50} for neat and plasma functionalized, ZnO NW-coated UHMWPE fabric.

Neat UHMWPE Fabric			**ZnO NW-Coated UHMWPE Fabric**		
Impact Speed ($m\ s^{-1}$)	**Penetration**	**Maximum Load (N)**	**Impact Speed ($m\ s^{-1}$)**	**Penetration**	**Maximum Load (N)**
8.02	No	242	29.53	No	1090
14.65	No	459	30.19	No	1060
16.56	No	72	32.67	No	1150
19.53	No	418	34.90	No	1103
21.17	No	216	35.48	No	1079
23.09	Yes	478	35.74	No	1270
23.96	No	554	36.22	No	975
24.00	Yes	211	36.77	Yes	1100
26.27	Yes	445	37.30	Yes	
28.01	Yes	502	38.10	Yes	2940
32.45	Yes	514	40.53	Yes	1150
33.87	Yes	548	45.35	Yes	1060
V_{50} = 23 $m\ s^{-1}$			**V_{50} = 36.6 $m\ s^{-1}$**		

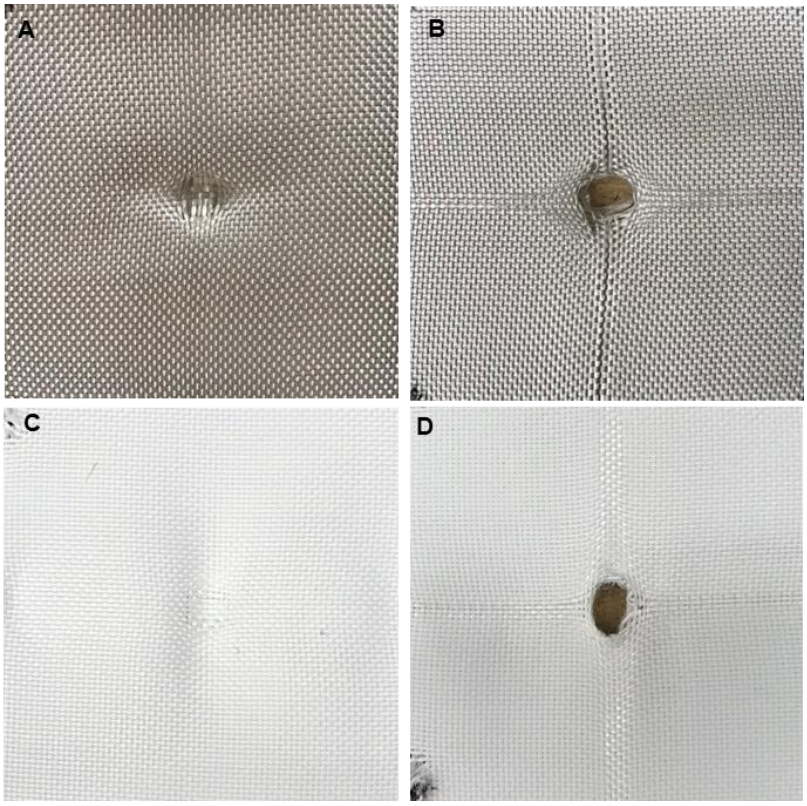

Figure 4.11. Comparison between neat UHMWPE fabrics and treated UHMWPE fabrics after impact. (A) Neat sample that did not penetrate at velocity of 19.53 m s-1. (B) Neat sample that penetrated at velocity of 26.27 m s-1. (C) Treated sample that did not penetrate at velocity of 35.48 m s^{-1}. (D) Treated sample that penetrated at velocity of 37.30 m s^{-1}.

4.7. Chapter Summary

In summary, this chapter demonstrates improved inter-yarn friction, energy absorption, and impact response of plasma treated and ZnO NW-coated UHMWPE woven fabric. The inert UHMWPE fabric surface was oxygen-plasma treated to populate the surface with oxygen functional groups, specifically ketone functional groups, which allows for enhanced ZnO NW adhesion. Vertically aligned ZnO NWs were grown using a benign hydrothermal process that preserves the fiber tensile strength. The ZnO NW-coated UHMWPE fabric exhibited a 224% and 255% increase in maximum pullout load and pullout energy, respectively, relative to neat fabrics. When applying a 30 s plasma treatment to the UHMWPE fabric prior to ZnO NW growth, inter-yarn properties can be further improved, yielding an overall 662% and 822.9% improvement in

maximum pullout load and pullout energy, respectively. The improved inter-yarn performance can be attributed to mechanical interlocking and increased surface area provided by the ZnO NWs between neighboring yarns. Moreover, 30 s plasma treated and ZnO NW-coated UHMWPE fabrics displayed an improved ballistic performance with a 59% and 227% improvement relative to neat fabric in V_{50} ballistic limit and absorbed impact load, respectively. These improvements can be attributed to the increased inter-yarn friction between yarns, which limits yarn movement during impact and improves resistance to penetration of the projectile. The results presented here show that an oxygen-plasma functionalization with a ZnO NW interphase is capable of significantly increasing the inter-yarn friction and impact response of traditional UHMWPE woven fabric, presenting a promising method that can be integrated in UHMWPE based equipment for ballistic applications.

Chapter 5. Laser-Induced Graphene for In-Situ Ballistic Impact Damage and Delamination Detection in Aramid Fiber-Reinforced Composites

5.1. Chapter Introduction

Aramid fibers have been shown to exhibit impressive mechanical properties, including high strength-to-weight ratio, excellent abrasion resistance, and exceptional ballistic performance. For these reasons, aramid fiber-reinforced polymer composites (FRPCs) have been widely used in high impact loading environments where ballistic properties are vital. In-situ damage monitoring of aramid composites under dynamic loading conditions typically requires externally-bonded sensors, which add bulk and are limited by size and space constraints. To overcome these limitations, this chapter examined a piezoresistive laser-induced graphene (LIG) interface for embedded impact sensing in aramid fiber-reinforced composites. The work presented here investigates the potential of LIG for in-situ impact damage and delamination detection in aramid fiber-reinforced polymer composites. To accomplish this, LIG was directly formed on the aramid fabric using a laser printer, before infusing the treated fabric to form aramid laminates. The ability of LIG to sense ballistic damage was evaluated by impacting the treated aramid laminates using a gas gun, and the electrical resistance was simultaneously monitored using the four-point probe technique. Through the monitoring of electrical resistance during ballistic impact, information regarding time and severity of the impact was obtained. The impact velocity correlated with the resistance change of the composites due to delamination between aramid plies and damage to the LIG interface. Additionally, resistance measurements taken during Mode I interlaminar fracture tests were used to investigate the correlation between the change in resistance and delamination

between composite plies. The interlaminar fracture toughness and areal-density-specific V_{50} of the LIG-treated aramid composites increased relative to untreated aramid composites. This work demonstrates a methodology to form multifunctional aramid-based composites with an LIG interface that provides both improved toughness and imbedded sensing of impact and damage severity during ballistic impact.

5.2. LIG Process and Characterization on Aramid Fabric

LIG was generated on the surface of the aramid fabric using the method described by Nasser et al. [227]. Prior to the laser treatment, the aramid fabric (Kevlar® KM2+ fabric plain-weave, style 790, scoured CS-800, received from BGF Industries) was successively sonicated in acetone and ethanol for 10 min to remove organic surface contaminants, and then dried in a vacuum oven at 100 °C for 1 hour. The carbonization of only one side of the aramid fabric was performed using a 40 W CO_2 laser printer (Epilog Zing 16) operated in raster mode, at a speed of 1 $cm^2\ s^{-1}$, pulsing density of 400 dots per inch (DPI), and output power of 20% (see Figure 5.2A). The parameters used in this work have previously been found to maintain the specific strength of the fabric [227]. Following the laser treatment, the morphology of the LIG-treated aramid fabric surface was characterized using a JEOL JSM-7800FLV field-emission scanning electron microscope (SEM).

To integrate a piezoresistive sensing element within traditionally insulating aramid fiber composites, one surface of each aramid fabric ply was coated with conductive LIG. Notably, no pre- or post-treatment of the aramid fibers was required prior to the conversion of the surface fibers to LIG. Following the laser treatment, the surface morphology of the LIG-coated aramid fabric was investigated using SEM imaging. As shown in Figure 5.1B, the exposed surface fibers of the woven aramid fabric are drastically changed following the laser treatment relative to an untreated

aramid fiber (see Figure 5.1A). Rather than displaying the smooth surface of untreated aramid fibers, the surface of the laser treated fibers possess a three-dimensional (3D) microporous fibrous structure. Previous studies have investigated the effect of the laser output power, pulsing density, and focusing density on the resultant LIG microstructure on the aramid surface and the corresponding mechanical properties [221,227]. In this work, a pulse density of 400 DPI, defocusing distance of 0.3 mm, and output power of 20% were chosen to generate a uniform coating on the surface of the exposed aramid fibers [227]. According to Figure 5.1C, the thickness of the aramid fabric was ~400 μm and the LIG layer was measured to be ~25 μm, which is equivalent to the diameters of 2 individual aramid fibers. It should be noted that the laser-induction parameters used in this dissertation resulted in the complete conversion of the top aramid surface to a textured graphitic layer while simultaneously limiting the laser penetration depth, thus leaving the majority of the aramid fibers intact and preserving the specific strength of the fabric as shown in Figure 5.1C [227].

The converted amorphous carbon atoms created a continuous conductive top surface; however, the untreated portion of the fabric remained insulating through its thickness, which confirmed that the LIG remained on the surface and did not completely penetrate the fabric (Figure 5.1). The fibrous structure of the LIG coating has previously been shown to result in improved mechanical interlocking and increased surface area interaction between the reinforcing fibers and the matrix, therefore, strengthening the interlaminar region in the aramid laminate [227,267]. The porous nature of LIG also permitted for easy infusion and resin wetting during the composite fabrication process. Furthermore, a small portion of the LIG remained exposed at the surface of the laminate, which allowed for direct contact between the LIG and the measurement probes

without the need to remove any of the matrix at the surface. The final resistance values of the ballistic composites ranged between ~40 – 100 Ω measured using the four-point probe method.

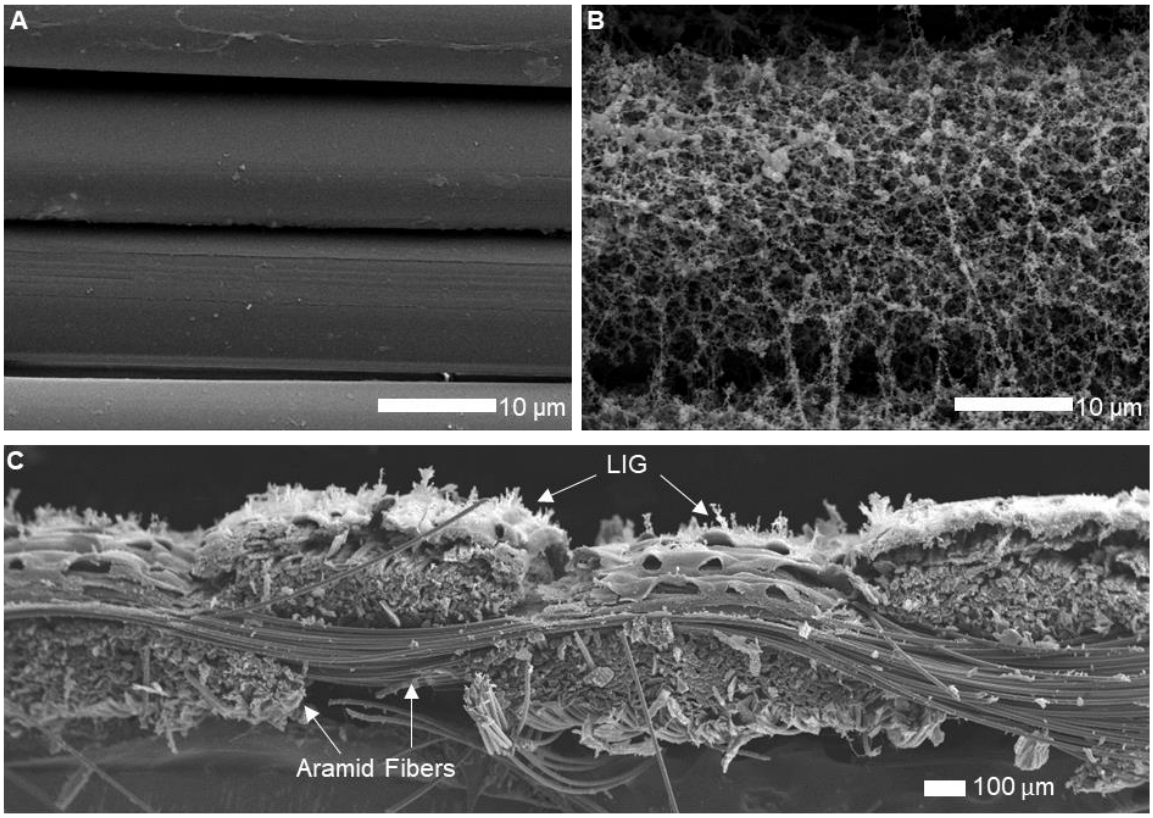

Figure 5.1. SEM image of (A) untreated aramid fibers, and (B) LIG microstructure on aramid fiber. (C) LIG conversion of the top aramid fibers with the rest of the aramid fibers within the fabric intact.

5.3. Ballistic Impact Test

5.3.1. Ballistic Sample Preparation and Experimental Test Setup

After LIG was generated on the aramid fabric surface (see Figure 5.2A), three 3 by 3-inch plies of aramid fabric were combined into a laminate using vacuum assisted resin transfer molding (VARTM; see Figure 5.2B). Epon 862 and Curing Agent W (100:26.4) resin were used as the matrix, and the laminates were cured under vacuum at 100 psi and 177 °C for 3 hours in a hot press. After the laminate was fabricated, two silver paint rings were added to each side of the LIG-treated composites to enable electrical resistance measurements during ballistic testing using the

four-point probe method. Next, 33-gauge copper wires were attached to the surface of each silver paint ring using additional silver paint and electrical tape. In order to monitor the average resistance of the entire composite during ballistic impact, the silver paint rings shown in Figure 5.2A and Figure 5.2B were designed to connect the three plies of the composite around the perimeter. As such, the final measured resistance values represented an average value for the entire composite specimen. For clarity, a schematic of the four-point probe resistance monitoring schematic is shown in Figure 5.3A-B.

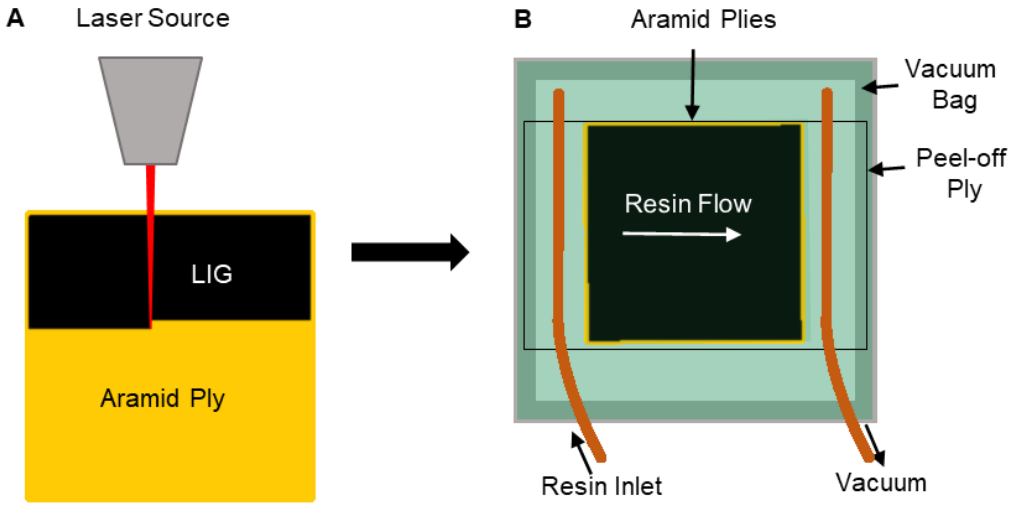

Figure 5.2. Flow chart schematic of (A) the LIG generation on aramid fabric to the (B) vacuum assisted resin transfer molding of the LIG-treated aramid laminate.

Following sample preparation, the composite laminates were impacted using the same customized gas gun as described and shown in section 4.6.1. The samples were placed between two steel plates with a 2.5-inch diameter target region to constrain any undesired motion of the laminate during testing. Once the composite was securely fixed, the barrel of the gas gun was placed 0.25 inches away from the center of the composite (Figure 5.3C). The projectile, comprised of 4130 alloy steel with a mass of 29 g and an 11.4 diameter hemispherical face, was propelled down the barrel by releasing a predetermined gas pressure. Two photogates, placed 19.5 mm apart at the end of the barrel, were used to measure the amount of time needed for the projectile to pass

between them, thus allowing for the calculation of the projectile velocity at the point of impact. To quantify the ballistic performance of each sample set, the V_{50} is considered as the figure of merit. The V_{50} ballistic limit is calculated by averaging the three lowest speeds at which the bullet penetrated and the three highest speeds at which the bullet did not penetrate the composite specimen. During ballistic testing, the copper wires attached to the outermost silver paint rings were used to apply 4 mA direct current through the sample using a BK Precision® model 9130 triple output programmable DC power supply, while the voltage was simultaneously measured across the copper wires attached to the two innermost silver paint rings using a National Instruments 4431 data acquisition system (DAQ) (see Figure 5.3A-B).

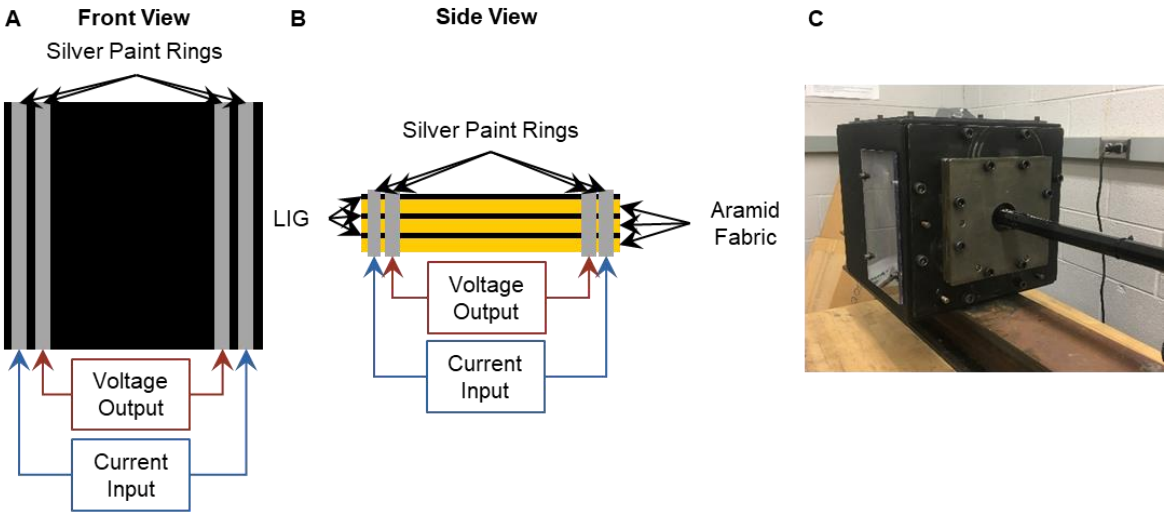

Figure 5.3. (A) Front view schematic of four-point probe resistance monitoring adopted on an aramid composite with LIG. (B) Side view schematic of four-point probe resistance monitoring adopted on an aramid composite with LIG. (C) Image of ballistic setup.

5.3.2. Ballistic Impact Test Results

The V_{50} ballistic limit, or the ballistic performance, of a composite can assist in both understanding the limits of the material for specific applications and aiding in the prediction of the extent of damage experienced by the composite based on the ballistic impact velocity. In this work, the V_{50} of the LIG-treated aramid fiber composites were compared to untreated aramid fiber

composites to ensure that the LIG treatment did not negatively affect the ballistic performance of the composites. A total of 12 untreated samples and 12 LIG-treated samples were prepared, of which at least 5 samples were penetrated by the projectile and at least 5 samples successfully stopped the projectile from penetrating. In order to qualify as penetrating the composite, 100% of the projectile was required to pass through the composite and impact the clay trap located 2 inches behind the composite. The projectile velocities for each sample set along with the penetration status and the resulting V_{50} values for untreated and LIG-treated samples are shown in Table 5.1. It can be noted that the larger range in impact speed for the LIG-treated composites was used to collect a wider and more complete range of data points as the authors investigated a relationship between the impact velocity and percent change in resistance, as shown Figure 5.1B. For this reason, additional impact speeds were reported for LIG-treated aramid composites relative to the untreated composites (see Table 5.1). With regards to ballistic limit, the 6 speeds used to calculate the V_{50} for the untreated samples ranged between 22.1 m/s and 26.6 m/s for a span of 4.5 m/s, while the LIG-treated samples ranged between 19.1 m/s and 23.5 m/s for a range of 4.4 m/s. Therefore, the V_{50} for both the untreated and LIG-treated samples were obtained over a similar range, which allowed for an accurate comparison of their ballistic limit.

Table 5.1. Projectile speed and penetration status of each ballistic test used to calculate the V_{50} of untreated and LIG-treated aramid fiber-reinforced composites.

Untreated Aramid Composite		**LIG-Treated Aramid Composite**	
Impact Speed (m/s)	**Penetration**	**Impact Speed (m/s)**	**Penetration**
18.2	No	6.9	No
20.2	No	10.0	No
21.0	No	19.1	No
22.1	No	20.0	No
23.4	No	21.3	Yes
25.4	No	23.0	No
25.6	Yes	23.1	Yes
26.0	Yes	23.5	Yes
26.6	Yes	25.0	Yes
28.2	Yes	26.0	Yes
29.8	Yes	38.0	Yes
30.5	Yes	48.0	Yes
		81.6	Yes
V_{50} = 24.6 m/s		**V_{50} = 21.7 m/s**	

Although a knowledge of the ballistic limit of LIG-treated aramid composites is important when predicting the amount of damage experienced by the composite, a direct comparison between the V_{50} of the untreated and LIG-coated aramid composites does not provide an accurate representation of the relative ballistic performance of each sample set. The weight of the aramid fabric is reduced during the irradiation process as the exterior fibers, which are exposed to the laser, are converted to a porous graphene interface. This conversion results in lower areal density aramid composites. Given that the areal density of a fabric is important to the ballistic performance, the areal-density-specific V_{50} presents a more reliable parameter for comparison. Therefore, for accuracy, the areal-density-specific V_{50} was calculated for each sample set by dividing the raw V_{50}

value by the respective areal density. Specifically, the weight of the three untreated and three LIG-treated plies were measured and divided by the area of the sample (7.62 cm x 7.62 cm), resulting in areal-densities of 0.073 g/cm^2 for the untreated aramid fabric plies, and 0.062 g/cm^2 for the LIG-treated plies. When normalized, the areal-density-specific V_{50} was found to be 0.033 m^3/s/g and 0.035 m^3/s/g for the untreated and LIG-treated fabric, respectively. Based on the normalized V_{50}, the ballistic performance of the LIG-treated composite was improved relative to that of the untreated aramid composite. This finding can be attributed to the increased friction between the LIG-treated aramid fabric surface and the surrounding matrix, as the LIG provides an interlocking mechanism and increases surface area interactions. Therefore, the ability of the projectile to penetrate the composite was reduced, and the ballistic energy absorption performance of the aramid laminates increased.

5.3.3. In-situ Impact Damage Detection of LIG-Coated Aramid Composites

To investigate this relationship, varying projectile velocities were tested and the correlation between the percent change in resistance and the projectile velocity was evaluated (see Figure 5.4B). The velocity was increased from approximately 7 m/s to 81 m/s and the corresponding change in electrical resistance increased from less than 1% to over 55%. As the velocity increased, the amount of damage and change in resistance also increased while the laminate absorbed some portion of the impact energy. This resulted in significant fiber fracture and delamination. A quadratic fit was applied to the resistance percent change vs impact velocity (see Figure 5.4B), and with a nonlinear least squares regression analysis, the quadratic fit predicted the trend of the resistance percent change and velocity with a coefficient of determination (R^2) value of 0.72. The relationship between the velocity and the percent change in resistance thus followed a quadratic trend through the range investigated, which was attributed to the similarly quadratic relationship

between velocity and kinetic energy. Therefore, it can be concluded that the energy absorbed by the composite was loosely related to the kinetic energy of the projectile. Although additional factors such as friction were expected to have an effect, this assumption allowed for the approximate prediction of the velocity using the percent change in resistance.

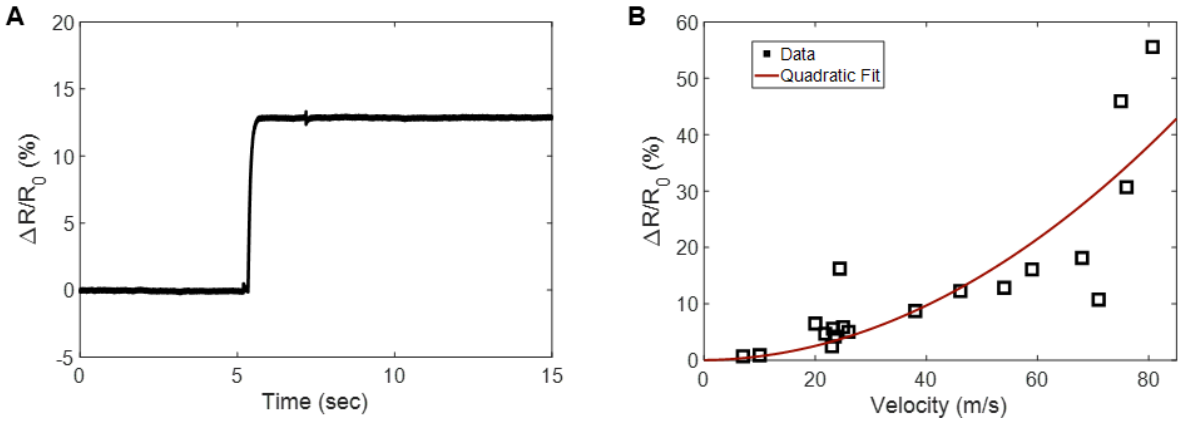

Figure 5.4. (A) Representative change in resistance of one ballistic impact sample. (B) Change in resistance percent change vs. velocity of impact for LIG-treated aramid fiber composites.

To further investigate the method of energy absorption and thus gain greater understanding of the previously observed trend between electrical resistance change and ballistic impact velocity, the impacted laminates were visually examined and compared. It is shown through macroscopic visual inspection that the plies comprising each laminate delaminated during impact, which introduced air pockets between the plies. This delamination was expected to further damage the LIG, thus increasing the electrical resistance of the sample. Moreover, from visual inspection the inter-ply delamination was more prominent as projectile velocity increased, which reduced carbon-carbon contact area in each LIG layer and resulted in a larger percent increase in the electrical resistance of the sample. For reference, Figure 5.5 shows four representative samples which are damaged with increasing impact velocities (see Figure 5.5A-H) and their corresponding percent change in resistance (see Figure 5.5I). As the velocity increased, the delaminated area—which is visible as the lighter portion of the composite from the top surface approximated by dashed black

contours—and the laminates cross section grew larger. Additionally, the fibers surrounding the impact hole in the composite, resulting from the penetration of the projectile, also show increased damage in the form of fiber failure. Therefore, the increase in resistance is dictated by the size of the damage due to penetration in addition to the delamination area which are both shown to increase with increasing impact velocities.

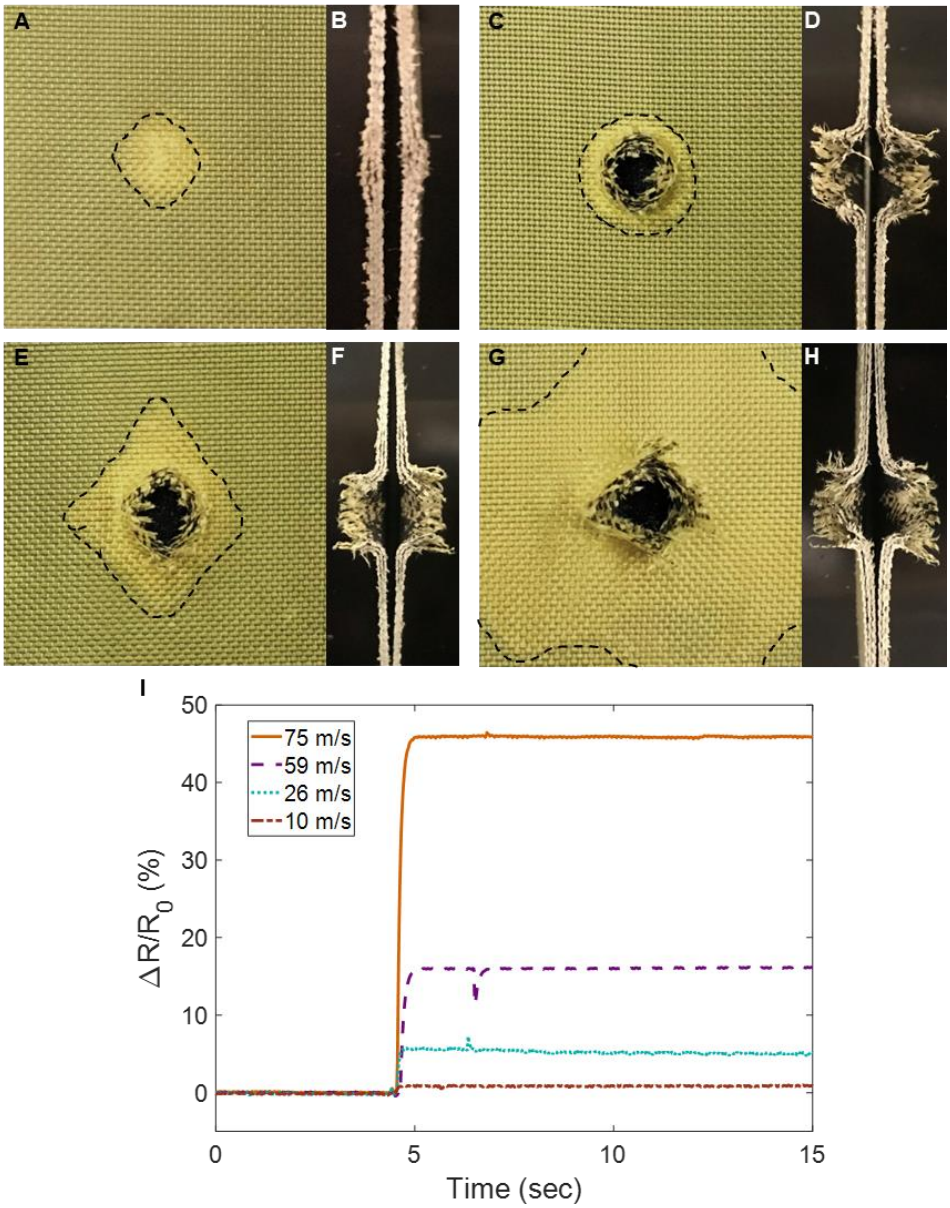

Figure 5.5. Images of impacted laminates with increased delamination between the composite plies imaged from the top surface at speeds of (A) 10 m/s, (C) 26 m/s, (E) 59 m/s, (G) 75 m/s and cross-section images at speeds of (B) 10 m/s, (D) 26 m/s, (F) 59 m/s, and (H) 75 m/s. (I) Corresponding percent change in resistance for each sample.

5.4. Mode I Interlaminar Fracture Toughness Test

5.4.1. Mode I Interlaminar Fracture Toughness Sample Preparation and Test Setup

The Mode I interlaminar fracture toughness of the LIG-treated aramid FRPCs were assessed as recommended per ASTM D5528-13. Specifically, each laminate was fabricated by VARTM (see Figure 5.2B) and consisted of 16 plies of aramid fabric with an EPON 862/Curing Agent W resin system. In order to form a pre-crack within the laminate, a 50 mm Teflon sheet was inserted between the two center plies. It should be noted that in order to enable in-situ resistance measurements, the two center plies were treated with LIG and the LIG interfaces were placed facing each other (see Figure 5.6A). The composite plate was then cut using a diamond saw to specimens which were 14 cm long, 23 mm wide, and 3 mm thick as recommended in the ASTM standard. Loading hinges were attached to the outer surfaces of each sample using a high shear strength epoxy (Loctite® 9430™ Hysol®) which was cured in an oven at 83 °C for 1 hour.

The completed samples were tested using an Instron model 5982 load frame with a 100 kN load cell at a crosshead extension rate of 2 mm/min (Figure 5.6B). After the crack was allowed to propagate to the length of the Teflon pre-crack, the Teflon insert was removed and copper wires were attached to each LIG surface using silver paint and electrical tape. Throughout the duration of the test, the electrical resistance between the two copper wires, and thus the two LIG plies, was measured as the delamination extended along the length of the specimen using a Wheatstone bridge with a constant voltage input provided by a Hewlett Packard model 6217A DC power supply. A schematic of the resistance monitoring method is shown in Figure 5.6A.

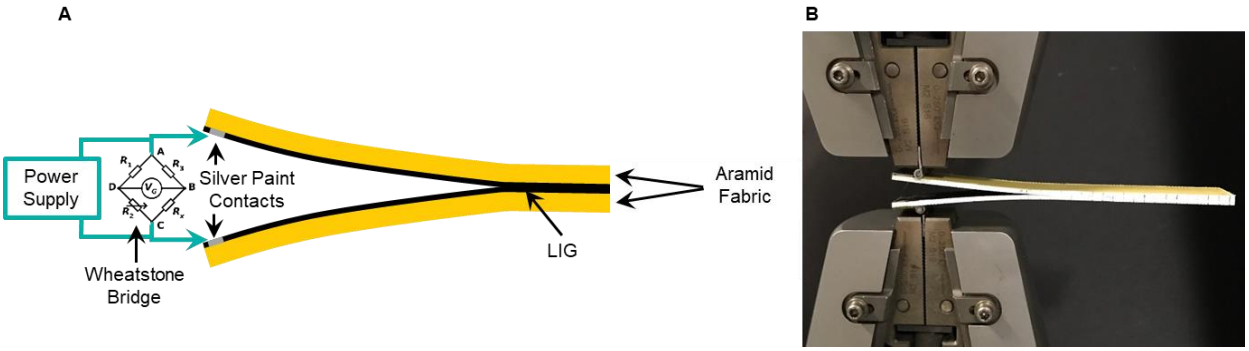

Figure 5.6. (A) Schematic of resistance monitoring method with increasing crack length during Mode I testing. (B) Mode I interlaminar fracture toughness setup.

5.4.2. Mode I Interlaminar Fracture Toughness Test Results

Given that the interlaminar region of composites are typically prone to failure, it is important that the Mode I interlaminar fracture toughness of the composite is not compromised when LIG is added to the interlaminar region. At least 5 samples of both untreated aramid composites and LIG-treated aramid composites were tested to calculate the Mode I interlaminar fracture toughness. Figure 5.7 shows the average fracture toughness (see Figure 5.7A) and a representative fracture toughness vs extension curve (see Figure 5.7B) for an untreated and a LIG-treated sample. As shown in Figure 5.7, the interlaminar fracture toughness of the untreated aramid composite was 437 J/m^2, and the LIG-treated composites exhibited an increased interlaminar fracture toughness at 476 J/m^2.

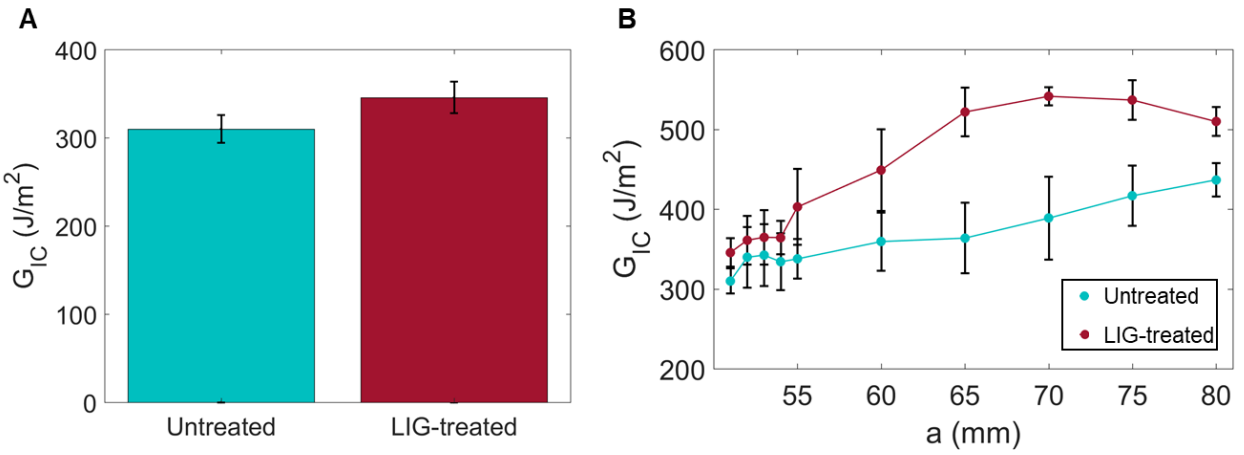

Figure 5.7. Mode I interlaminar fracture toughness of untreated aramid composite and LIG-treated aramid composite. (A) Average fracture toughness. (B) Representative fracture toughness vs. extension plots.

The improved fracture toughness can be attributed to an interlocking mechanism from the fibrous LIG microstructure mechanically bridging the gap between adjacent plies. The mechanism required more energy to drive crack propagation in the double cantilever beams. A similar mechanism has been previously reported in the literature, and is often termed as "nanostitching" [227,268,269]. The fracture surface images of the LIG-treated aramid Mode I samples are shown in Figure 5.8. While stick slip behavior is shown in Figure 5.8A-B, the interlaminar failure mode is a cohesive one, allowing the LIG-aramid fiber composites to withstand higher loads as the crack propagates within the interlaminar region. Figure 5.8C and D demonstrate this strong adhesion between the LIG and epoxy resin as there is a substantial amount of epoxy blocks remaining on the fracture surface. These findings are in agreement with other studies that report cohesive failure in LIG coated aramid fiber Mode I interlaminar fracture toughness samples [227]. Taken together, the added LIG interface appears to improve the fracture toughness of the aramid FRPCs and contributes to piezoresistance.

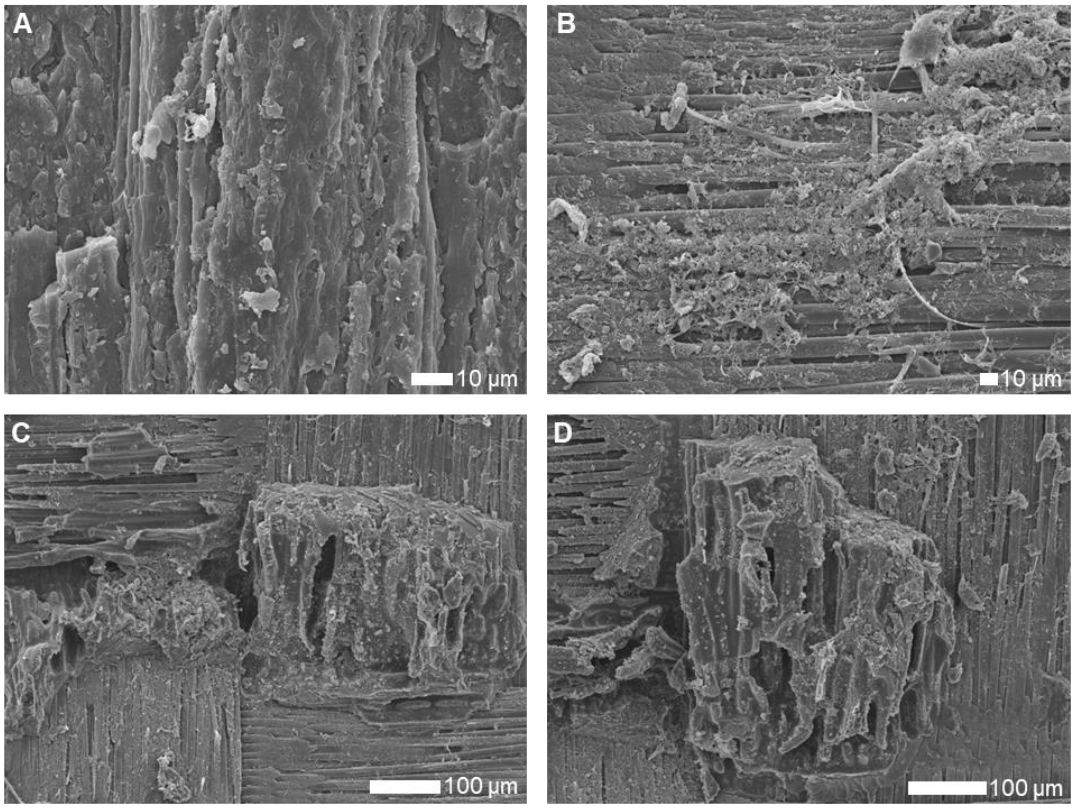

Figure 5.8. (A, B, C, D) Mode I interlaminar fracture toughness fracture surfaces of LIG-treated aramid fiber-reinforced composite.

5.4.3. Damage Detection Monitoring During Mode I Interlaminar Fracture Toughness Test

In addition to investigating the interfacial reinforcing capabilities of the LIG, the ability of the LIG to detect delamination between LIG interfaces was also simultaneously evaluated during Mode I interlaminar fracture toughness testing. The applied load and change in resistance with increasing crosshead extension of a representative Mode I sample is shown in Figure 5.9A. It is immediately clear from the figure that there is a strong correlation between the load and change in resistance with crosshead extension. As the extension increased and the double cantilever beam sample was delaminated, the crack length increased while the load required to pull apart the specimen and propagate the crack decreased. When the decreasing trend in the load was observed, the rate of change in the double cantilever beams resistance increased, thus showing a correlation

between delamination and electrical resistance. When the extension reached 22 mm, the load decreased dramatically, indicating rapid crack propagation within the interlaminar region. The dramatic load decrease was accompanied by a significant increase in specimen resistance, which resulted in a confirmed direct correlation between crack growth and change in resistance. This finding suggests that the piezoresistive LIG not only detects delamination, but it can also provide insight into the rate at which the delamination grows. For additional analysis, the relationship between the change in the resistance of the double cantilever beam and the crack length is shown in Figure 5.9B. Overall, the percent change in resistance increased with increasing crack length, which correlated with an increase in inter-ply delamination. As the crack propagated through the interlaminar region, the conductive contacts between the LIG surfaces decreased, therefore, restricting current pathways and causing a measured increase in resistance. Thus, the LIG exhibited multifunctionality in both reinforcing the interface between plies and enabling structural health monitoring of a failure-prone area within fiber-reinforced composites.

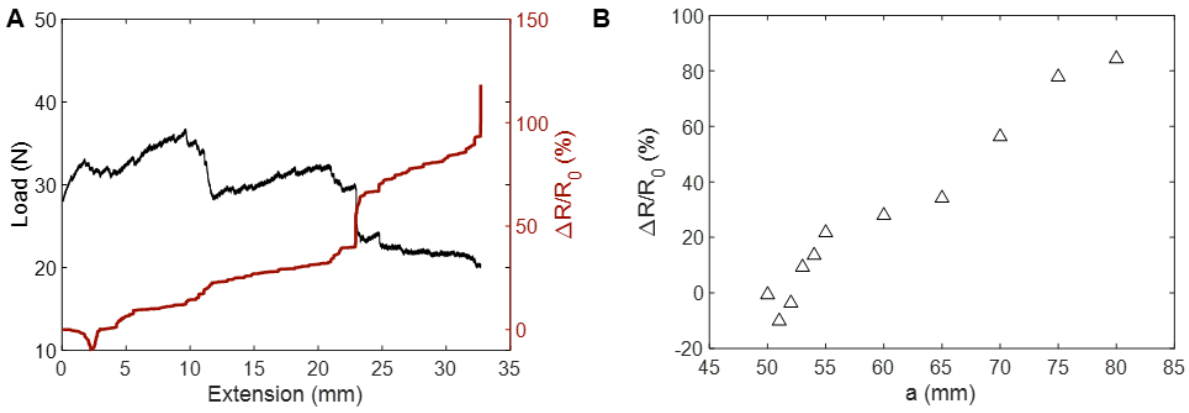

Figure 5.9. (A) Applied load and percent change in resistance versus extension during Mode I interlaminar fracture toughness test. (B) Percent change in resistance versus crack length during Mode I interlaminar fracture toughness test.

5.5. Chapter Summary

This chapter presented a method for in-situ impact and delamination damage detection for aramid FRPCs using an integrated piezoresistive LIG interphase. There are several benefits of this approach that make it a viable alternative to existing approaches. First, the addition of the LIG does not add extra weight or interlaminar thickness to the sample and does not require external bonding given that the LIG is generated using the aramid fibers as a precursor. Furthermore, the LIG process does not require extreme processing conditions and can be completed at room temperature and atmospheric pressure using a commercial CO_2 laser printer which contributes to the scalability of the method.

The LIG-treated aramid FRPCs were successfully shown to detect ballistic damage in-situ using a four-point probe resistance monitoring method and the percent change in electrical resistance was found to directly correlate to the projectile impact velocity. Therefore, a prediction of failure, damage extent, and projectile impact velocity can be made through correlation of resistance change and projectile velocity. Mode I interlaminar fracture toughness testing also evaluated the relation between change in resistance and generated delamination; a common form of damage experienced by ballistic composites. Results indicate that the addition of LIG within the aramid composite was shown to improve both the areal-density-specific V_{50} and the Mode I interlaminar fracture toughness. Thus, the results of this work demonstrate the multifunctionality of LIG-treated aramid composites and shows that the LIG piezoresistivity can be exploited to predict impact velocity and delamination extent, providing an estimate of the scope of damage sustained by the composites during ballistic impact.

Chapter 6. Conclusion

Ballistic materials have made great strides throughout history to improve protection from a wide variety of threats; however, as these threats continue to increase, the protection ballistic materials offer needs to be enhanced while remaining lightweight. Two popular ballistic materials are ultra-high molecule weight polyethylene (UHMWPE) and aramid fibers for their unique properties such as high strength-to-weight ratio, impact resistance, energy absorption, and wear and abrasion resistance. These fibers are used in a wide range of industries that require structural components, such as automotive, aerospace, marine, medical, and sporting goods.

In ballistic applications, these fibers are used in the form of fiber-reinforced polymer composites (FRPCs) and woven fabrics as hard and soft body armor, respectively. One major limitation of such FRPCs is that the fiber-matrix interface is prone to failure due to weak adhesion between the two components. A lack of chemical bonding and mechanical interlocking at the interface as well as a difference in stiffness between the fiber and the matrix often leads to stress concentrations that are prone to failure during loading conditions. Specifically, when UHMWPE and aramid fibers are used in FRPCs, this interface is substantially weaker than other reinforcing fibers due to the fact that they lack functional groups on their surface, which results weak adhesion with the matrix. In addition, when UHMWPE and aramid fibers are woven into a fabric, they exhibit low friction between the yarns. This low inter-yarn friction causes yarn slippage and yarn pullout that reduces the structural packing of the fabric. As a result, the impact energy is not shared with secondary yarns, and the load is solely absorbed by the primary yarns, which causes fabric failure to happen at lower impact speeds.

Research efforts aiming to improve the UHMWPE and aramid fiber interfacial properties in FRPCs and inter-yarn friction in woven fabrics have resulted in the development of chemical and nanoscale surface modifications. Yet, these surface treatments have some disadvantages, including that they (a) compromise the structural integrity of the fiber, (b) are not scalable, and (c) and can be cost- and time-inefficient. This dissertation sought to improve the interfacial and inter-yarn properties of UHMWPE and aramid fibers through the use of three nanomaterials-based surface modifications: aramid nanofibers (ANFs), zinc oxide nanowires (ZnO NWs), and laser induced graphene (LIG). These fibers were selected because they all have been shown to be simple, benign, and scalable interphase design methods [186,210,227]

Chapter 2 explored the use of an ANF interphase to improve the interfacial properties of UHWMPE composites under quasi-static loading. The UHMWPE fiber surface was first functionalized using an oxygen plasma treatment to improve adhesion with the ANF interphase. The ANF was then grafted to the UHWMPE fiber surface through a simple dip-coating process for various treatment periods. Through Fourier-transform infrared spectroscopy (FTIR) and X-ray photoelectron spectroscopy (XPS) analysis, it was determined that the ANF interphase increased the polar functional group concentrations on the UHMWPE fiber surfaces. Through scanning electron microscopy (SEM) and atomic force microscopy (AFM), it was shown that the UHMWPE fiber surface roughness was increased with the introduction of the ANFs. Single-fiber tensile testing demonstrated the benign nature of the treatment through preserved tensile strength of the treated UHMWPE fibers. Due to the enhanced surface area interactions and chemical bonding between the ANF-coated UHWMPE fiber and the epoxy matrix, the interfacial shear strength (IFSS) was found to increase by 173% after a 3 min ANF dip-coating treatment as assessed through

single-fiber pullout. Thus, it was shown that the ANF interphase was capably of reinforcing the UHMWPE fiber to improve the interfacial properties of UHMWPE composites.

Expanding on the use of a nanostructure interphase in UHWMPE composites, ZnO NWs were used to improve interfacial properties (Chapter 3). The UHMWPE fibers were first oxygen plasma-treated for various durations to study and optimize the adhesion of the ZnO NWs to the surface of the fibers. Post-functionalization, the UHMWPE surface chemical structure was examined using FTIR and XPS analysis and demonstrated an increase in oxygen functional groups with increased plasma treatment duration. Through SEM imaging, the morphology and uniformity of the growth on the UHMWPE fiber were characterized, and the grown ZnO NWs were shown to be consistent between the varying oxygen plasma treatment durations. The benign nature of the oxygen plasma treatment and subsequent ZnO NW growth were also confirmed through the preservation of the tensile strength. Using single-fiber pullout testing, the interfacial shear strength of ZnO NW-coated UHMWPE composites showed a maximum increase in IFSS of 135%. The ZnO NW interphase was capable of reinforcing the UHMWPE composite through enhanced surface area interactions and mechanical interlocking between the fiber and the matrix. It was also revealed that the performance of the ZnO NW interphase was found to correlate with the amount of the C=O (ketone) functional group on the fiber surface. Therefore, it was demonstrated that the IFSS of UHMWPE FRPCs can be significantly increased with a simple surface modification consisting of an oxygen plasma functionalization and the grafting of a ZnO NW interphase.

Building on the previously discuss surface treatment, ZnO interphase was also exploited to improve inter-yarn friction and ballistic performance of UHMWPE fabrics (Chapter 4). Oxygen plasma functionalization was performed on the UHWMPE fabric surface prior to the ZnO NW growth to enhance the adhesion of the ZnO NWs to the surface. Through XPS, the surface

chemistry was examined, and results showed that the oxygen functional group concentration increased as plasma treatment durations increased. The ZnO NWs were grown by means of a hydrothermal growth process and the morphology, uniformity, and quality of growth was characterized by SEM imaging. The ZnO NW reinforcement on woven UHMWPE fabric was found to improve the pullout load and pullout energy by a maximum of 663.5% and 822.9%, respectively. In addition, projectile impact testing confirmed that the V_{50} ballistic limit and energy absorption of the ZnO NW-coated fabric is increased by a 59.13% and 227%, respectively. The improvement in inter-yarn friction and impact performance are the result of the ZnO NWs providing enhanced mechanical interlocking and increased surface area interactions between neighboring yarns, which limits their movement. Taken together, these results demonstrate the effectiveness of a ZnO NW interphase in improving inter-yarn friction, impact performance, and the energy absorption of woven UHMWPE fabrics.

The use of a nanostructured and piezoresistive LIG interphase was also studied in aramid FRPC for improving ballistic and structural performance, as well as in-situ impact damage and delamination detection (Chapter 5). A commercial laser printer was used to directly generate LIG on the aramid fabric surface before being fabricated into aramid composites. SEM was used to characterize the morphology and penetration depth of the LIG interphase, which was shown to completely cover and create a conductive top surface. The LIG-treated aramid composites' interlaminar fracture toughness and areal-density-specific V_{50} increased relative to untreated aramid composites. This experienced increase was due to the LIG microstructure mechanically bridging between adjacent plies and providing an interlocking mechanism between the fabric and matrix. The percent change in electrical resistance was monitored during ballistic impact and was found to correlate with the projectile impact velocity due to fiber breakage and delamination

damaging the LIG interface. A relationship between change in electrical resistance and generated delamination length and rate of growth was also established by measuring electrical resistance during Mode I interlaminar fracture toughness testing. In sum, these findings demonstrate an effective method to generate an LIG interlayer in aramid-based composites to provide multifunctionality in both improving the structural and ballistic aramid composite performance and with in-situ sensing of damage and delamination.

6.1 Contribution

The main contribution of this dissertation is the novel design methods that were shown to improve the interfacial and inter-yarn properties of UHMWPE and aramid fibers This was done by modifying the originally inert surface of the UHMWPE and aramid fibers with nanomaterial-based surface modifications that significantly improve the weak interfacial adhesion in FRPCs and fiber-fiber interactions in woven fabric. Dissertation findings support the use of these fibers in ballistic protection applications and as high-performance composites in structural applications. The methodological and empirical contributions made in this dissertation are detailed in the following paragraphs.

The first contribution of this dissertation is the establishment of a simple and fast method to adhere ANFs onto the originally smooth and inert surface of UHMPWE fibers. The ANF interphase was well-adhered through enhanced chemical interactions by means of an oxygen plasma surface functionalization, followed by a short dip-coating process. The nanostructured ANF interphase considerably roughens the UHMWPE surface and populates it with polar functional groups that improve the chemical interactions and induce mechanical interlocking at the fiber matrix interface which significantly improve the IFSS of UHMWPE composites. This

ANF interphase design technique is scalable and can be integrated in UHMWPE composites to advance their use in structural applications.

The second contribution of this work is development of the technique for adhering ZnO NWs to UHWMPE fiber surfaces, which are originally smooth and non-reactive. By studying different oxygen plasma functionalization durations on the UHWMPE fiber surface to add ketone functional groups, the ZnO NW adhesion was optimized after only a 30 s plasma treatment. The ZnO NW interphase offers a substantially increased surface area interactions and mechanical interlocking mechanism between the fiber and the epoxy matrix which considerably improve the IFSS of the UHWMPE composite. The simple, fast, and effective nature of a ZnO NW interphase makes it easy to integrate into structural applications of UHMWPE composites and allow for expanding their use.

Another contribution of this dissertation is revealing the use of a ZnO NW interphase in UHWMPE fabric for soft body armor applications. Oxygen functional groups, specifically the ketone functional group, were introduced to the UHMWPE fabric surface using varying oxygen plasma treatment durations to improve the ZnO NW adhesion, where an optimal treatment duration of 30 s was determined. The ZnO NWs improve the yarn pullout load, ballistic limit, and energy absorption of the fabric through increased mechanical interlocking between the yarns. The quick, benign, and effect nature of this process significantly improves inter-yarn friction, which enhances the ballistic performance of woven UHWMPE and can advance its use in ballistic protection applications without compromising weight limitations.

The last contribution of this work is the introduction of an LIG interlayer in aramid fiber composites to add multifunctionality. The LIG was generated directly on the aramid surface using a CO_2 laser printer, which photo-thermally converts the top aramid surface into a textured

conductive graphitic layer while limiting the penetration depth, leaving the majority of the aramid fibers intact. The LIG-treated aramid composites demonstrated improved interlaminar fracture toughness and areal-density-specific V_{50} properties. Using the LIG interphase for in-situ structural health monitoring (SHM), failure prediction, damage extent, and projectile impact velocity can be made through establishing a correlation between the change in electrical resistance and projectile velocity. The LIG interphase also was shown to provide a relationship between change in electrical resistance and both generated delamination length and rate of growth in the LIG-treated aramid composites under Mode I loading conditions. These results demonstrate the multifunctional ability of the LIG interphase in aramid composites for a reinforcing material in structural and ballistic applications while also enabling in-situ SHM of failure-prone areas within FRPCs, which has direct use in military applications in vehicles and armor.

6.2 Recommendations for Future Work

This dissertation describes research to improve interfacial adhesion and inter-yarn friction in UHMWPE and aramid woven fabric, and FRPCs. The findings and results in this work demonstrate the use of the three benign, simple, and scalable nano-material based surface modifications to improve the interfacial adhesion and inter-yarn friction. This research has led to significant scientific contributions that can be used to further advance the use of polymer fibers in structural and ballistic applications as woven fabrics and composites through the integration of nanomaterials. However, additional tasks and further studies can be done to expand the knowledge of these nanomaterial reinforcements and their potential applications.

In this dissertation, the varying dip-coating treatment periods of ANF were assessed on a 30 s oxygen-plasma functionalized UHMWPE fiber surface for improved IFSS of UHWMPE composites. However, future studies should examine whether varying the surface oxygen-plasma

functionalization time and including different surface functionalization treatments improves the ANF adhesion through enhanced chemical interactions to the UHMWPE fiber surface and thus, further improve the IFSS of UHWMPE composites. Also, future studies can aim to exploit different ANF morphologies and study their effect on the interfacial properties of the composite to further optimize the ANF interphase on the UHWMPE fiber. The ANF aspect ratio and geometry can be modified by changing parameters related to the dissolution and deprotonation process used for synthesis. The type and concentration of the base used for the ANF solution can be varied, resulting ANFs with larger aspect ratios that have the potential to further improve the interphase performance.

While it has been proven that an ANF and ZnO NW reinforcement improve the interfacial properties of single-fiber UHMWPE composites, the macro-scale properties of reinforced UHMWPE FRPCs have yet to be explored. The next step would be to fabricate UHMWPE composite laminates with ANF and ZnO NW reinforcement on the surface of the woven UHWMPE fabric and examine macro-scale composites properties, such as short beam strength and interlaminar fracture toughness. Although UHMWPE already has a high wear and abrasion resistant property, the effect the nano-material reinforcements could be an interesting area of study to reveal any potential contributions to an improved high wear and abrasion performance.

The improved impact performance of a ZnO NW reinforcement on woven UHMWPE fabric has been demonstrated; however, the stab performance has yet to be explored. It has been proven that through increased surface area interactions and mechanical interlocking that the ZnO NWs increase the inter-yarn friction between the UHMWPE yarns, reduce yarn pullout, and limit windowing failure during impact. These results are expected to translate to an improved stab resistance performance in ZnO NW-coated UHMWPE woven fabric. In addition, the potential of

ANFs as a reinforcement in woven fabrics has yet to be explored, along with their effect on impact and stab performance. Since aramid fibers are known to exhibit excellent ballistic properties, it would be an interesting to investigate if their ballistic performance translates to ANFs and use an ANF reinforcement on UHMWPE woven fabric for the potential improvement of inter-yarn friction, ballistic limit, and energy absorption. Studying the impact performance of UHMWPE composites with nano-scale reinforcements is also recommended as future work due to the fact that ANFs and ZnO NWs have been investigated and proven to improve the interfacial property of single-fiber UHMWPE composites.

The LIG-treated aramid composites in this dissertation were shown to exhibit improved ballistic performance and were capable of detecting damage during impact tests and delamination through the mode I fracture toughness testing. A next step would be to assess the ability for performing in-situ damage localization during impact tests, both along the 2D plane and through the thickness of the composite. The ability of the LIG to improve the multifunctionality of aramid composites through its piezoresistivity would also be an interesting topic to be further investigated, for example, using joule heating to perform out-of-autoclave curing, in-situ bonding/repair of LIG-treated aramid composite, and thermal damage and delamination detection using an IR-camera. Because aramids are known to suffer greatly in structural applications due to their moisture sensitivity, an important parameter to look at is how environmental factors would affect the LIG interphase, and therefore, its ballistic performance along and in-situ damage and delamination detection properties.

References

[1] Reports and Data, Ultra High Molecular Weight Polyethylene [UHMWPE] market, 2020-2028. https://www.reportsanddata.com/report-detail/ultra-high-molecular-weight-polyethylene-uhmwpe-market, n.d. (accessed 11 October 2021).

[2] Grand View Research, Para-aramid fibers market size & share, industry report, 2019-2025. https://www.grandviewresearch.com/industry-analysis/para-aramid-fibers-market, 2019 (accessed 11 October 2021).

[3] Computational & Multiscale Mechanics of Materials, Fracture mechanics online class. http://www.ltas-cm3.ulg.ac.be/FractureMechanics/?p=overview_P3, n.d. (accessed 20 October 2021).

[4] A. Majumdar, B.S. Butola, A. Srivastava, An analysis of deformation and energy absorption modes of shear thickening fluid treated Kevlar fabrics as soft body armour materials, Mater. Des. 51 (2013) 148–153. https://doi.org/10.1016/J.MATDES.2013.04.016.

[5] B.A. Cheeseman, T.A. Bogetti, Ballistic impact into fabric and compliant composite laminates, Compos. Struct. 61 (2003) 161–173. https://doi.org/10.1016/S0263-8223(03)00029-1.

[6] O.E., İşmal, R. Paul, 17 - Composite textiles in high-performance apparel, in: J. McLoughlin, T. Sabir (Eds.), High-Performance Apparel: Materials, Development, and Applications, Woodhead Publishing Series in Textiles, United Kingdom, 2018, pp. 377–420. https://doi.org/10.1016/B978-0-08-100904-8.00019-5 (accessed 8 October 2021).

[7] T. Tam, A. Bhatnagar, High performance ballistic fibers, in: Light. Ballist. Compos. Mil. Law-Enforcement Appl., Elsevier Inc., 2006, pp. 189–209. https://doi.org/10.1533/9781845691554.2.189.

[8] C. on R. of T.P.U. by the D. to T. CombatHelmets, B. on A.S. and Technology, D. on E. and P. Sciences, N.R. Council, Evolution of Combat Helmets based, (2014). https://www.ncbi.nlm.nih.gov/books/NBK224907/ (accessed 10 October 2021).

[9] Smithsonian Magazine, How the military helmet evolved from a hazard to a bullet shield. https://www.smithsonianmag.com/smithsonian-institution/how-military-helmet-evolved-hazard-bullet-shield-180963319/ , 2017 (accessed 10 October 2021).

[10] Small Wars Journal, The history of body armor, from medieval times to today . https://smallwarsjournal.com/jrnl/art/the-history-of-body-armor-from-medieval-times-to-today , 2017 (accessed 8 October 2021).

[11] MarketsandMarkets, Ballistic protection market by material, product, technology, threat level, platform, applicationCOVID-19 impact analysis. https://www.marketsandmarkets.com/Market-Reports/ballistic-protection-market-30112278.html , n.d. (accessed 10 October 2021).

[12] Grand View Research, Ballistic composites market size & share industry report, 2018-2025. https://www.grandviewresearch.com/industry-analysis/ballistic-composites-market , 2017 (accessed 10 October 2021).

[13] Armor Materials Market Share & Forecast Report, 2020-2027. https://www.reportsanddata.com/report-detail/armor-materials-market , n.d. (accessed 10 October 2021).

[14] A. Peacock, Handbook of Polyethylene : Structures: Properties, and Applications, first ed., CRC Press, Boca Raton, 2000. https://doi.org/10.1201/9781482295467.

[15] M. Vlasblom, The manufacture, properties, and applications of high-strength, high-modulus polyethylene fibers, in: Handb. Prop. Text. Tech. Fibres, Elsevier, 2018: pp. 699–755. https://doi.org/10.1016/B978-0-08-101272-7.00018-3.

[16] H. Van Der Werff, U. Heisserer, High-performance ballistic fibers: Ultra-high molecular weight polyethylene (UHMWPE), Adv. Fibrous Compos. Mater. Ballist. Prot. (2016) 71–107. https://doi.org/10.1016/B978-1-78242-461-1.00003-0.

[17] P. Bajaj, Sriram, Ballistic protective clothing: An overview, Indian Journal of Fibre & Textile Research 22 (1997) 274–291.

[18] J.K. Fink, Aramids, High Perform. Polym. (2014) 301–320. https://doi.org/10.1016/B978-0-323-31222-6.00013-3.

[19] M. Hosur, N. Wagner, C.T. Sun, V. Rangari, J. Gillespie, S. Jeelani, H. Mahfuz, Development of flexible extremities protection utilizing shear thickening fluid/fabric composites, 2012.

[20] J.W.S. Hearle, High-performance fibres, Woodhead Publishing Limited, England, 2001.

[21] E.G. Chatzi, J.L. Koenig, Polymer-plastics technology and engineering morphology and structure of Kevlar fibers: A review, Polymer-Plastics Technology and Engineering 26 (1987) 229270. https://doi.org/10.1080/03602558708071938.

[22] M. Jassal, S. Ghosh, Aramid fibres-An overview, Indian Journal of Fibre & Textile Research 27 (2002) 290–306.

[23] Y. Chu, S. Min, X. Chen, Numerical study of inter-yarn friction on the failure of fabrics upon ballistic impacts, Mater. Des. 115 (2017) 299–316. https://doi.org/10.1016/j.matdes.2016.11.013.

[24] Y. Chu, X. Chen, Finite element modelling effects of inter-yarn friction on the single-layer high-performance fabrics subject to ballistic impact, Mech. Mater. 126 (2018) 99–110. https://doi.org/10.1016/j.mechmat.2018.08.003.

[25] Y. Zhou, M. Ali, X. Gong, D. Yang, An overview of yarn pull-out behavior of woven fabrics, Text. Res. J. 89 (2019) 223–234. https://doi.org/10.1177/0040517517741156.

[26] M.P. Rao, Y. Duan, M. Keefe, B.M. Powers, T.A. Bogetti, Modeling the effects of yarn material properties and friction on the ballistic impact of a plain-weave fabric, Compos. Struct. 89 (2009) 556–566. https://doi.org/10.1016/j.compstruct.2008.11.012.

[27] C. Ha-Minh, F. Boussu, T. Kanit, D. Crépin, A. Imad, Effect of frictions on the ballistic performance of a 3D warp interlock fabric: Numerical analysis, Appl. Compos. Mater. 19 (2012) 333–347. https://doi.org/10.1007/s10443-011-9202-2.

[28] B.J. Briscoe, F. Motamedi, The ballistic impact characteristics of aramid fabrics: The influence of interface friction, Wear. 158 (1992) 229–247. https://doi.org/10.1016/0043-1648(92)90041-6.

[29] Y. Duan, M. Keefe, T.A. Bogetti, B.A. Cheeseman, B. Powers, A numerical investigation of the influence of friction on energy absorption by a high-strength fabric subjected to ballistic impact, Int. J. Impact Eng. 32 (2006) 1299–1312. https://doi.org/10.1016/j.ijimpeng.2004.11.005.

[30] X.S. Zeng, V.B.C. Tan, V.P.W. Shim, Modelling inter-yarn friction in woven fabric armour, Int. J. Numer. Methods Eng. 66 (2006) 1309–1330. https://doi.org/10.1002/nme.1596.

[31] J.M. Hofsté, J.A. Schut, A.J. Pennings, The effect of chromic acid treatment on the mechanical and tribological properties of aramid fibre reinforced ultra-high molecular weight polyethylene composite, J. Mater. Sci. Mater. Med. 9 (1998) 561–566. https://doi.org/10.1023/A:1008957324878.

[32] S.-H. Lu, G.-Z. Liang, Z.-W. Zhou, F. Li, Structure and properties of UHMWPE fiber/carbon fiber hybrid composites, J. Appl. Polym. Sci. 101 (2006) 1880–1884. https://doi.org/10.1002/app.24071.

[33] K. K. Chawla, Composite Materials: Science and Engineering, third ed., Springer, New York, 2012.

[34] M.R. Wisnom, The role of delamination in failure of fibre-reinforced composites, Philos.

Trans. R. Soc. A Math. Phys. Eng. Sci. 370 (2012) 1850–1870. https://doi.org/10.1098/rsta.2011.0441.

[35] N.J. Pagano, G.A. Schoeppner, Delamination of polymer matrix composites: Problems and assessment, in: Compr. Compos. Mater., Elsevier, 2000, pp. 433–528. https://doi.org/10.1016/b0-08-042993-9/00073-5.

[36] M.W. Hyer, Stress Analysis of Fiber-Reinforced Composite Materials, DEStech Publications, Inc., Pennsylvania, 2009.

[37] S. Arora, A. Majumdar, B.S. Butola, Structure induced effectiveness of shear thickening fluid for modulating impact resistance of UHMWPE fabrics, Compos. Struct. 210 (2019) 41–48. https://doi.org/10.1016/j.compstruct.2018.11.028.

[38] L.-L. Sun, D.-S. Xiong, C.-Y. Xu, Application of shear thickening fluid in ultra high molecular weight polyethylene fabric, J. Appl. Polym. Sci. 129 (2013) 1922–1928. https://doi.org/10.1002/app.38844.

[39] W. Li, D. Xiong, X. Zhao, L. Sun, J. Liu, Dynamic stab resistance of ultra-high molecular weight polyethylene fabric impregnated with shear thickening fluid, Mater. Des. 102 (2016) 162–167. https://doi.org/10.1016/j.matdes.2016.04.006.

[40] G. Juan, H. Xian-cong, L. Yan, W. Xin-ling, S. Mei-wu, Z. Zhen, Improving the stab-resistance performance of ultra high molecular weight polyethylene fabric intercalated with nano-silica-fluid, J. Shanghai Jiaotong Univ. 19 (2014) 102–109. https://doi.org/10.1007/s12204-013-1467-1.

[41] D. Firouzi, D.A. Foucher, H. Bougherara, Nylon-coated ultra high molecular weight polyethylene fabric for enhanced penetration resistance, J. Appl. Polym. Sci. 131 (2014) 40350. https://doi.org/10.1002/app.40350.

[42] Y. Chu, X. Chen, L. Tian, Modifying friction between ultra-high molecular weight polyethylene (UHMWPE) yarns with plasma enhanced chemical vapour deposition (PCVD), Appl. Surf. Sci. 406 (2017) 77–83. https://doi.org/10.1016/j.apsusc.2017.02.109.

[43] S. Arora, A. Majumdar, B. Singh Butola, Interplay of fabric structure and shear thickening fluid impregnation in moderating the impact response of high-performance woven fabrics, J. Compos. Mater. 54 (2020) 4387–4395. https://doi.org/10.1177/0021998320932991.

[44] S.-G. Lee, T.-J. Kang, T.-H. Yoon, Enhanced interfacial adhesion of ultra-high molecular weight polyethylene (UHMWPE) fibers by oxygen plasma treatment, J. Adhes. Sci. Technol. 12 (2012) 731–748. https://doi.org/10.1163/156856198X00263.

[45] S.I. Moon, J. Jang, Factors affecting the interfacial adhesion of ultrahigh-modulus polyethylene fibre-vinylester composites using gas plasma treatment, J. Mater. Sci. 33

(1998) 3419–3425. https://doi.org/10.1023/A:1013205918208.

[46] S.I. Moon, J. Jang, The effect of the oxygen-plasma treatment of UHMWPE fiber on the transverse properties of UHMWPE-fiber/vinylester composites, Compos. Sci. Technol. 59 (1999) 487–493. https://doi.org/10.1016/S0266-3538(98)00093-1.

[47] B. Tissington, G. Pollard, I.M. Ward, A study of the influence of fibre/resin adhesion on the mechanical behaviour of ultra-high-modulus polyethylene fibre composites, J. Mater. Sci. 26 (1991) 82–92. https://doi.org/10.1007%2FBF00576036

[48] P. Masse, J.P. Cavrot, P. François, J.M. Lefebvre, B. Escaig, Adhesion improvement of high modulus polyethylene fibers by surface plasma treatment: Evaluation by pull-out testing, Polym. Compos. 15 (1994) 247–251. https://doi.org/10.1002/pc.750150311.

[49] S.G. Lee, T.J. Kang, T.H. Yoon, Enhanced interfacial adhesion of ultra-high molecular weight polyethylene (UHMWPE) fibers by oxygen plasma treatment, J. Adhes. Sci. Technol. 12 (1998) 731–748. https://doi.org/10.1163/156856198X00263.

[50] Y.F. Fu, K. Xu, J. Li, Z.Y. Sun, F.Q. Zhang, D.M. Chen, The influence of plasma surface treatment of carbon fibers on the interfacial adhesion properties of UHMWPE composite, Polym. Plast. Technol. Eng. 51 (2012) 273–276. https://doi.org/10.1080/03602559.2011.617406.

[51] R. He, F. Niu, Q. Chang, The effect of plasma treatment on the mechanical behavior of UHMWPE fiber-reinforced thermoplastic HDPE composite, Surf. Interface Anal. 50 (2018) 73–77. https://doi.org/10.1002/sia.6337.

[52] Y. Chu, R. Rahman, H. He, W. Huang, X. Chen, Increasing inter-yarn friction to ultra-high molecular weight polyethylene yarns for ballistic application by sol-gel treatment, J. Ind. Text. (2020). https://doi.org/10.1177/1528083720942960.

[53] R. Roy, A. Laha, N. Awasthi, A. Majumdar, B.S. Butola, Multi layered natural rubber coated woven P-aramid and UHMWPE fabric composites for soft body armor application, Polym. Compos. 39 (2018) 3636–3644. https://doi.org/10.1002/PC.24391.

[54] W.-Q. Yang, X.-Y. Liu, Y.-P. Yu, W.-D. Yu, Evaluation of stab resistance of coated UHMWPE fabric, Fibres Text. East. Eur. Nr 2 (2020) 76–79. https://doi.org/10.5604/01.3001.0013.7319.

[55] D. Firouzi, C.Y. Ching, S.N. Rizvi, P.R. Selvaganapathy, Development of oxygen-plasma-surface-treated UHMWPE fabric coated with a mixture of SiC/polyurethane for protection against puncture and needle threats, Fibers 7 (2019) 46. https://doi.org/10.3390/FIB7050046.

[56] L. Shanmugam, M.E. Kazemi, Z. Li, W. Luo, Y. Xiang, L. Yang, J. Yang, Low-velocity

impact behavior of UHMWPE fabric/thermoplastic laminates with combined surface treatments of polydopamine and functionalized carbon nanotubes, Compos. Commun. 22 (2020) 100527. https://doi.org/10.1016/J.COCO.2020.100527.

[57] X. Liu, M. Li, X. Li, X. Deng, X. Zhang, Y. Yan, Y. Liu, X. Chen, Ballistic performance of UHMWPE fabrics/EAMS hybrid panel, J. Mater. Sci. 2018 5310. 53 (2018) 7357–7371. https://doi.org/10.1007/S10853-018-2055-4.

[58] I. Khan, G. Hussain, K.A. Al-Ghamdi, R. Umer, Investigation of impact strength and hardness of UHMW polyethylene composites reinforced with nano-hydroxyapatite particles fabricated by friction stir processing, Polym. 11 (2019) 1041. https://doi.org/10.3390/POLYM11061041.

[59] Z. Zheng, X. Tang, M. Shi, G. Zhou, A study of the influence of controlled corona treatment on UHMWPE fibres in reinforced vinylester composites, Polym. Int. 52 (2003) 1833–1838. https://doi.org/10.1002/pi.1372.

[60] Y. Hu, Y. Shi, D. Liu, J. Guo, J. Zhang, Z. Chen, Damage tolerance of 2-dimentional UHMWPE/CF hybrid woven laminates subjected to low-velocity impact, Mater. Des. 191 (2020) 108604. https://doi.org/10.1016/J.MATDES.2020.108604.

[61] J.L. Holloway, A.M. Lowman, M.R. VanLandingham, G.R. Palmese, Chemical grafting for improved interfacial shear strength in UHMWPE/PVA-hydrogel fiber-based composites used as soft fibrous tissue replacements, Compos. Sci. Technol. 85 (2013) 118–125. https://doi.org/10.1016/j.compscitech.2013.06.007.

[62] A.P. Kharitonov, A. V. Maksimkin, K.S. Mostovaya, S.D. Kaloshkin, M. V. Gorshenkov, T.P. D'yachkova, A.G. Tkachev, L.N. Alekseiko, Reinforcement of bulk ultrahigh molecular weight polyethylene by fluorinated carbon nanotubes insertion followed by hot pressing and orientation stretching, Compos. Sci. Technol. 120 (2015) 26–31. https://doi.org/10.1016/j.compscitech.2015.10.009.

[63] S. Chhetri, H. Bougherara, A comprehensive review on surface modification of UHMWPE fiber and interfacial properties, Compos. Part A Appl. Sci. Manuf. 140 (2021) 106146. https://doi.org/10.1016/j.compositesa.2020.106146.

[64] W. Li, L. Meng, R. Ma, Effect of surface treatment with potassium permanganate on ultra-high molecular weight polyethylene fiber reinforced natural rubber composites, Polym. Test. 55 (2016) 10–16. https://doi.org/10.1016/J.POLYMERTESTING.2016.08.006.

[65] Y. Muraoka, M.J. Rich, L.T. Drzal, Sulfonation of UHMW-PE fibers for adhesion promotion in epoxy polymers, J. Adhes. Sci. Technol. 16 (2012) 1669–1685. https://doi.org/10.1163/15685610260255279.

[66] M.S. Silverstein, O. Breuer, Mechanical properties and failure of etched UHMW-PE

fibres, J. Mater. Sci. 1993 2815. 28 (1993) 4153–4158. https://doi.org/10.1007/BF00351246.

[67] W. Li, R. Li, C. Li, Z.-R. Chen, L. Zhang, Mechanical properties of surface-modified ultra-high molecular weight polyethylene fiber reinforced natural rubber composites, Polym. Compos. 38 (2017) 1215–1220. https://doi.org/10.1002/PC.23685.

[68] R. Oosterom, T.J. Ahmed, J.A. Poulis, H.E.N. Bersee, Adhesion performance of UHMWPE after different surface modification techniques, Med. Eng. Phys. 28 (2006) 323–330. https://doi.org/10.1016/j.medengphy.2005.07.009.

[69] Z. Zheng, X. Tang, M. Shi, G. Zhou, A study of the influence of controlled corona treatment on UHMWPE fibres in reinforced vinylester composites, Polym. Int. 52 (2003) 1833–1838. https://doi.org/10.1002/PI.1372.

[70] T. Ogawa, H. Mukai, S. Osawa, Improvement of the mechanical properties of an ultrahigh molecular weight polyethylene fiber/epoxy composite by corona-discharge treatment, J. Appl. Polym. Sci. 79 (2001) 1162–1168. https://doi.org/10.1002/1097-4628(20010214)79:7<1162::AID-APP20>3.0.CO;2-Y.

[71] N. Bahramian, M. Atai, M.R. Naimi-Jamal, Ultra-high-molecular-weight polyethylene fiber reinforced dental composites: Effect of fiber surface treatment on mechanical properties of the composites, Dent. Mater. 31 (2015) 1022–1029. https://doi.org/10.1016/j.dental.2015.05.011.

[72] T. Ogawa, H. Mukai, S. Osawa, Effects of functional groups and surface roughness on interfacial shear strength in ultrahigh molecular weight polyethylene fiber/polyethylene system, J. Appl. Polym. Sci. 71 (1999) 243–249. https://doi.org/10.1002/(SICI)1097-4628(19990110)71:2<243::AID-APP7>3.0.CO;2-I.

[73] W.S. Gutowski, E.R. Pankevicius, A novel surface treatment process for enhanced adhesion of ultra-high modulus polyethylene fibres to epoxy resins, Compos. Interfaces. 1 (1993) 141–151. https://doi.org/10.1163/156855493x00031.

[74] Z. Li, W. Zhang, X. Wang, Y. Mai, Y. Zhang, Surface modification of ultra high molecular weight polyethylene fibers via the sequential photoinduced graft polymerization, Appl. Surf. Sci. 257 (2011) 7600–7608. https://doi.org/10.1016/j.apsusc.2011.03.134.

[75] J. Wang, G. Liang, W. Zhao, S. Lü, Z. Zhang, Studies on surface modification of UHMWPE fibers via UV initiated grafting, Appl. Surf. Sci. 253 (2006) 668–673. https://doi.org/10.1016/j.apsusc.2005.12.165.

[76] M.J. Martínez-Morlanes, P. Castell, V. Martínez-Nogués, M.T. Martinez, P.J. Alonso, J.A. Puértolas, Effects of gamma-irradiation on UHMWPE/MWNT nanocomposites,

Compos. Sci. Technol. 71 (2011) 282–288. https://doi.org/10.1016/j.compscitech.2010.11.013.

[77] M.S. Broujerdi, M. Masoomi, M. Asgari, Interfacial improvement and mechanical properties of epoxy resin/ultra-high molecular weight polyethylene fibre composites compatibilized with glycidyl methacrylate, J. Reinf. Plast. Compos. 32 (2013) 1675–1684. https://doi.org/10.1177/0731684413498520.

[78] Z. Zhang, G. Jiang, Y. Wu, F. Kong, J. Huang, Surface functional modification of ultrahigh molecular weight polyethylene fiber by atom transfer radical polymerization, Appl. Surf. Sci. 427 (2018) 410–415. https://doi.org/10.1016/j.apsusc.2017.08.159.

[79] S. Wang, J. Ma, X. Feng, J. Cheng, X. Ma, Y. Zhao, L. Chen, An effective surface modification of UHMWPE fiber for improving the interfacial adhesion of epoxy resin composites, Polym. Compos. 41 (2020) 1614–1623. https://doi.org/10.1002/pc.25483.

[80] Y. Lo Hsieh, M. Hartzell, S. Xu, Effects of acid oxidation on wetting and adhesion properties of ultra-high modulus and molecular weight polyethylene (UHMWPE) fibers, J. Adhes. Sci. Technol. 5 (1991) 1023–1039. https://doi.org/10.1163/156856191X00026.

[81] K. Wang, M. Liu, C. Song, L. Shen, P. Chen, S. Xu, Surface-conductive UHMWPE fibres via in situ reduction and deposition of graphene oxide, Mater. Des. 148 (2018) 167–176. https://doi.org/10.1016/j.matdes.2018.03.069.

[82] X. Jin, W. Wang, C. Xiao, T. Lin, L. Bian, P. Hauser, Improvement of coating durability, interfacial adhesion and compressive strength of UHMWPE fiber/epoxy composites through plasma pre-treatment and polypyrrole coating, Compos. Sci. Technol. 128 (2016) 169–175. https://doi.org/10.1016/j.compscitech.2016.03.026.

[83] J. Hu, X. Feng, Z. Liu, Y. Zhao, L. Chen, Surface amine-functionalization of UHMWPE fiber by bio-inspired polydopamine and grafted hexamethylene diamine, Surf. Interface Anal. 49 (2017) 640–646. https://doi.org/10.1002/sia.6203.

[84] G. Tang, X. Hu, T. Tang, C. Claramunt, C. Liu, Enhanced interfacial adhesion of UHMWPE fibers by alkali treatment and its behavior to PI resins, J. Thermoplast. Compos. Mater. 32 (2017) 52–61. https://doi.org/10.1177/0892705717743296.

[85] M. Mohammadalipour, M. Masoomi, M. Ahmadi, S. Safi, Interfacial shear strength characterization of GMA-grafted UHMWPE fiber/epoxy/nano clay hybrid nanocomposite materials, RSC Adv. 6 (2016) 41793–41799. https://doi.org/10.1039/c6ra05027a.

[86] M. Ahmadi, O. Zabihi, M. Masoomi, M. Naebe, Synergistic effect of MWCNTs functionalization on interfacial and mechanical properties of multi-scale UHMWPE fibre reinforced epoxy composites, Compos. Sci. Technol. 134 (2016) 1–11. https://doi.org/10.1016/j.compscitech.2016.07.026.

[87] L. Shanmugam, X. Feng, J. Yang, Enhanced interphase between thermoplastic matrix and UHMWPE fiber sized with CNT-modified polydopamine coating, Compos. Sci. Technol. 174 (2019) 212–220. https://doi.org/10.1016/j.compscitech.2019.03.001.

[88] L. Shanmugam, M.E. Kazemi, Z. Rao, D. Lu, X. Wang, B. Wang, L. Yang, J. Yang, Enhanced mode I fracture toughness of UHMWPE fabric/thermoplastic laminates with combined surface treatments of polydopamine and functionalized carbon nanotubes, Compos. Part B Eng. 178 (2019) 107450. https://doi.org/10.1016/J.COMPOSITESB.2019.107450.

[89] Y. Zhang, J. Yu, C. Zhou, L. Chen, Z. Hu, Preparation, morphology, and adhesive and mechanical properties of ultrahigh-molecular-weight polyethylene/SiO2 nanocomposite fibers, Polym. Compos. 31 (2010) 684–690. https://doi.org/10.1002/pc.20847.

[90] W. Li, M. Huang, R. Ma, Improved mechanical properties of epoxy composites reinforced with surface-treated UHMWPE fibers, Polym. Adv. Technol. 29 (2018) 1287–1293. https://doi.org/10.1002/PAT.4240.

[91] S. Gürgen, M.C. Kuşhan, The ballistic performance of aramid based fabrics impregnated with multi-phase shear thickening fluids, Polym. Test. 64 (2017) 296–306. https://doi.org/10.1016/J.POLYMERTESTING.2017.11.003.

[92] U. Mawkhlieng, A. Majumdar, D. Bhattacharjee, Graphene reinforced multiphase shear thickening fluid for augmenting low velocity ballistic resistance, Fibers Polym. 22 (2021) 213–221. https://doi.org/10.1007/S12221-021-0163-2.

[93] A. Majumdar, B.S. Butola, A. Srivastava, Development of soft composite materials with improved impact resistance using Kevlar fabric and nano-silica based shear thickening fluid, Mater. Des. 54 (2014) 295–300. https://doi.org/10.1016/J.MATDES.2013.07.086.

[94] A. Ghosh, A. Majumdar, B.S. Butola, Rheometry of novel shear thickening fluid and its application for improving the impact energy absorption of p-aramid fabric, Thin-Walled Struct. 155 (2020) 106954. https://doi.org/10.1016/J.TWS.2020.106954.

[95] P. Dixit, A. Ghosh, A. Majumdar, Hybrid approach for augmenting the impact resistance of p-aramid fabrics: grafting of ZnO nanorods and impregnation of shear thickening fluid, J. Mater. Sci. 54 (2019) 13106–13117. https://doi.org/10.1007/S10853-019-03830-Z.

[96] A. Laha, A. Majumdar, Shear thickening fluids using silica-halloysite nanotubes to improve the impact resistance of p-aramid fabrics, Appl. Clay Sci. 132–133 (2016) 468–474. https://doi.org/10.1016/J.CLAY.2016.07.017.

[97] S. Cao, H. Pang, C. Zhao, S. Xuan, X. Gong, The CNT/PSt-EA/Kevlar composite with excellent ballistic performance, Compos. Part B Eng. 185 (2020) 107793. https://doi.org/10.1016/J.COMPOSITESB.2020.107793.

[98] D.P. Kalman, R.L. Merrill, N.J. Wagner, E.D. Wetzel, Effect of particle hardness on the penetration behavior of fabrics intercalated with dry particles and concentrated particle−fluid suspensions, ACS Appl. Mater. Interfaces. 1 (2009) 2602–2612. https://doi.org/10.1021/AM900516W.

[99] M. Liu, S. Zhang, S. Liu, S. Cao, S. Wang, L. Bai, M. Sang, S. Xuan, W. Jiang, X. Gong, CNT/STF/Kevlar-based wearable electronic textile with excellent anti-impact and sensing performance, Compos. Part A Appl. Sci. Manuf. 126 (2019) 105612. https://doi.org/10.1016/J.COMPOSITESA.2019.105612.

[100] Z. Tan, W. Li, W. Huang, The effect of graphene on the yarn pull-out force and ballistic performance of Kevlar fabrics impregnated with shear thickening fluids, Smart Mater. Struct. 27 (2018) 075048. https://doi.org/10.1088/1361-665X/AACA4B.

[101] D. Sun, X. Chen, Plasma modification of Kevlar fabrics for ballistic applications, Tex. Res. J. 82 (2012) 1928–1934. https://doi.org/10.1177/0040517512450765.

[102] E.D. LaBarre, X. Calderon-Colon, M. Morris, J. Tiffany, E. Wetzel, A. Merkle, M. Trexler, Effect of a carbon nanotube coating on friction and impact performance of Kevlar, J. Mater. Sci. 50 (2015) 5431–5442. https://doi.org/10.1007/S10853-015-9088-8.

[103] J. Nasser, K. Steinke, L. Groo, H.A. Sodano, Improved interyarn friction, impact response, and stab resistance of surface fibrilized aramid fabric, Adv. Mater. Interfaces. 6 (2019) 1900881. https://doi.org/10.1002/admi.201900881.

[104] R. Nayak, S. Kanesalingam, L. Wang, R. Padhye, Stab resistance and thermophysiological comfort properties of boron carbide coated aramid and ballistic nylon fabrics, J. Tex. Inst. 110 (2018) 1159–1168. https://doi.org/10.1080/00405000.2018.1548800.

[105] S. Laurenzi, R. Pastore, G. Giannini, M. Marchetti, Experimental study of impact resistance in multi-walled carbon nanotube reinforced epoxy, Compos. Struct. 99 (2013) 62–68. https://doi.org/10.1016/J.COMPSTRUCT.2012.12.002.

[106] T.-T. Li, X. Cen, H. Peng, H. Ren, L. Han, C.-W. Lou, J.-H. Lin, Rheological response and quasi-static stab resistance of STF/MWCNTs-impregnated aramid fabrics with different textures, J. Ind. Text. 50 (2019) 380–397. https://doi.org/10.1177/1528083719830144.

[107] I. Taraghi, A. Fereidoon, F. Taheri-Behrooz, Low-velocity impact response of woven Kevlar/epoxy laminated composites reinforced with multi-walled carbon nanotubes at ambient and low temperatures, Mater. Des. 53 (2014) 152–158. https://doi.org/10.1016/J.MATDES.2013.06.051.

[108] A.H.I. Mourad, A.H. Idrisi, N. Zaaroura, M.M. Sherif, H. Fouad, Damage assessment of nanofiller-reinforced woven kevlar KM2plus/Epoxy resin laminated composites, Polym.

Test. 86 (2020) 106501. https://doi.org/10.1016/J.POLYMERTESTING.2020.106501.

[109] S. Sharma, S.R. Dhakate, A. Majumdar, B.P. Singh, Improved static and dynamic mechanical properties of multiscale bucky paper interleaved Kevlar fiber composites, Carbon N. Y. 152 (2019) 631–642. https://doi.org/10.1016/J.CARBON.2019.06.055.

[110] A. Majumdar, B.S. Butola, N. Awasthi, I. Chauhan, P. Hatua, Improving the mechanical properties of p-aramid fabrics and composites by developing ZnO nanostructures, Polym. Compos. 39 (2018) 3300–3306. https://doi.org/10.1002/PC.24346.

[111] A.S. Rahman, V. Mathur, R. Asmatulu, Effect of nanoclay and graphene inclusions on the low-velocity impact resistance of Kevlar-epoxy laminated composites, Compos. Struct. 187 (2018) 481–488. https://doi.org/10.1016/J.COMPSTRUCT.2017.12.054.

[112] D.M. Simić, D.B. Stojanović, M. Dimić, K. Mišković, M. Marjanović, Z. Burzić, P.S. Uskoković, A. Zak, R. Tenne, Impact resistant hybrid composites reinforced with inorganic nanoparticles and nanotubes of WS2, Compos. Part B Eng. 176 (2019) 107222. https://doi.org/10.1016/J.COMPOSITESB.2019.107222.

[113] M. Xia, Z. Quan, X. Wang, J. Yu, Preparation and characterization of B4C particle coated composites for stab-resistance, Compos. Struct. 228 (2019) 111370. https://doi.org/10.1016/J.COMPSTRUCT.2019.111370.

[114] C.Y. Yue, K. Padmanabhan, Interfacial studies on surface modified Kevlar fibre/epoxy matrix composites, Compos. Part B Eng. 30 (1999) 205–217. https://doi.org/10.1016/S1359-8368(98)00053-5.

[115] C. Jia, R. Zhang, C. Yuan, Z. Ma, Y. Du, L. Liu, Y. Huang, Surface modification of aramid fibers by amino functionalized silane grafting to improve interfacial property of aramid fibers reinforced composite, Polym. Compos. 41 (2020) 2046–2053. https://doi.org/10.1002/PC.25519.

[116] J. Nasser, J. Lin, H. Sodano, High strength fiber reinforced composites with surface fibrilized aramid fibers, J. Appl. Phys. 124 (2018) 045305. https://doi.org/10.1063/1.5026987.

[117] B. Wang, Y. Duan, J. Zhang, Titanium dioxide nanoparticles-coated aramid fiber showing enhanced interfacial strength and UV resistance properties, Mater. Des. 103 (2016) 330–338. https://doi.org/10.1016/J.MATDES.2016.04.085.

[118] L. Zhang, H. Kong, M. Qiao, X. Ding, M. Yu, Growing nano-SiO2 on the surface of aramid fibers assisted by supercritical CO2 to enhance the thermal stability, interfacial shear strength, and UV resistance, Polym. 2019, Vol. 11, Page 1397. 11 (2019) 1397. https://doi.org/10.3390/POLYM11091397.

[119] L. Zeng, X. Liu, X. Chen, C. Soutis, Surface modification of aramid fibres with graphene oxide for interface improvement in composites, Appl. Compos. Mater. 25 (2018) 843–852. https://doi.org/10.1007/S10443-018-9718-9.

[120] Y. Wu, B. Tang, K. Liu, X. Zeng, J. Lu, T. Zhang, X. Shen, Enhanced flexural properties of aramid fiber/epoxy composites by graphene oxide, Nanotechnol. Rev. 8 (2019) 484–492. https://doi.org/10.1515/NTREV-2019-0043.

[121] J. Tian, L. An, Y. Tan, T. Xu, X. Li, G. Chen, Graphene oxide-modified aramid fibers for reinforcing epoxy resin matrixes, ACS Appl. Nano Mater. 4 (2021) 9595–9605. https://doi.org/10.1021/ACSANM.1C02017.

[122] B. Suresha, N.M. Indushekhara, C.A. Varun, D. Sachin, K. Pranao, Effect of carbon nanotubes reinforcement on mechanical properties of aramid/epoxy hybrid composites, Mater. Today Proc. 43 (2021) 1478–1484. https://doi.org/10.1016/J.MATPR.2020.09.307.

[123] G. Kister, B. Ralph, G.F. Fernando, Damage detection in glass fibre-reinforced plastic composites using self-sensing E-glass fibres, Smart Mater. and Struct. 3 (2004) 1166. https://doi.org/10.1088/0964-1726/13/5/021.

[124] K.S.C. Kuang, W.J. Cantwell, Use of conventional optical fibers and fiber Bragg gratings for damage detection in advanced composite structures: A review, Appl. Mech. Rev. 56 (2003) 493–513. https://doi.org/10.1115/1.1582883.

[125] S. Huguet, N. Godin, R. Gaertner, L. Salmon, D. Villard, Use of acoustic emission to identify damage modes in glass fibre reinforced polyester, Compos. Sci. Technol. 62 (2002) 1433–1444. https://doi.org/10.1016/S0266-3538(02)00087-8.

[126] S. Barré, M.L. Benzeggagh, On the use of acoustic emission to investigate damage mechanisms in glass-fibre-reinforced polypropylene, Compos. Sci. Technol. 52 (1994) 369–376. https://doi.org/10.1016/0266-3538(94)90171-6.

[127] L. Böger, M.H.G. Wichmann, L.O. Meyer, K. Schulte, Load and health monitoring in glass fibre reinforced composites with an electrically conductive nanocomposite epoxy matrix, Compos. Sci. Technol. 68 (2008) 1886–1894. https://doi.org/10.1016/j.compscitech.2008.01.001.

[128] S. Gao, R.-C. Zhuang, J. Zhang, J.-W. Liu, E. Mäder, Glass fibers with carbon nanotube networks as multifunctional sensors, Adv. Funct. Mater. 20 (2010) 1885–1893. https://doi.org/10.1002/adfm.201000283.

[129] I. Weber, P. Schwartz, Monitoring bending fatigue in carbon-fibre/epoxy composite strands: A comparison between mechanical and resistance techniques, Compos. Sci. Technol. 61 (2001) 849–853. https://doi.org/10.1016/S0266-3538(01)00028-8.

[130] M. Kupke, K. Schulte, R. Schüler, Non-destructive testing of FRP by d.c. and a.c. electrical methods, Compos. Sci. Technol. 61 (2001) 837–847. https://doi.org/10.1016/S0266-3538(00)00180-9.

[131] J.C. Abry, S. Bochard, A. Chateauminois, M. Salvia, G. Giraud, In situ detection of damage in CFRP laminates by electrical resistance measurements, Compos. Sci. Technol. 59 (1999) 925–935. https://doi.org/10.1016/S0266-3538(98)00132-8.

[132] K. Schulte, C. Baron, Load and failure analyses of CFRP laminates by means of electrical resistivity measurements, Compos. Sci. Technol. 36 (1989) 63–76. https://doi.org/10.1016/0266-3538(89)90016-X.

[133] M. Sánchez, R. Moriche, S.G. Prolongo, A.R. Marrón, A. Jiménez-Suárez, A. Ureña, Evaluation of sensitivity for detecting different failure modes of epoxy matrix composites doped with graphene nanoparticles, Compos. Struct. 225 (2019) 111167. https://doi.org/10.1016/j.compstruct.2019.111167.

[134] X. Du, H. Zhou, W. Sun, H.Y. Liu, G. Zhou, H. Zhou, Y.W. Mai, Graphene/epoxy interleaves for delamination toughening and monitoring of crack damage in carbon fibre/epoxy composite laminates, Compos. Sci. Technol. 140 (2017) 123–133. https://doi.org/10.1016/j.compscitech.2016.12.028.

[135] M. Nofar, S. V. Hoa, M.D. Pugh, Failure detection and monitoring in polymer matrix composites subjected to static and dynamic loads using carbon nanotube networks, Compos. Sci. Technol. 69 (2009) 1599–1606. https://doi.org/10.1016/j.compscitech.2009.03.010.

[136] N.D. Alexopoulos, C. Bartholome, P. Poulin, Z. Marioli-Riga, Structural health monitoring of glass fiber reinforced composites using embedded carbon nanotube (CNT) fibers, Compos. Sci. Technol. 70 (2010) 260–271. https://doi.org/10.1016/j.compscitech.2009.10.017.

[137] L. Gao, E.T. Thostenson, Z. Zhang, T.-W. Chou, Sensing of damage mechanisms in fiber-reinforced composites under cyclic loading using carbon nanotubes, Adv. Funct. Mater. 19 (2009) 123–130. https://doi.org/10.1002/adfm.200800865.

[138] D.J. Kwon, Z.J. Wang, J.Y. Choi, P.S. Shin, K.L. Devries, J.M. Park, Damage sensing and fracture detection of CNT paste using electrical resistance measurements, Compos. Part B Eng. 90 (2016) 386–391. https://doi.org/10.1016/j.compositesb.2016.01.020.

[139] M. Tehrani, A.Y. Boroujeni, T.B. Hartman, T.P. Haugh, S.W. Case, M.S. Al-Haik, Mechanical characterization and impact damage assessment of a woven carbon fiber reinforced carbon nanotube-epoxy composite, Compos. Sci. Technol. 75 (2013) 42–48. https://doi.org/10.1016/j.compscitech.2012.12.005.

[140] F.H. Gojny, M.H.G. Wichmann, U. Köpke, B. Fiedler, K. Schulte, Carbon nanotube-reinforced epoxy-composites: Enhanced stiffness and fracture toughness at low nanotube content, Compos. Sci. Technol. 64 (2004) 2363–2371. https://doi.org/10.1016/j.compscitech.2004.04.002.

[141] K. Imielińska, M. Castaings, R. Wojtyra, J. Haras, E. Le Clezio, B. Hosten, Air-coupled ultrasonic C-scan technique in impact response testing of carbon fibre and hybrid: Glass, carbon and Kevlar/epoxy composites, in: J. Mater. Process. Technol., 2004: pp. 513–522. https://doi.org/10.1016/j.jmatprotec.2004.07.143.

[142] S. Fidan, T. Sınmazcelik, E. Avcu, M. Ozgur Bora, O. Coban, Detecting impact damages in an aramid / glass fiber reinforced hybrid composite with micro tomography, Advanced Materials Research. 445 (2012) 9–14. https://doi.org/10.4028/www.scientific.net/AMR.445.9.

[143] J. Parthenios, D.G. Katerelos, G.C. Psarras, C. Galiotis, Aramid fibers; a multifunctional sensor for monitoring stress/strain fields and damage development in composite materials, Eng. Fract. Mech. 69 (2002) 1067–1087. https://doi.org/10.1016/S0013-7944(01)00123-0.

[144] I. Zivkovic, A. Kojovic, R. Aleksic, I. Živković, K. Maksimović, A. Kojović, R. Aleksić, Analysis of smart aramid fiber reinforced laminar thermoplastic composite material under static loading. https://www.researchgate.net/publication/265892293 , 2008 (accessed 2 February 2020).

[145] C. Caneva, I.M. De Rosa, F. Sarasini, Damage mechanisms in loaded aramid composites by means of embedded PVDF acoustic emission sensors, Advanced Materials Research. 13-14 (2006) 337–342. https://doi.org/10.4028/www.scientific.net/AMR.13-14.337.

[146] L. Groo, D.J. Inman, H.A. Sodano, In situ damage detection for fiber-reinforced composites using integrated zinc oxide nanowires, Adv. Funct. Mater. 28 (2018) 1802846. https://doi.org/10.1002/adfm.201802846.

[147] H. Dai, E.T. Thostenson, T. Schumacher, Processing and characterization of a novel distributed strain sensor using carbon nanotube-based nonwoven composites, Sensors 15 (2015) 17728–17747. https://doi.org/10.3390/S150717728.

[148] H. Dai, G.J. Gallo, T. Schumacher, E.T. Thostenson, A novel methodology for spatial damage detection and imaging using a distributed carbon nanotube-based composite sensor combined with electrical impedance tomography, J. Nondestruct. Eval. 35 (2016) 26. https://doi.org/10.1007/S10921-016-0341-0.

[149] S. Luo, W. Obitayo, T. Liu, SWCNT-thin-film-enabled fiber sensors for lifelong structural health monitoring of polymeric composites - From manufacturing to utilization to failure, Carbon N. Y. 76 (2014) 321–329. https://doi.org/10.1016/J.CARBON.2014.04.083.

[150] O. Rodríguez-Uicab, C. Martin-Barrera, A. May-Pat, A. Can-Ortiz, P. Gonzalez-Chi, F. Avilés, Electrical self-sensing of strain and damage of thermoplastic hierarchical composites subjected to monotonic and cyclic tensile loading, J. of Intell. Mater. Systs and Struct. 30 (2019) 1527–1537. https://doi.org/10.1177/1045389X19835962.

[151] M. Yang, K. Cao, L. Sui, Y. Qi, J. Zhu, A. Waas, E.M. Arruda, J. Kieffer, M.D. Thouless, N.A. Kotov, Dispersions of aramid nanofibers: A new nanoscale building block, ACS Nano. 5 (2011) 6945–6954. https://doi.org/10.1021/nn2014003.

[152] B. Yang, L. Wang, M. Zhang, J. Luo, Z. Lu, X. Ding, Fabrication, applications, and prospects of aramid nanofiber, Adv. Funct. Mater. 30 (2020) 2000186. https://doi.org/10.1002/ADFM.202000186.

[153] Y. Fan, Z. Li, J. Wei, Application of aramid nanofibers in nanocomposites: A brief review, Polym. 13 (2021) 3071. https://doi.org/10.3390/POLYM13183071.

[154] K. Cao, C.P. Siepermann, M. Yang, A.M. Waas, N.A. Kotov, M.D. Thouless, E.M. Arruda, Reactive aramid nanostructures as high-performance polymeric building blocks for advanced composites, Adv. Funct. Mater. 23 (2013) 2072–2080. https://doi.org/10.1002/adfm.201202466.

[155] J. Nasser, L. Zhang, H. Sodano, Aramid nanofiber interlayer for improved interlaminar properties of carbon fiber/epoxy composites, Compos. Part B Eng. 197 (2020) 108130. https://doi.org/10.1016/j.compositesb.2020.108130.

[156] S.-O. Tung, S. Ho, M. Yang, R. Zhang, N.A. Kotov, A dendrite-suppressing composite ion conductor from aramid nanofibres, Nat. Commun. 2015 6 (2015) 6152. https://doi.org/10.1038/ncomms7152.

[157] M. Wang, A. Emre, S. Tung, A. Gerber, D. Wang, Y. Huang, V. Cecen, N.A. Kotov, Biomimetic solid-state Zn2+ electrolyte for corrugated structural batteries, ACS Nano. 13 (2019) 1107–1115. https://doi.org/10.1021/ACSNANO.8B05068.

[158] Q. Kuang, D. Zhang, J.C. Yu, Y.-W. Chang, M. Yue, Y. Hou, M. Yang, Toward record-high stiffness in polyurethane nanocomposites using aramid nanofibers, J. Phys. Chem. C. 119 (2015) 27467–27477. https://doi.org/10.1021/ACS.JPCC.5B08856.

[159] J. Fan, J. Wang, Z. Shi, S. Yu, J. Yin, Kevlar nanofiber-functionalized multiwalled carbon nanotubes for polymer reinforcement, Mater. Chem. Phys. 141 (2013) 861–868. https://doi.org/10.1016/J.MATCHEMPHYS.2013.06.015.

[160] J. Zhu, W. Cao, M. Yue, Y. Hou, J. Han, M. Yang, Strong and stiff aramid nanofiber/carbon nanotube nanocomposites, ACS Nano. 9 (2015) 2489–2501. https://doi.org/10.1021/NN504927E.

[161] S.A. Shah, D. Kulhanek, W. Sun, X. Zhao, S. Yu, D. Parviz, J.L. Lutkenhaus, M.J. Green, Aramid nanofiber-reinforced three-dimensional graphene hydrogels for supercapacitor electrodes, J. Colloid Interface Sci. 560 (2020) 581–588. https://doi.org/10.1016/J.JCIS.2019.10.066.

[162] S.R. Kwon, M.B. Elinski, J.D. Batteas, J.L. Lutkenhaus, Robust and flexible aramid nanofiber/graphene layer-by-layer electrodes, ACS Appl. Mater. Interfaces. 9 (2017) 17125–17135. https://doi.org/10.1021/ACSAMI.7B03449.

[163] J. Fan, Z. Shi, M. Tian, J. Yin, Graphene–aramid nanofiber nanocomposite paper with high mechanical and electrical performance, RSC Adv. 3 (2013) 17664–17667. https://doi.org/10.1039/C3RA42515K.

[164] J. Lyu, X. Wang, L. Liu, Y. Kim, E.K. Tanyi, H. Chi, W. Feng, L. Xu, T. Li, M.A. Noginov, C. Uher, M.D. Hammig, N.A. Kotov, High strength conductive composites with plasmonic nanoparticles aligned on aramid nanofibers, Adv. Funct. Mater. 26 (2016) 8435–8445. https://doi.org/10.1002/ADFM.201603230.

[165] M. Lin, Y. Li, K. Xu, Y. Ou, L. Su, X. Feng, J. Li, H. Qi, D. Liu, Thermally conductive nanostructured, aramid dielectric composite films with boron nitride nanosheets, Compos. Sci. Technol. 175 (2019) 85–91. https://doi.org/10.1016/J.COMPSCITECH.2019.02.006.

[166] K. Wu, J. Wang, D. Liu, C. Lei, D. Liu, W. Lei, Q. Fu, Highly thermoconductive, thermostable, and super-flexible film by engineering 1D rigid rod-like aramid nanofiber/2D boron nitride nanosheets, Adv. Mater. 32 (2020) 1906939. https://doi.org/10.1002/ADMA.201906939.

[167] L. Zong, Y. Yang, H. Yang, X. Wu, Shapeable aerogels of metal–organic-frameworks supported by aramid nanofibrils for efficient adsorption and interception, ACS Appl. Mater. Interfaces. 12 (2020) 7295–7301. https://doi.org/10.1021/ACSAMI.9B22466.

[168] Q. Yin, H. Jia, A. Mohamed, Q. Ji, L. Hong, Highly flexible and mechanically strong polyaniline nanostructure @ aramid nanofiber films for free-standing supercapacitor electrodes, Nanoscale. 12 (2020) 5507–5520. https://doi.org/10.1039/C9NR09272B.

[169] Y. Li, G. Ren, Z. Zhang, C. Teng, Y. Wu, X. Lu, Y. Zhu, L. Jiang, A strong and highly flexible aramid nanofibers/PEDOT:PSS film for all-solid-state supercapacitors with superior cycling stability, J. Mater. Chem. A. 4 (2016) 17324–17332. https://doi.org/10.1039/C6TA06981A.

[170] L. Liu, J. Lyu, J. Mo, H. Yan, L. Xu, P. Peng, J. Li, B. Jiang, L. Chu, M. Li, Comprehensively-upgraded polymer electrolytes by multifunctional aramid nanofibers for stable all-solid-state Li-ion batteries, Nano Energy. 69 (2020) 104398. https://doi.org/10.1016/J.NANOEN.2019.104398.

[171] C. Zhu, J. Zhang, J. Xu, X. Yin, J. Wu, S. Chen, Z. Zhu, L. Wang, H. Wang, Aramid nanofibers/polyphenylene sulfide nonwoven composite separator fabricated through a facile papermaking method for lithium ion battery, J. Memb. Sci. 588 (2019) 117169. https://doi.org/10.1016/J.MEMSCI.2019.117169.

[172] S. on Tung, S.L. Fisher, N.A. Kotov, L.T. Thompson, Nanoporous aramid nanofibre separators for nonaqueous redox flow batteries, Nat. Commun. 2018 9 (2018) 4193. https://doi.org/10.1038/s41467-018-05752-x.

[173] Z. Cheng, Z. Bai, Y. Dai, L. Luo, X. Liu, Benzimidazole-containing aramid nanofiber for naked-eye detection of heavy metal ions, Analyst. 143 (2018) 5225–5233. https://doi.org/10.1039/C8AN01484A.

[174] Y. Li, S. Yuan, C. Zhou, Y. Zhao, B.V. der Bruggen, A high flux organic solvent nanofiltration membrane from Kevlar aramid nanofibers with in situ incorporation of microspheres, J. Mater. Chem. A. 6 (2018) 22987–22997. https://doi.org/10.1039/C8TA08518H.

[175] C. Nie, Y. Yang, Z. Peng, C. Cheng, L. Ma, C. Zhao, Aramid nanofiber as an emerging nanofibrous modifier to enhance ultrafiltration and biological performances of polymeric membranes, J. Memb. Sci. 528 (2017) 251–263. https://doi.org/10.1016/J.MEMSCI.2016.12.070.

[176] Z. Ma, S. Kang, J. Ma, L. Shao, A. Wei, C. Liang, J. Gu, B. Yang, D. Dong, L. Wei, Z. Ji, High-performance and rapid-response electrical heaters based on ultraflexible, heat-resistant, and mechanically strong aramid nanofiber/Ag nanowire nanocomposite papers, ACS Nano. 13 (2019) 7578–7590. https://doi.org/10.1021/ACSNANO.9B00434.

[177] P. Hu, J. Lyu, C. Fu, W. Gong, J. Liao, W. Lu, Y. Chen, X. Zhang, Multifunctional aramid nanofiber/carbon nanotube hybrid aerogel films, ACS Nano. 14 (2019) 688–697. https://doi.org/10.1021/ACSNANO.9B07459.

[178] C. Lei, Y. Zhang, D. Liu, K. Wu, Q. Fu, Metal-level robust, folding endurance, and highly temperature-stable MXene-based film with engineered aramid nanofiber for extreme-condition electromagnetic interference shielding applications, ACS Appl. Mater. Interfaces. 12 (2020) 26485–26495. https://doi.org/10.1021/ACSAMI.0C07387.

[179] M.M. Rahman, A.B. Puthirath, A. Adumbumkulath, T. Tsafack, H. Robatjazi, M. Barnes, Z. Wang, S. Kommandur, S. Susarla, S.M. Sajadi, D. Salpekar, F. Yuan, G. Babu, K. Nomoto, S. Islam, R. Verduzco, S.K. Yee, H.G. Xing, P.M. Ajayan, Fiber reinforced layered dielectric nanocomposite, Adv. Funct. Mater. 29 (2019) 1900056. https://doi.org/10.1002/ADFM.201900056.

[180] L. Si, Z. Lu, C. Yao, Q. Ma, Y. Zhao, Y. Wang, D. Wang, Z. Jin, Nacre-like

nanocomposite film with excellent dielectric insulation properties and mechanical strength based on montmorillonite nanosheet and aramid nanofiber, J. Mater. Sci. 2020 55 (2020) 5948–5960. https://doi.org/10.1007/S10853-020-04412-0.

[181] Z. Liu, J. Lyu, D. Fang, X. Zhang, Nanofibrous Kevlar aerogel threads for thermal insulation in harsh environments, ACS Nano. 13 (2019) 5703–5711. https://doi.org/10.1021/ACSNANO.9B01094.

[182] J. Lyu, Z. Liu, X. Wu, G. Li, D. Fang, X. Zhang, Nanofibrous Kevlar aerogel films and their phase-change composites for highly efficient infrared stealth, ACS Nano. 13 (2019) 2236–2245. https://doi.org/10.1021/ACSNANO.8B08913.

[183] J. Lin, S.H. Bang, M.H. Malakooti, H.A. Sodano, Isolation of aramid nanofibers for high strength and toughness polymer nanocomposites, ACS Appl. Mater. Interfaces. 9 (2017) 11167–11175. https://doi.org/10.1021/acsami.7b01488.

[184] B.A. Patterson, M.H. Malakooti, J. Lin, A. Okorom, H.A. Sodano, Aramid nanofibers for multiscale fiber reinforcement of polymer composites, Compos. Sci. Technol. 161 (2018) 92–99. https://doi.org/10.1016/j.compscitech.2018.04.005.

[185] J. Nasser, J. Lin, K. Steinke, H.A. Sodano, Enhanced interfacial strength of aramid fiber reinforced composites through adsorbed aramid nanofiber coatings, Compos. Sci. Technol. 174 (2019) 125–133. https://doi.org/10.1016/j.compscitech.2019.02.025.

[186] J. Nasser, K. Steinke, L. Zhang, H. Sodano, Enhanced interfacial strength of hierarchical fiberglass composites through an aramid nanofiber interphase, Compos. Sci. Technol. 192 (2020) 108109. https://doi.org/10.1016/j.compscitech.2020.108109.

[187] J.U. Lee, B. Park, B.S. Kim, D.R. Bae, W. Lee, Electrophoretic deposition of aramid nanofibers on carbon fibers for highly enhanced interfacial adhesion at low content, Compos. Part A Appl. Sci. Manuf. 84 (2016) 482–489. https://doi.org/10.1016/j.compositesa.2016.02.029.

[188] S. Bagga, J. Akhtar, S. Mishra, Synthesis and applications of ZnO nanowire: A review, AIP Conf. Proc. 1989 (2018) 020004. https://doi.org/10.1063/1.5047680.

[189] Z.L. Wang, Zinc oxide nanostructures: growth, properties and applications, J. Phys. Condens. Matter. 16 (2004) R829. https://doi.org/10.1088/0953-8984/16/25/R01.

[190] X. Li, C. Zhao, X. Liu, A paper-based microfluidic biosensor integrating zinc oxide nanowires for electrochemical glucose detection, Microsystems Nanoeng. 2015 1 (2015) 15014. https://doi.org/10.1038/micronano.2015.14.

[191] M. Villani, D. Delmonte, M. Culiolo, D. Calestani, N. Coppedè, M. Solzi, L. Marchini, R. Bercella, A. Zappettini, Turning carbon fiber into a stress-sensitive composite material,

J. Mater. Chem. A. 4 (2016) 10486–10492. https://doi.org/10.1039/C6TA02646J.

[192] J. Zang, C.M. Li, X. Cui, J. Wang, X. Sun, H. Dong, C.Q. Sun, Tailoring zinc oxide nanowires for high performance amperometric glucose sensor, Electroanalysis. 19 (2007) 1008–1014. https://doi.org/10.1002/ELAN.200603808.

[193] R.K. Joshi, Q. Hu, F. Alvi, N. Joshi, A. Kumar, Au decorated zinc oxide nanowires for CO sensing, J. Phys. Chem. C. 113 (2009) 16199–16202. https://doi.org/10.1021/JP906458B.

[194] Y. Zhang, K. Yu, D. Jiang, Z. Zhu, H. Geng, L. Luo, Zinc oxide nanorod and nanowire for humidity sensor, Appl. Surf. Sci. 242 (2005) 212–217. https://doi.org/10.1016/J.APSUSC.2004.08.013.

[195] A. Khan, M. Hussain, O. Nur, M. Willander, E. Broitman, Analysis of direct and converse piezoelectric responses from zinc oxide nanowires grown on a conductive fabric, Phys. Status Solidi. 212 (2015) 579–584. https://doi.org/10.1002/PSSA.201431625.

[196] T.S. van den Heever, W.J. Perold, Comparing three different energy harvesting circuits for a ZnO nanowire based nanogenerator, Smart Mater. Struct. 22 (2013) 105029. https://doi.org/10.1088/0964-1726/22/10/105029.

[197] M. H. Malakooti, B. A. Patterson, Hyun-Sik Hwang, H. A. Sodano, ZnO nanowire interfaces for high strength multifunctional composites with embedded energy harvesting, Energy Environ. Sci. 9 (2016) 634–643. https://doi.org/10.1039/C5EE03181H.

[198] B.A. Patterson, H.A. Sodano, Enhanced interfacial strength and UV shielding of aramid fiber composites through ZnO nanoparticle sizing, ACS Appl. Mater. Interfaces. 8 (2016) 33963–33971. https://doi.org/10.1021/acsami.6b07555.

[199] R. Khokhra, B. Bharti, H.-N. Lee, R. Kumar, Visible and UV photo-detection in ZnO nanostructured thin films via simple tuning of solution method, Sci. Reports 7 (2017) 15032. https://doi.org/10.1038/s41598-017-15125-x.

[200] S.-Y. Kuo, H.-I. Lin, Field emission characteristics of zinc oxide nanowires synthesized by vapor-solid process, Nanoscale Res. Lett. 9 (2014) 70. https://doi.org/10.1186/1556-276X-9-70.

[201] M. Law, L.E. Greene, J.C. Johnson, R. Saykally, P. Yang, Nanowire dye-sensitized solar cells, Nat. Mater. 2005 4 (2005) 455–459. https://doi.org/10.1038/nmat1387.

[202] J. Cui, U.J. Gibson, A simple two-step electrodeposition of Cu2O/ZnO nanopillar solar cells, J. Phys. Chem. C. 114 (2010) 6408–6412. https://doi.org/10.1021/JP1004314.

[203] G. Syrrokostas, K. Govatsi, G. Leftheriotis, S.N. Yannopoulos, Platinum decorated zinc oxide nanowires as an efficient counter electrode for dye sensitized solar cells, J.

Electroanal. Chem. 835 (2019) 86–95. https://doi.org/10.1016/J.JELECHEM.2019.01.013.

[204] J. Yu, X. Yu, Hydrothermal synthesis and photocatalytic activity of zinc oxide hollow spheres, Environ. Sci. Technol. 42 (2008) 4902–4907. https://doi.org/10.1021/ES800036N.

[205] J. Nasser, K. Steinke, H. Hwang, H. Sodano, Nanostructured ZnO interphase for carbon fiber reinforced composites with strain rate tailored interfacial strength, Adv. Mater. Interfaces. 7 (2020) 1901544. https://doi.org/10.1002/admi.201901544.

[206] J. Nasser, K. Steinke, H. Sodano, ZnO Nanostructured interphase for multifunctional and lightweight glass fiber reinforced composite materials under various loading conditions, ACS Appl. Nano Mater. 3 (2020) 1363–1372. https://doi.org/10.1021/acsanm.9b02216.

[207] Y. Lin, G. Ehlert, H.A. Sodano, Increased interface strength in carbon fiber composites through a ZnO nanowire interphase, Adv. Funct. Mater. 19 (2009) 2654–2660. https://doi.org/10.1002/ADFM.200900011.

[208] U. Galan, Y. Lin, G.J. Ehlert, H.A. Sodano, Effect of ZnO nanowire morphology on the interfacial strength of nanowire coated carbon fibers, Compos. Sci. Technol. 71 (2011) 946–954. https://doi.org/10.1016/j.compscitech.2011.02.010.

[209] G.J. Ehlert, U. Galan, H.A. Sodano, Role of surface chemistry in adhesion between ZnO nanowires and carbon fibers in hybrid composites, ACS Appl. Mater. Interfaces. 5 (2013) 635–645. https://doi.org/10.1021/am302060v.

[210] G.J. Ehlert, H.A. Sodano, Zinc oxide nanowire interphase for enhanced interfacial strength in lightweight polymer fiber composites, ACS Appl. Mater. Interfaces. 1 (2009) 1827–1833. https://doi.org/10.1021/am900376t.

[211] K. Kong, B.K. Deka, M. Kim, A. Oh, H. Kim, Y. Bin Park, H.W. Park, Interlaminar resistive heating behavior of woven carbon fiber composite laminates modified with ZnO nanorods, Compos. Sci. Technol. 100 (2014) 83–91. https://doi.org/10.1016/j.compscitech.2014.06.006.

[212] G. Swaminathan, C. Palanisamy, G. Chidambaram, G. Henri, C. Udayagiri, Enhancing the interfacial strength of glass/epoxy composites using ZnO nanowires, Compos. Interfaces. 25 (2018) 151–168. https://doi.org/10.1080/09276440.2017.1341790.

[213] M.H. Malakooti, Z. Zhou, J.H. Spears, T.J. Shankwitz, H.A. Sodano, Biomimetic nanostructured interfaces for hierarchical composites, Adv. Mater. Interfaces. 3 (2016) 1500404. https://doi.org/10.1002/admi.201500404.

[214] H.S. Hwang, M.H. Malakooti, B.A. Patterson, H.A. Sodano, Increased interyarn friction through ZnO nanowire arrays grown on aramid fabric, Compos. Sci. Technol. 107 (2015)

75–81. https://doi.org/10.1016/j.compscitech.2014.12.001.

[215] M.H. Malakooti, H.-S. Hwang, H.A. Sodano, Morphology-controlled ZnO nanowire arrays for tailored hybrid composites with high damping, ACS Appl. Mater. Interfaces. 7 (2015) 332–339. https://doi.org/10.1021/am506272c..

[216] M.H. Malakooti, H.S. Hwang, N.C. Goulbourne, H.A. Sodano, Role of ZnO nanowire arrays on the impact response of aramid fabrics, Compos. Part B Eng. 127 (2017) 222–231. https://doi.org/10.1016/j.compositesb.2017.05.084.

[217] S. Arora, A. Majumdar, B.S. Butola, Deciphering the structure-induced impact response of ZnO nanorod grafted UHMWPE woven fabrics, Thin-Walled Struct. 156 (2020) 106991. https://doi.org/10.1016/j.tws.2020.106991.

[218] J. Lin, Z. Peng, Y. Liu, F. Ruiz-Zepeda, R. Ye, E.L.G. Samuel, M.J. Yacaman, B.I. Yakobson, J.M. Tour, Laser-induced porous graphene films from commercial polymers, Nat. Commun. 5 (2014) 5714. https://doi.org/10.1038/ncomms6714.

[219] L.X. Duy, Z. Peng, Y. Li, J. Zhang, Y. Ji, J.M. Tour, Laser-induced graphene fibers, Carbon N. Y. 126 (2018) 472–479. https://doi.org/10.1016/j.carbon.2017.10.036.

[220] D.X. Luong, K. Yang, J. Yoon, S.P. Singh, T. Wang, C.J. Arnusch, J.M. Tour, Laser-induced graphene composites as multifunctional surfaces, ACS Nano. 13 (2019) 2579–2586. https://doi.org/10.1021/acsnano.8b09626.

[221] Y. Chyan, R. Ye, Y. Li, S.P. Singh, C.J. Arnusch, J.M. Tour, Laser-induced graphene by multiple lasing: Toward electronics on cloth, paper, and food, ACS Nano. 12 (2018) 2176–2183. https://doi.org/10.1021/acsnano.7b08539.

[222] L.Q. Tao, H. Tian, Y. Liu, Z.Y. Ju, Y. Pang, Y.Q. Chen, D.Y. Wang, X.G. Tian, J.C. Yan, N.Q. Deng, Y. Yang, T.L. Ren, An intelligent artificial throat with sound-sensing ability based on laser induced graphene, Nat. Commun. 8 (2017) 14579. https://doi.org/10.1038/ncomms14579.

[223] R. Rahimi, M. Ochoa, W. Yu, B. Ziaie, Highly stretchable and sensitive unidirectional strain sensor via laser carbonization, ACS Appl. Mater. Interfaces. 7 (2015) 4463–4470. https://doi.org/10.1021/am509087u.

[224] Y. Wang, Y. Wang, P. Zhang, F. Liu, S. Luo, Laser-induced freestanding graphene papers: A new route of scalable fabrication with tunable morphologies and properties for multifunctional devices and structures, Small. 14 (2018) 1802350. https://doi.org/10.1002/smll.201802350.

[225] S. Luo, P.T. Hoang, T. Liu, Direct laser writing for creating porous graphitic structures and their use for flexible and highly sensitive sensor and sensor arrays, Carbon N. Y. 96

(2016) 522–531. https://doi.org/10.1016/j.carbon.2015.09.076.

[226] L.A. Groo, J. Nasser, D.J. Inman, H.A. Sodano, Laser induced graphene for in situ damage sensing in aramid fiber reinforced composites, Compos. Sci. Technol. 201 (2021) 108541. https://doi.org/10.1016/j.compscitech.2020.108541

[227] J. Nasser, L.A. Groo, L. Zhang, H. Sodano, Laser induced graphene fibers for multifunctional aramid fiber reinforced composite, Carbon N. Y. 158 (2020) 146–156. https://doi.org/10.1016/j.carbon.2019.11.078.

[228] J. Karger-Kocsis, H. Mahmood, A. Pegoretti, Recent advances in fiber/matrix interphase engineering for polymer composites, Prog. Mater. Sci. 73 (2015) 1–43. https://doi.org/10.1016/J.PMATSCI.2015.02.003.

[229] P.J. Herrera-Franco, L.T. Drzal, Comparison of methods for the measurement of fibre/matrix adhesion in composites, Composites. 23 (1992) 2–27. https://doi.org/10.1016/0010-4361(92)90282-Y.

[230] R.J. Kerans, T.A. Parthasarathy, Theoretical analysis of the fiber pullout and pushout tests, J. Am. Ceram. Soc. 74 (1991) 1585–1596. https://doi.org/10.1111/J.1151-2916.1991.TB07144.X.

[231] S.K. Kang, D.B. Lee, N.S. Choi, Fiber/epoxy interfacial shear strength measured by the microdroplet test, Compos. Sci. Technol. 69 (2009) 245–251. https://doi.org/10.1016/J.COMPSCITECH.2008.10.016.

[232] A. Hodzic, S. Kalyanasundaram, A. Lowe, Z.H. Stachurski, The microdroplet test: Experimental and finite element analysis of the dependance of failure mode on droplet shape, Compos. Interfaces 6 (2012) 375–389. https://doi.org/10.1163/156855498X00379.

[233] A. Hodzic, Z.H. Stachurski, J.K. Kim, An analysis of microdroplet test: Effects of specimen geometry, matrix type, fibre treatment and water ageing, Polym. Polym. Compos. 9 (2001) 499–508. https://doi.org/10.1177/096739110100900802.

[234] A. ten Busschen, A.P.S. Selvadurai, Mechanics of the segmentation of an embedded fiber, part I: Experimental investigations, J. Appl. Mech. 62 (1995) 87–97. https://doi.org/10.1115/1.2895888.

[235] S. Feih, K. Wonsyld, D. Minzari, P. Westermann, H. Lilholt, Establishing a testing procedure for the single fiber fragmentation test, AFM, Department for Material Research, (2004). https://backend.orbit.dtu.dk/ws/portalfiles/portal/5223434/ris-r-1483.pdf , 2004 (accessed 9 July 2020).

[236] M.R. Piggott, The single-fibre pull-out method: its advantages, interpretation and experimental realization, Compos. Interfaces. 1 (1993) 211–223.

https://doi.org/10.1163/156855493X00086.

[237] Development of a zinc oxide nanowire interphase for enhanced structural composites - NASA/ADS. https://ui.adsabs.harvard.edu/abs/2012PhDT.....62E/abstract , n.d. (accessed 2 November 2021).

[238] M.R. Piggott, Why interface testing by single-fibre methods can be misleading, Compos. Sci. Technol. 57 (1997) 965–974. https://doi.org/10.1016/S0266-3538(97)00036-5.

[239] X.J. Gong, J.A. Arthur, L.S. Penn, Strain rate effect in the single-fiber-fragmentation test, Polym. Compos. 22 (2001) 349–360. https://doi.org/10.1002/PC.10543.

[240] Z. Li, X. Bi, J. Lambros, P.H. Geubelle, Dynamic fiber debonding and frictional push-out in mode composite systems: Experimental observations, Exp. Mech. 42 (2002) 417–425. https://doi.org/10.1007/BF02412147.

[241] V. Rao, P. Herrera-franco, A.D. Ozzello, L.T. Drzal, A direct comparison of the fragmentation test and the microbond pull-out test for determining the interfacial shear strength, J. Adhes. 34 (2006) 65–77. https://doi.org/10.1080/00218469108026506.

[242] P. Zinck, H.D. Wagner, L. Salmon, J.F. Gerard, Are microcomposites realistic models of the fibre/matrix interface? I. Micromechanical modelling, Polymer (Guildf). 42 (2001) 5401–5413. https://doi.org/10.1016/S0032-3861(00)00870-3.

[243] A. Kelly, W.R. Tyson, Tensile properties of fibre-reinforced metals: Copper/tungsten and copper/molybdenum, J. Mech. Phys. Solids. 13 (1965) 329–350. https://doi.org/10.1016/0022-5096(65)90035-9.

[244] C. DiFrancia, T.C. Ward, R.O. Claus, The single-fibre pull-out test. 1: Review and interpretation, Compos. Part A Appl. Sci. Manuf. 27 (1996) 597–612. https://doi.org/10.1016/1359-835X(95)00069-E.

[245] B.F. Sørensen, H. Lilholt, Fiber pull-out test and single fiber fragmentation test - Analysis and modelling, in: IOP Conf. Ser. Mater. Sci. Eng., Institute of Physics Publishing, 2016: p. 012009. https://doi.org/10.1088/1757-899X/139/1/012009.

[246] M.R. Sanchis, V. Blanes, M. Blanes, D. Garcia, R. Balart, Surface modification of low density polyethylene (LDPE) film by low pressure O 2 plasma treatment, 42 (2006) 1558–1568. https://doi.org/10.1016/j.eurpolymj.2006.02.001.

[247] U. Galan, H.A. Sodano, Intermolecular interactions dictating adhesion between ZnO and graphite, Carbon N. Y. 63 (2013) 517–522. https://doi.org/10.1016/j.carbon.2013.07.027.

[248] B.A. Patterson, U. Galan, H.A. Sodano, Adhesive Force Measurement between HOPG and Zinc Oxide as an Indicator for Interfacial Bonding of Carbon Fiber Composites, ACS Appl. Mater. Interfaces. 7 (2015) 15380–15387. https://doi.org/10.1021/acsami.5b03322.

[249] ASTM C1557 - 20 Standard Test Method for Tensile Strength and Youngs Modulus of Fibers, (n.d.). https://www.astm.org/Standards/C1557 (accessed 2 November 2021).

[250] H.S. Hwang, J. Nasser, H.A. Sodano, Piezoelectric stack actuator for measurement of interfacial shear strength at high strain rates, Exp. Mech. 59 (2019) 979–990. https://doi.org/10.1007/S11340-019-00502-6.

[251] Z. Hu, G. Oskam, P.C. Searson, Influence of solvent on the growth of ZnO nanoparticles, J. Colloid Interface Sci. 263 (2003) 454–460. https://doi.org/10.1016/S0021-9797(03)00205-4.

[252] K. Ma, P. Chen, B. Wang, G. Cui, X. Xu, A study of the effect of oxygen plasma treatment on the interfacial properties of carbon fiber/epoxy composites, J. Appl. Polym. Sci. 118 (2010) 1606–1614. https://doi.org/10.1002/app.32549.

[253] J.B. Donnet, M. Brendle, T.L. Dhami, P. Bahl, Plasma treatment effect on the surface energy of carbon and carbon fibers, Carbon N. Y. 24 (1986) 757–770 https://doi.org/10.1016/0008-6223(86)90186-7.

[254] M. Su, A. Gu, G. Liang, L. Yuan, The effect of oxygen-plasma treatment on Kevlar fibers and the properties of Kevlar fibers/bismaleimide composites, Appl. Surf. Sci. 257 (2011) 3158–3167. https://doi.org/10.1016/j.apsusc.2010.10.133.

[255] Y. Wan, X. Qu, J. Lu, C. Zhu, L. Wan, J. Yang, J. Bei, S. Wang, Characterization of surface property of poly(lactide-co-glycolide) after oxygen plasma treatment, Biomaterials. 25 (2004) 4777–4783. https://doi.org/10.1016/j.biomaterials.2003.11.051.

[256] F. Ji, Y. Hong, S. Peng, T. He, J. Sun, L. Yao, Y. Qiu, Effect of glycerol coating on the atmospheric pressure plasma treatment of UHMWPE fibers, J. Adhes. Sci. Technol. 26 (2012) 289–301. https://doi.org/10.1163/016942411X576491.

[257] C.Y. Huang, J.Y. Wu, C.S. Tsai, K.H. Hsieh, J.T. Yeh, K.N. Chen, Effects of argon plasma treatment on the adhesion property of ultra high molecular weight polyethylene (UHMWPE) textile, Surf. Coatings Technol. 231 (2013) 507–511. https://doi.org/10.1016/j.surfcoat.2012.04.069.

[258] S.G. Lee, T.J. Kang, T.H. Yoon, Enhanced interfacial adhesion of ultra-high molecular weight polyethylene (UHMWPE) fibers by oxygen plasma treatment, J. Adhes. Sci. Technol. 12 (1998) 731–748. https://doi.org/10.1163/156856198X00263.

[259] P. Masse, J.P. Cavrot, P. François, J.M. Lefebvre, B. Escaig, Adhesion improvement of high modulus polyethylene fibers by surface plasma treatment: Evaluation by pull-out testing, Polym. Compos. 15 (1994) 247–251. https://doi.org/10.1002/pc.750150311.

[260] T.W. Clyne, A simple development of the shear lag theory appropriate for composites

with a relatively small modulus mismatch, Mater. Sci. Eng. A. 122 (1989) 183–192. https://doi.org/10.1016/0921-5093(89)90629-1.

[261] Honeywell Spectra ® Fiber 1000 high-strength, light-weight polyethylene fiber Product Information Sheet, www.honeywell.com/spectra, n.d. (accessed 17 May 2021).

[262] F. Alam, M. Choosri, T.K. Gupta, K.M. Varadarajan, D. Choi, S. Kumar, Electrical, mechanical and thermal properties of graphene nanoplatelets reinforced UHMWPE nanocomposites, Mater. Sci. Eng. B Solid-State Mater. Adv. Technol. 241 (2019) 82–91. https://doi.org/10.1016/j.mseb.2019.02.011.

[263] Y. Qin, X. Wang, Z.L. Wang, Microfibre-nanowire hybrid structure for energy scavenging, Nature. 451 (2008) 809–813. https://doi.org/10.1038/nature06601.

[264] H.S. Hwang, M.H. Malakooti, H.A. Sodano, Tailored interyarn friction in aramid fabrics through morphology control of surface grown ZnO nanowires, Compos. Part A Appl. Sci. Manuf. 76 (2015) 326–333. https://doi.org/10.1016/j.compositesa.2015.06.012.

[265] J.S. Stenzler, N. Goulbourne, D. Dillard, A. Wicks, T. Long, Impact Mechanics of PMMA/PC Multi-Laminates with Soft Polymer Interlayers, 2009.

[266] A. V. Ignatova, O.A. Kudryavtsev, M. V. Zhikharev, Influence of surface polymer coating on ballistic impact response of multi-layered fabric composites: Experimental and numerical study, Int. J. Impact Eng. 144 (2020) 103654. https://doi.org/10.1016/J.IJIMPENG.2020.103654.

[267] J. Nasser, L. Zhang, H. Sodano, Laser induced graphene interlaminar reinforcement for tough carbon fiber/epoxy composites, Compos. Sci. Technol. 201 (2021) 108493. https://doi.org/10.1016/J.COMPSCITECH.2020.108493.

[268] E.J. García, B.L. Wardle, A.J. Hart, Joining prepreg composite interfaces with aligned carbon nanotubes, Compos. Part A Appl. Sci. Manuf. 39 (2008) 1065–1070. https://doi.org/10.1016/j.compositesa.2008.03.011.

[269] J. Blanco, E.J. García, R. Guzmán de Villoria, B.L. Wardle, Limiting mechanisms of mode I interlaminar toughening of composites reinforced with aligned carbon nanotubes, J. of Compos. Mater. 43 (2009) 825–841. https://doi.org/10.1177/0021998309102398.